Alma Mater Studiorum - Università di Bologna

SCUOLA DI INGEGNERIA

DIPARTIMENTO DI INGEGNERIA DELL'ENERGIA ELETTRICA E DELL'INFORMAZIONE "GUGLIELMO MARCONI"

LAUREA MAGISTRALE IN INGEGNERIA DELL'ENERGIA ELETTRICA

TESI DI LAUREA MAGISTRALE

in

Electric Motor Desing M

Modelling and Analysis of Multi-Three-Phase Drives for Radial Force Control

Modellizzazione e Analisi di Azionamenti Multi-Trifase per il Controllo di Forza Radiale

Candidato:
Tiberio Spadi

Relatore:
Prof. Giacomo Sala

Correlatori:
Prof. Michele Degano
Prof. Angelo Tani
Ing. Mauro Di Nardo
Ing. Meiqi Wang

Sessione III
Anno Accademico 2021/2022

Abstract

Nell'ambito delle macchine elettriche per il controllo di forza radiale, in letteratura sono state proposte diverse soluzioni, tutte in grado di generare simultaneamente una distribuzione di flusso magnetico al traferro con periodicità p e $p \pm 1$ necessaria per produrre rispettivamente coppia e forza radiale. Per distinguere le diverse tipologie proposte, è possibile suddividerle in due categorie principali in base alla disposizione degli avvolgimenti. La prima fa uso di due gruppi di avvolgimenti separati: uno per generare la coppia e l'altro per produrre la forza radiale. La seconda si basa su un avvolgimento combinato, tipicamente multifase, in cui tutte le fasi contribuiscono simultaneamente alla produzione di coppia e forza radiale. Lo studio presentato in questo elaborato di tesi è incentrato sulle soluzioni multifase, anziché quelle con avvolgimenti separati. Le macchine elettriche multifase presentano una migliore capacità di tolleranza ai guasti rispetto a quelle a doppio avvolgimento, in quanto i controlli di coppia e forza possono ancora essere eseguiti in caso di condizioni di guasto di una o più fasi dell'avvolgimento. Inoltre, lo sfruttamento dell'intero avvolgimento per la produzione sia di coppia che di forza è ritenuto potenzialmente più efficiente, per il maggiore sfruttamento del rame in cava, rispetto alla soluzione con due avvoglimenti separati. Il controllo di forza della macchina elettrica è proposto al fine di ridurre la sollecitazione dei cuscinetti. I cuscinetti sono una delle parti più critiche di un motore elettrico in termini di probabilità di guasto. Il miglioramento della capacità di tolleranza ai guasti delle macchine elettriche tramite il controllo della forza radiale è dunque un argomento di ricerca promettente. Lo scopo dell'attività di tesi è ottenere un modello meccanico del motore elettrico e incorporarlo con il modello elettromagnetico di una macchina elettrica multifase; simulare il comportamento del motore attraverso un modello numerico (in ambiente Matlab/Simulink); valutare un algoritmo di controllo sufficientemente robusto e che consenta di mantenere elevate le prestazioni del motore anche durante la produzione di forza per compensazione attiva delle vibrazioni del rotore in corrispondenza dei cuscinetti. Il modello multifisico dell'azionamento multifase ed il controllo del motore sono stati sviluppati sulla base dei disegni e dei dati di un prototipo e del rispettivo banco di prova disponibile nel laboratorio del gruppo PEMC (Power Electronics, Machines and Control) dell'Università di Nottingham, UK. Prove sperimentali preliminari sono state eseguite per validare i modelli utilizzati, e altre sono attualmente in corso presso il medesimo gruppo di ricerca.

Abstract

In the field of electrical machines for radial force control, several solutions have been proposed in the literature, all of which are able to simultaneously generate a magnetic flux distribution at the air gap with periodicity p and $p \pm 1$ required to produce torque and radial force, respectively. To distinguish the different types proposed, it is possible to divide them into two main categories based on the arrangement of the windings. The first makes use of two separate sets of windings: one to generate the torque and the other to produce the radial force. The second is based on a combined winding, typically multiphase, in which all phases contribute simultaneously to the production of torque and radial force. The study presented in this thesis focuses on multiphase solutions, rather than those with separate windings. Multiphase electrical machines have a better fault-tolerance capability than dual-winding machines, as torque and force checks can still be performed in the event of failure conditions of one or more winding phases. In addition, the utilization of the entire winding for both torque and force production is considered potentially more efficient, due to the greater utilization of the copper in the slots, than the solution with two separate windings. Force control of the electric machine is proposed in order to reduce bearing stress. Bearings are one of the most critical parts of an electric motor in terms of the probability of failure. Therefore, improving the fault-tolerance capability of electric machines through radial force control is a promising research topic. The purpose of the thesis activity is to obtain a mechanical model of the electric motor and incorporate it with the electromagnetic model of a multiphase electric machine; to simulate the behavior of the motor through a numerical model (in the Matlab/Simulink environment) and to evaluate a control algorithm that is sufficiently robust and allows the motor's performance to remain high even during force generation by active compensation of rotor vibration at the bearings. The multiphysics model of the multiphase drive and the motor control were developed based on drawings and data from a prototype and the respective test bench available in the laboratory of the PEMC (Power Electronics, Machines and Control) group at the University of Nottingham, UK. Preliminary experimental tests have been carried out to validate the models used, and others are currently underway in the same research group.

Contents

Chapter 1

Overview of Radial Force Control and Multiphase Machines

This chapter is the result of the literature review of the principles and the state of the art in the field of radial force control in electrical machines. Firstly, the motivations for investigating radial forces are presented and a general description of the strategy employed to reduce stress on bearings and vibrations is introduced. The active control of radial forces in electric motors is of great interest since it allows also for the production of the suspension force of the rotor and, consequently, is an alternative technology to the use of devices such as Active Magnetic Bearings (AMBs) in the so-called Bearingless Machines (BMs) or in electric machines for bearing relief. Afterward, some examples of industrial applications are described. After a brief description of the multi-phase electrical machine and the radial force production principle, the overview of the drive and its control strategy studied in this thesis are presented.

1.1 Introduction

Application requirements for electrical machines are very varied, however, there is a general trend towards increasing their lifetime and their reliability as well as reducing their maintenance and noise. Indeed, acoustic noise and mechanical vibrations are increasingly stringent design requirements, especially for high-speed machines [1, 2]. The impact of mechanical bearings on the reliability and maintenance of electrical machines is typically severe [3, 4]. The active control of radial forces could lead to significant improvement in terms of noise reduction and vibration dampening [5, 6]. This would also enable the compensation of external forces acting on the rotating structure such as Unbalanced Magnetic Pull (UMP) and inertial forces (like the gyroscopic effect that affects the electric automotive and aircraft rotors and the out-of-balance force). The UMP, in particular, has been widely investigated and its minimization is often considered from a design point of

view [7], especially for brushless motors with a fractional number of slots per pole and per phase (e.g., tooth wound concentrated windings). It can be caused by the effect of the rotor eccentricity, or by the machine's geometric features (such as rotor and stator structures in certain machine topologies), as well as by the combination of poles and slots number [8, 9]. Sometimes the design does not succeed in the elimination of the UMP. Furthermore, mass unbalance is often present after the manufacturing process. This unbalance leads to a displacement between the principal rotor axis of inertia and its geometric axis [10]. The trend to move towards higher density machines clearly implies increasing the operational speed that in turn increases the centrifugal unbalance forces. Therefore, vibration control and active balancing techniques have become fundamental. They have been adopted to achieve a longer bearing lifetime and to avoid unscheduled shut-downs. In [11], it has been shown that active vibration control techniques have many advantages over passive ones. In fact, despite their more complicated implementation, the former are more flexible since they can be employed when several vibration modes are excited and can adapt to the motor operation according to the vibration characteristics. More recently, bearingless machines (BM) are attracting growing attention because of their more compact structure, when compared to their Active Magnetic Bearings (AMB) counterparts. The reasons that motivate the development of bearingless technology are mainly the high failure rate of mechanical bearings, high rotational speed application requirements, and oil-free / high-purity environments. To be more specific, the most targeted applications for BMs are:

- centrifugal pumps [12, 13, 14, 15];
- artificial hearts [16, 17];
- mixers for chemical and pharmaceutical applications [18, 19] and fans[20, 21];

Furthermore, a full levitating system is particularly convenient when high and ultra-high rotation speeds have to be achieved [22] since it allows full rotor-dynamic control on the rotating component and provides damping effects while crossing critical frequencies [23]. It is the case of compressors [24], flywheels [23, 25], and generators, where high rotational speed operation allows for minimizing weight, volume, and cost while maximizing the efficiency of the whole system [26].

1.2 Incidence of bearing failures on the failure rate of electric machines

In general, there are many types of electrical rotating machines within various classes of power range and duty cycles. These machines are operated under industrial or civil conditions. Every machine can eventually fail and lead to safety risks and economical losses. Therefore, it is necessary to evaluate failure rates and their distribution over certain types of electrical machines and their subsystems. The failure rate of different parts of electrical machines are considered in [3] for the following types of electrical machines:

- Turbo generators
- Electric motors
- Synchronous motors

Failure rates are calculated according to Eq. (1.1):

$$\lambda = \frac{\sum_{i=1}^{n} m_i}{\sum_{i=1}^{n} M_i} \cdot 100 \tag{1.1}$$

where λ stands for failure rate per year in percentage, m_i is the number of machines that failed in the i^{th} year and the M_i is the number of machines that have been in service in the i^{th} year.

1.2.1 Failure Rate of Turbo-generator Parts

In the turbo-generator sector, there are many data and studies available on the reliability and failure probability of different components, while in other application areas, the number of studies and publications is very small. Therefore, studies mainly from this area are reported in this section. For turbo generators, the reference [27] presents a percentage of failures related to each subsystem part. Fig. 1.1 shows that the distribution of the failures across these subsystems is quite uniform, with a relevant percentage of failures related to the bearings system.

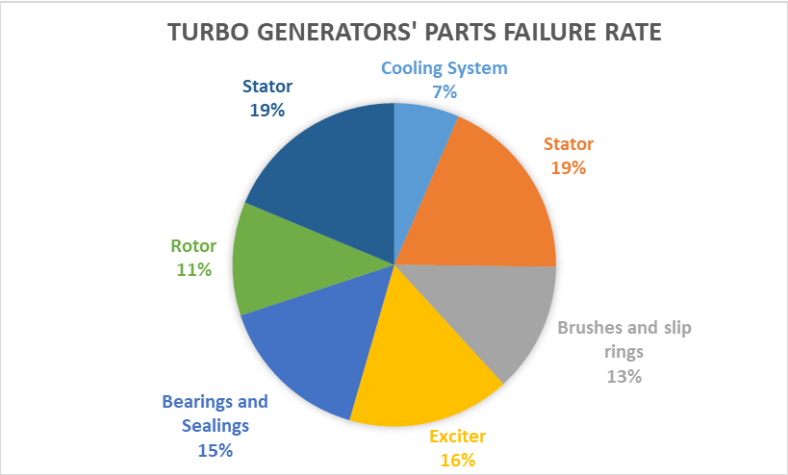

Figure 1.1: Turbo generators' parts failure rate [3].

1.2.2 Failure Rate of Electric Motor Parts

Electric motors operate within a wide range of applications (fans, pumps and drives for various purposes) including critical ones. The types of machines surveyed are induction motors (both squirrel cage and wound rotor) and synchronous motors. Failures distributed over the most general main motor parts according to [28] are shown in Fig. 1.2. As can be seen, failures related to bearings are the most frequent and represent 41% of the total. The following specific components failed most frequently: ground insulation (17.9 % of all failed machines reported) followed by sleeve bearings (11.4 %) and ball bearings (5.5 %) [28]. Bearings-related failures are for instance associated with the failure of various types of bearings (sleeve, thrust, ball), leakages, seals or oil systems.

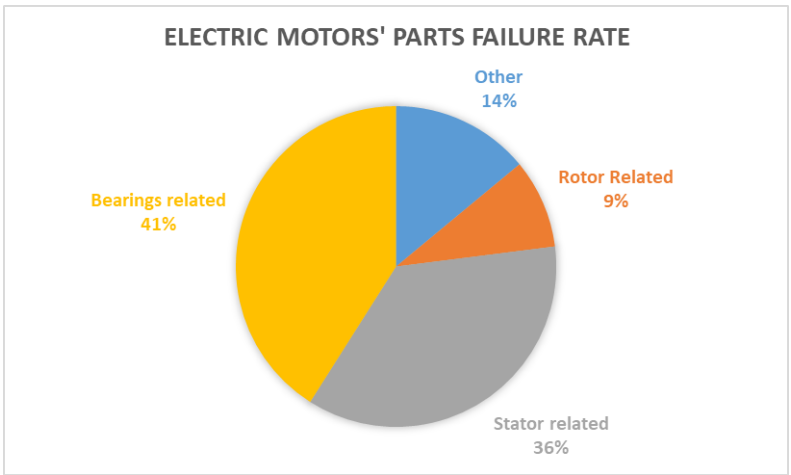

Figure 1.2: Electric Motors' parts failure rate [3].

1.2.3 Failure Rate of Synchronous Motor Parts

Synchronous motors' failures are discussed in the introduction section of [4] and the distribution of faulty components was presented. As it is shown, for high voltage motors the majority of failures are reported for the stator winding (60 %) followed by rotor winding and bearings (13 % each). The chart is shown in Fig. 1.3.

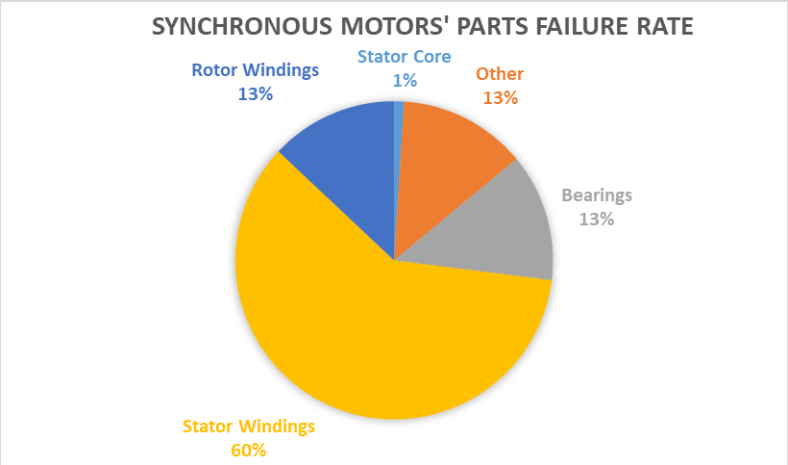

Figure 1.3: Synchronous motors' parts failure rate [3].

1.3 Multiphase Electrical Machines

Multiphase motor drives were already adopted almost 50 years ago when, in 1969, a five-phase voltage source inverter-fed induction motor drive was proposed [29]. Multiphase motors received relatively little attention for the next 20 years, until the 1990s when researchers from all over the world began to show a strong interest in their potential. In particular, the main fields of multiphase drives application are ship propulsion [30], aircraft sector [31], and electric traction [32]. All aforementioned uses require sizable power converters. Therefore, by using a multiphase machine, the possibility of splitting the power into several converters is of great interest since the cost, the size, and the stress of the electronic components is expected to drop. Furthermore, a multiphase winding presents a greater number of degrees of freedom than a three-phase machine which can be exploited for different scopes:

- Independent control of Magneto-Motive Force (MMF) spatial harmonic components that can be exploited, for example, to produce radial force in a BM or to increase the torque density.
- Fault-tolerant capabilities of the drive can be successfully enhanced by a multiphase winding modular architecture, as proposed in the literature on the electrification in the aircraft and marine sectors.

1.4 Radial force control for Vibration Suppression

Rotating electrical machines used in bearingless applications feature the capability of simultaneously generating controlled radial forces and torque. While the torque allows spinning the rotor at the desired speed, the x and y radial force components are involved in the control of the rotor's radial position. More precisely, in the case of bearingless levitating motors, the aim is the centering of the rotor with respect to the stator lamination. Another application of this kind of electrical machine is the active control of the system vibrations when the rotor is constrained by mechanical bearings, as described in [33]. In both cases, their adoption allows operating around the critical speed which is defined by the rotodynamic behavior of the system (rotor, mechanical bearings, and housing). Several rotating electrical machine topologies able of producing and controlling both torque and radial forces have been proposed in the literature and adopted in the industry to lead to improvement in terms of noise reduction and vibration dampening [6, 34, 11]. In this thesis, the role of radial force control for the vibration suppression of the shaft at the bearing locations is further investigated thanks to the implementation of a rotodynamic mechanical model.

1.4.1 Radial force production principle

It is interesting to consider the different strategies that have been chosen by researchers around the world to generate a controllable radial force and torque. These strategies were developed for motors with different winding structures. Conversely, the mathematical models are always carried out by exploiting either the virtual displacement method or the Maxwell and Lorentz equations. Some examples of key architectures are the followings:

- Separate torque and suspension windings.
- Five-phase winding with multiple orthogonal d-q planes for force and torque generation.
- Six-phase winding structure with fault-tolerant capability.
- Triple three-phase winding structure with decoupled torque and radial force control.

The machine object of study of this thesis is a triple three-phase sectored machine with decoupled torque and radial force control. The machine consists of a Surface Permanent Magnet (SPM) synchronous machine with three sectored three-phase windings as shown in Fig. 1.4.

The torque demand and the force vector are generated by controlling the three currents of the phases in the synchronous reference frame, respectively. The torque–force characteristic of the machine is derived in a generic form that can be extended to any

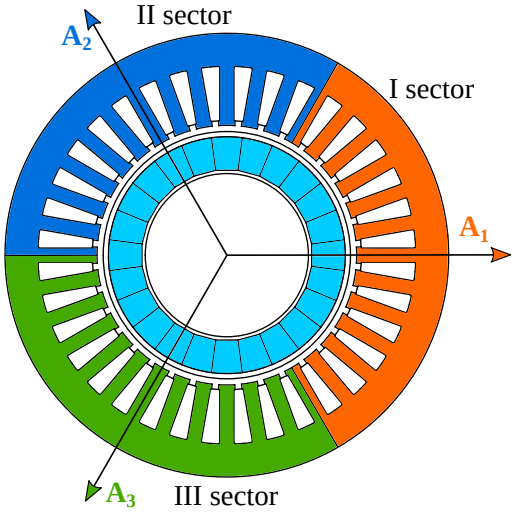

Figure 1.4: Radial cross-section of the multi-sector SPM Machine

multiphase machine. The approach presented in this paper is based on the methodology explained in [35]. Under the hypothesis of the linear magnetic behavior of the materials and magnetic decoupling between sectors, the matrix formulation (1.2) expresses the generalized mechanical wrench of the motor as a function of the stator phase currents:

$$\overline{W}_E = \mathbf{K_{abc}}(\theta_e)\bar{i}_{abc} \tag{1.2}$$

where:

- $\overline{W}_E = [F_x, F_y, T]^T$ is the vector of the wrench components, i.e., the x and y mechanical forces and the torque;
- $\bar{i}_{abc} = [i_{a_1}, i_{b_1}, i_{c_1}, ..., i_{a_3}, i_{b_3}, i_{c_3}]^T$ is the vector of the abc phase currents of each of the three-phase sub windings;
- $\theta_e = p\theta_m$ is the electrical angular position of the rotor magnetic axis with respect to the $a1$ phase magnetic axis;

$\mathbf{K_{abc}}(\theta_e)$ is the $3 \times 3n_s$ matrix that can be expressed as:

$$\mathbf{K_{abc}}(\theta_e) = [\ \mathbf{K_{abc,1}}(\theta_e),\ \ \ldots\ \ , \mathbf{K_{abc,n_s}}(\theta_e)\ ] \tag{1.3}$$

with n_s the number of sectors, and each $\mathbf{K_{abc,s}}(\theta_e)$ of the respective sector s is a 3×3 matrix defined as follows:

$$\mathbf{K_{abc,s}}(\theta_e) = \begin{bmatrix} K_{F_x,a,s}(\theta_e) & K_{F_x,b,s}(\theta_e) & K_{F_x,c,s}(\theta_e) \\ K_{F_y,a,s}(\theta_e) & K_{F_y,b,s}(\theta_e) & K_{F_y,c,s}(\theta_e) \\ K_{T,a,s}(\theta_e) & K_{T,b,s}(\theta_e) & K_{T,c,s}(\theta_e) \end{bmatrix} \tag{1.4}$$

It is possible to demonstrate that, as explained in [36], the mean q-axis current demand is obtained considering the torque expression:

$$T_E = \sum_{n=1}^{3} k_{T,n} i_{q,n} = k_T \sum_{n=1}^{3} i_{q,n} \quad \Rightarrow \quad \frac{1}{3} \sum_{n=1}^{3} i_{q,n} = \frac{T_E}{3k_T} \tag{1.5}$$

where k_T is the torque constant of the motor. Thus considering the magnetically isotropic structure of the MSPM machine, the torque is controlled only by the mean value of the q-axis current components of each sector.

1.4.2 Control System Overview

In the literature review presented, the active control of radial force was mainly applied for the rotor suspension. However, radial forces can be controlled to actively suppress vibrations in rotating machinery. In the next chapters, results will show that the radial displacement at bearing locations presents a periodic fluctuation caused by vibration forces acting on the rotor (out-of-balance and UMP forces are examples of these kinds of forces). Therefore, a position control algorithm will be introduced to suppress the rotor oscillation. Rotor vibrations typically present specific frequencies which are related to the design of the machine and the operating condition (number of poles, number of stator and rotor slots, rotational speed, load, eccentricity, etc.). A typical mechanical source of vibration is the rotor mass unbalance that produces forces synchronous with the rotation frequency [37]. The control strategy considered in this work is shown in Fig. 1.5 and aims to track the x position, y position and ω_m speed references.

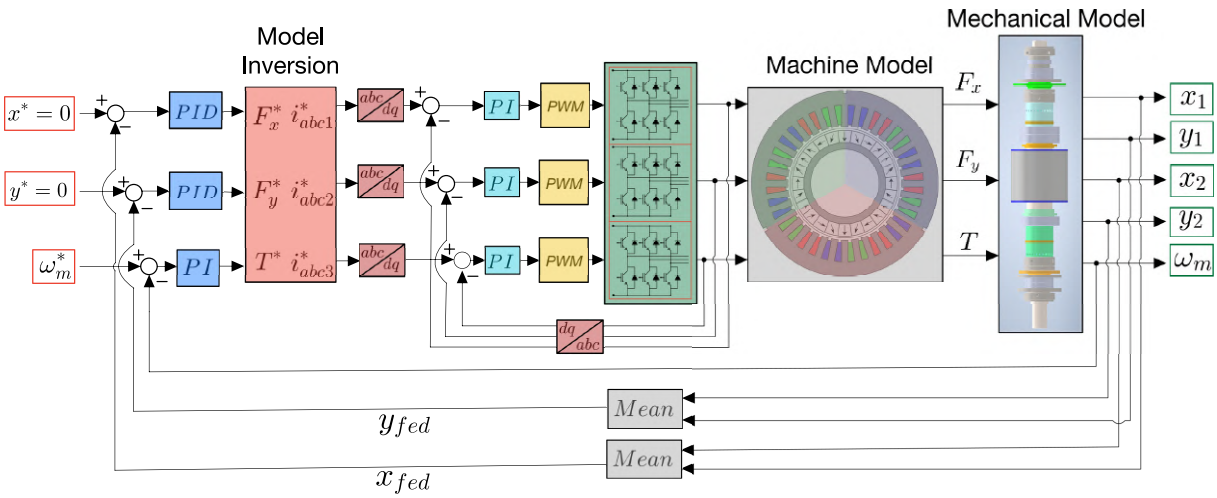

Figure 1.5: Model Overview

The radial force control is employed to dampen the vibrations of the rotor and to allow spinning of the machine at its critical speed with reduced vibrations. Starting from the errors calculated from the x, y and ω_m feedback, a PID position controller is introduced to

obtain the Wrench references $\overline{W}_E^* = [F_x^*, F_y^*, T^*]^T$. The current references $\bar{i}_{abc}^*$ required for the motor control are obtained by applying the pseudo-inverse matrix approach, which will be presented in the following work. The current control employs PI regulators to determine the reference phase voltages, applied to the motor by the converter. In particular, the instantaneous voltage set points for each machine sector are defined through a PWM modulator and supplied by a three-phase inverter.

It is important to mention that other several position controller configurations have been proposed to suppress the periodic disturbances using AMBs. For example, as explained in [23] a notch filter can be implemented to eliminate synchronous disturb or resonant PID controllers can be implemented to reject the disturbances [11].

Chapter 2

Electromagnetic Model of the Three-Sector SPM Synchronous Machine

This Chapter deals with the analytical model of the multi-three-phase machine considered in this study. The numerical model of the machine is based on the stator voltage equation considering the back-emf calculation, the phase resistances and the inductance matrix. Furthermore, this chapter shows the wrench mapping required to perform the radial force control. The introduced mathematical model considers also for the cross-coupling between the torque and the radial forces produced by the machine.

2.1 Machine Structure

The machine under consideration is a nine-phase three-sector SPM (Surface Permanents Magnets) motor with distributed windings and 3 pole pairs ($p = 3$). The machine presents three single-layer full-pitch distributed three-phase windings. These latter are located in 36 stator slots and each winding counts 2 slots per pole per phase. Each sector covers 120 mechanical degrees of the machine and counts one pole pair. The rotor features 24 surface-mounted NeFeB magnets. The magnets are arranged on the rotor with a Halbach array layout in order to obtain 3 pole pairs as shown in fig. 2.1. More details about this magnets' configuration are given in the section 2.1.1. The rotor presents also a 5 mm yoke (made with the same lamination steel as the stator). The lamination of this layer is necessary to limit the iron losses on the rotor. In fact, in order to achieve radial force production, the magnetic field at the airgap presents a non-synchronous component with the rotation of the rotor and this leads to high iron losses in the rotor if this is not laminated. More details of the magnetic field at the airgap and of the current waveforms are given further ahead. The phase currents are fed to the machine by adopting a series of

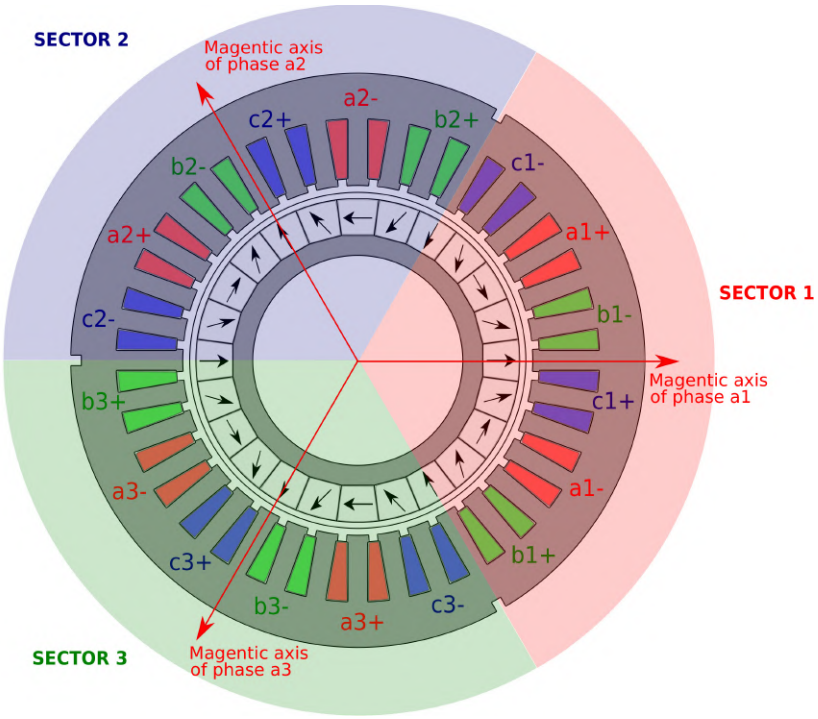

Figure 2.1: Radial cross-section of the multi-sector SPM Machine

three conventional three-phase inverters that share the same DC bus. Also, the converters are all managed in combination by a single control platform.

The main parameters and characteristics of the machine are described in Tab. 2.1

MACHINE PARAMETERS

Pole Number	$2p$	6	
Rated current	I_{max}	50	[Apk]
Rated torque	T_{max}	27	[Nm]
Max speed	n_{max}	20000	[rpm]
Rated power	P_{nom}	55	[kW]
Stator external radius	R_{ext}	82	[mm]
Rotor radius	r	46.2	[mm]
Airgap length	g	4	[mm]
Shaft radius	r_{shaft}	30	[mm]
Stack length	L	80	[mm]
Turns per coil	n	9	
PM relative permeability	μ_r	1.06360	
PM coercivity	H_c	849228.15	[A/m]

Table 2.1: Multi-Sector SPM Machine Parameters

2.1.1 Halbach Array Magnets configuration

A Halbach array is a special arrangement of permanent magnets that augments the magnetic field on one side of the array while canceling the field to near zero on the other

side. This is achieved by having a spatially rotating pattern of magnetization. Halbach permanent magnet array was first proposed by the Physicist Klaus Halbach, in literature [38], while at the Lawrence Berkeley National Laboratory during the 1980s, independently invented the Halbach array to focus particle accelerator beams. It consisted of a magnetized cylinder composed of ferromagnetic material producing (in the idealized case) an intense magnetic field confined entirely within the cylinder, with zero field outside. The cylinders can also be magnetized such that the magnetic field is entirely outside the cylinder, with zero field inside. Several magnetization distributions are shown in Fig. 2.2.

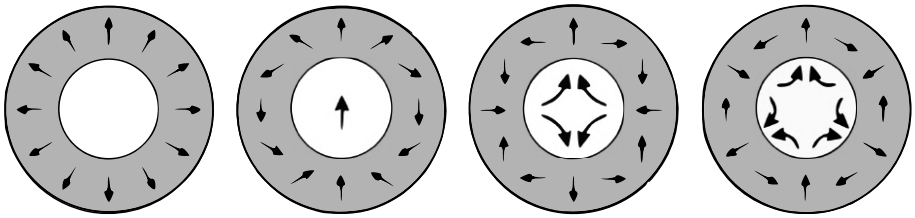

Figure 2.2: A ferromagnetic cylinder showing various magnetization patterns.

SPM with Halbach array magnets layout

The Halbach motor layout has been widely developed over the years, with several applications in aircraft [39] which is also one of the main application fields of Halbach motor [40], automotive sector [41] and flywheel energy storage [42]. Halbach magnetized brushless machines often present an essentially sinusoidal airgap field distribution which leads to a sinusoidal back-emf waveform, as well as negligible cogging torque, without employing skew. As in the considered machine (whose flux map is shown in 2.3), Halbach machines often employ tangentially segmented magnets (made of oriented bonded NdFeB magnets) to realize an approximate Halbach magnetization. Further axial segmentation is also used to limit induced eddy currents.

Generally, a Halbach cylindrical layout can be manufactured:

- from pre-magnetized anisotropic magnet segments having magnetization orientations that approximate the desired field distribution;
- molded as bonded isotropic ring magnets which are subsequently impulse magnetized to obtain a sinusoidally distributed magnetizing field [43];
- by employing an anisotropic molding compound which can be oriented during the compression or injection molding process to produce an anisotropic bonded Halbach cylinder (the magnet powder is both oriented and subsequently impulse magnetized by a sinusoidally distributed field) [44].

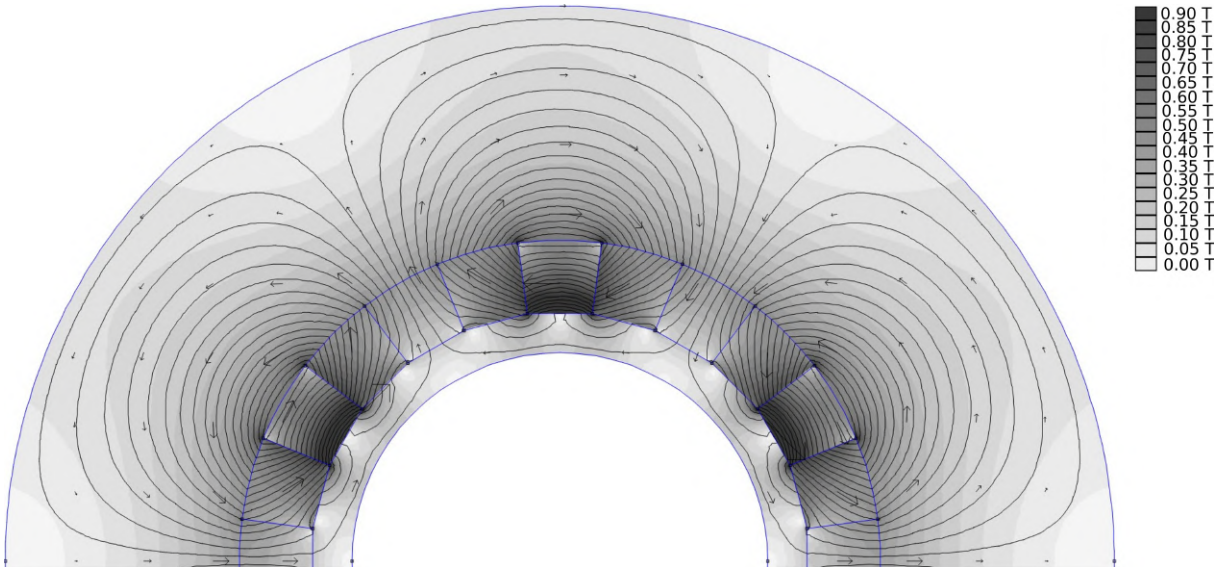

Figure 2.3: Flux density produced by the Halbach array magnets in the rotor machine.

2.2 Analytical model of the machine

The analytical model of the machine is based on the stator voltage equations. The voltage equation for a stator phase is:

$$v_{k_j} = R_s i_{k_j} + \frac{d\varphi_{k_j}}{dt} \tag{2.1}$$

Where:

- $j = a, b, c$ is the phase index;
- $k = 1, 2, 3$ is the sector index;
- v_{k_j} is the voltage applied to the k_j-th phase;
- R_s is the phase resistance;
- φ_{k_j} is the linked flux with the k_j-th phase;

2.2.1 Inductance Matrix calculation

For a single sector of the machine (or for a three-phase machine), the relationship between the flux linked with each phase and the phase currents can be expressed by a 3×3 inductance matrix as expressed in (2.2):

$$\begin{bmatrix} \varphi_a \\ \varphi_b \\ \varphi_c \end{bmatrix} = \begin{bmatrix} m_{aa} & m_{ab} & m_{ac} \\ m_{ba} & m_{bb} & m_{bc} \\ m_{ca} & m_{cb} & m_{cc} \end{bmatrix} \begin{bmatrix} i_a \\ i_b \\ i_c \end{bmatrix} + \begin{bmatrix} \varphi_{PM,a} \\ \varphi_{PM,b} \\ \varphi_{PM,c} \end{bmatrix} \tag{2.2}$$

where φ_a, φ_b, φ_c are the total linked fluxes with the stator phases, $\varphi_{PM,a}$, $\varphi_{PM,b}$, $\varphi_{PM,c}$ are the linked fluxes with the stator phases produced by the magnets only and m_{kj} is mutual inductance between the k-th and the j-th phase and m_{kk} is the self-inductance coefficient of the phase k (with $k = a, b, c$) and it results:

$$m_{kk} = l_l + l_{kk} \qquad for\ k = a, b, c \tag{2.3}$$

where l_l is the phase leakage inductance coefficient and l_{kk} is the self-inductance coefficient net of the leakage contribution.

For the considered 9-phase machine the relation between the fluxes and the currents is expressed in (2.4):

$$\bar{\varphi} = \mathbf{M}\bar{i}_{abc} + \bar{\varphi}_{PM} \tag{2.4}$$

With:

- $\bar{\varphi} = [\varphi_{a_1},\ \varphi_{b_1},\ \varphi_{c_1},\ \varphi_{a_2},\ \varphi_{b_2},\ \varphi_{c_2},\ \varphi_{a_3},\ \varphi_{b_3},\ \varphi_{c_3}]^T$ are the linked fluxes with the stator phases;
- $\bar{i} = [i_{a_1},\ i_{b_1},\ i_{c_1},\ i_{a_2},\ i_{b_2},\ i_{c_2},\ i_{a_3},\ i_{b_3},\ i_{c_3}]^T$ are the phase currents;
- $\bar{\varphi}_{PM} = [\varphi_{PM,a1},\ \varphi_{PM,b1},\ \varphi_{PM,c1},\ \varphi_{PM,a2},\ \varphi_{PM,b2},\ \varphi_{PM,c2},\ \varphi_{PM,a3},\ \varphi_{PM,b3},\ \varphi_{PM,c3}]^T$ are the linked fluxes with the stator phases produced by the magnets.

And:

$$\mathbf{M}= \begin{bmatrix} m_{a_1a_1} & m_{a_1b_1} & m_{a_1c_1} & m_{a_1a_2} & m_{a_1b_2} & m_{a_1c_2} & m_{a_1a_3} & m_{a_1b_3} & m_{a_1c_3} \\ m_{a_1b_1} & m_{b_1b_1} & m_{b_1c_1} & m_{b_1a_2} & m_{b_1b_2} & m_{b_1c_2} & m_{b_1a_3} & m_{b_1b_3} & m_{b_1c_3} \\ m_{c_1a_1} & m_{c_1b_1} & m_{c_1c_1} & m_{c_1a_2} & m_{c_1b_2} & m_{c_1c_2} & m_{c_1a_3} & m_{c_1b_3} & m_{c_1c_3} \\ m_{a_2a_1} & m_{a_2b_1} & m_{a_2c_1} & m_{a_2a_2} & m_{a_21b_2} & m_{a_2c_2} & m_{a_2a_3} & m_{a_2b_3} & m_{a_2c_3} \\ m_{b_2a_1} & m_{b_2b_1} & m_{b_2c_1} & m_{b_2a_2} & m_{b_2b_2} & m_{b_2c_2} & m_{b_2a_3} & m_{b_2b_3} & m_{b_2c_3} \\ m_{c_2a_1} & m_{c_2b_1} & m_{c_2c_1} & m_{c_2a_2} & m_{c_2b_2} & m_{c_2c_2} & m_{c_2a_3} & m_{c_2b_3} & m_{c_2c_3} \\ m_{a_3a_1} & m_{a_3b_1} & m_{a_3c_1} & m_{a_3a_2} & m_{a_3b_2} & m_{a_3c_2} & m_{a_3a_3} & m_{a_3b_3} & m_{a_3c_3} \\ m_{b_3a_1} & m_{b_3b_1} & m_{b_3c_1} & m_{b_3a_2} & m_{b_3b_2} & m_{b_3c_2} & m_{b_3a_3} & m_{b_3b_3} & m_{b_3c_3} \\ m_{c_3a_1} & m_{c_3b_1} & m_{c_3c_1} & m_{c_3a_2} & m_{c_3b_2} & m_{c_3c_2} & m_{c_3a_3} & m_{c_3b_3} & m_{c_3c_3} \end{bmatrix} \tag{2.5}$$

As expected, the stator inductance matrix is symmetrical. Generally, the coefficients of the inductance matrix are a function of the rotor position (anisotropic rotor). However, in this case, the rotor is isotropic therefore the coefficients of the inductance matrix are not a function of the rotor position. Thus, in order to determine the first row of the inductance matrix by using the FE analysis, the coercivity of the magnets must be set to zero, the phase a of sector 1 has to be supplied with a constant current and the flux in the other

phases has to be calculated. The same is done by supplying the other phases and the coefficients of the matrix have been calculated as explained in eq. (2.6):

$$\begin{aligned} m_{k_j k_j} &= \left.\frac{\varphi_{k_j}}{i_{kj}}\right|_{\substack{i_{kj}\neq 0 \\ i_{ht}=0}} \quad \forall h \wedge \forall t \neq j \\ m_{k_j h_t} &= \left.\frac{\varphi_{h_t}}{i_{k_j}}\right|_{\substack{i_{k_j}\neq 0 \\ i_{h_t}=0}} \quad \forall h \wedge \forall t \neq j \end{aligned} \tag{2.6}$$

with $k = a, b, c$, $h = a, b, c$, $j = 1, 2, 3$ and $t = 1, 2, 3$.

FEMM is the software used to perform the inductance matrix calculation. Only one phase is supplied with a constant current of 1A and the linked flux with the other phases is calculated as shown in fig. 2.4:

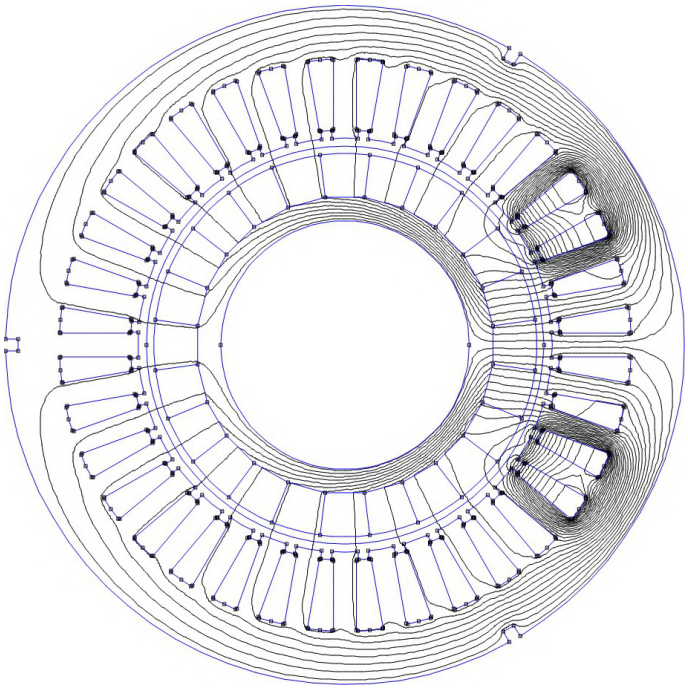

Figure 2.4: Inductance Matrix calculation (example)

The linked flux for each slot is calculated with FEMM software by solving a magneto-static problem, performed by using the magnetic potential vector approach.

The result of the Inductance matrix calculation is expressed in (2.7):

$$\mathbf{M} = \begin{bmatrix} 0.1804 & -0.054 & -0.054 & -0.0173 & 0.0175 & 0.0172 & -0.0173 & 0.0172 & 0.0175 \\ -0.054 & 0.1804 & 0.0164 & 0.0172 & -0.0173 & -0.0172 & 0.0175 & -0.0173 & -0.0185 \\ -0.054 & 0.0164 & 0.1804 & 0.0175 & -0.0185 & -0.0173 & 0.0172 & -0.0172 & -0.0173 \\ -0.0173 & 0.0172 & 0.0175 & 0.1804 & -0.054 & -0.054 & -0.0173 & 0.0175 & 0.0172 \\ 0.0175 & -0.0173 & -0.0185 & -0.054 & 0.1804 & 0.0164 & 0.0172 & -0.0173 & -0.0172 \\ 0.0172 & -0.0172 & -0.0173 & -0.054 & 0.0164 & 0.1804 & 0.0175 & -0.0185 & -0.0173 \\ -0.0173 & 0.0175 & 0.0172 & -0.0173 & 0.0172 & 0.0175 & 0.1804 & -0.054 & -0.054 \\ 0.0172 & -0.0173 & -0.0172 & 0.0175 & -0.0173 & -0.0185 & -0.054 & 0.1804 & 0.0164 \\ 0.0175 & -0.0185 & -0.0173 & 0.0172 & -0.0172 & -0.0173 & -0.054 & 0.0164 & 0.1804 \end{bmatrix} [mH] \tag{2.7}$$

Predictably, the inductance matrix is symmetrical and the self-inductances are the same for each phase. But it is not a cycling matrix, so, if the generalized Clark transformation (9x9) is applied the result will not be a diagonal matrix. Considering the inductance matrix formulation, the linked flux with the k_j-th phase can be expressed as in (2.8)

$$\varphi_{k_j} = \varphi_{PM,k_j} + \sum_{\substack{h=a,b,c \\ t=1,2,3}} m_{h_t k_j} i_{k_j} \tag{2.8}$$

with φ_{PM,k_j} the linked flux with the phase k_j-th produced by the permanent magnets and $m_{h_t k_j}$ the mutual inductance between the h_t-th phase and the k_j-th phase.

So the derivative with respect to the time becomes:

$$\frac{d\varphi_{k_j}}{dt} = \frac{d\varphi_{PM,k_j}}{dt} + \sum_{\substack{h=a,b,c \\ t=1,2,3}} m_{h_t k_j} \frac{di_{k_j}}{dt} = e_{j_k} + \sum_{\substack{h=a,b,c \\ t=1,2,3}} m_{h_t k_j} \frac{di_{k_j}}{dt} \tag{2.9}$$

Where $e_{j_k} = \frac{d\varphi_{PM,j_k}}{dt}$ is the back-EMF (electromotive force) induced in the j_k-th phase due to the PM flux. Thus the eq. (2.1) becomes:

$$v_{k_j} = R_s i_{k_j} + \sum_{\substack{h=a,b,c \\ t=1,2,3}} m_{h_t k_j} \frac{di_{k_j}}{dt} + e_{j_k} \tag{2.10}$$

The eq. (2.10) allows the implementation of the numerical model of the machine as it will be explained further.

2.2.2 Back-emf calculation

In order to implement the stator voltage equation, it is necessary to calculate the back-EMFs induced in the stator windings by the rotor magnets during the machine rotation for different rotational speeds.

To calculate the back-EMFs (electromotive forces) induced by the rotor magnets in the stator windings, the currents are set to 0 and only the magnets' flux is present. For each rotor position, the flux linked with the stator windings is calculated, and then the derivative of the flux is calculated. Solving this problem will also help to calculate the no-load torque (cogging torque). In order to calculate the back-EMFs induced in the k_j-th phase, the flux linked with the phase produced by the magnets has to be derived with respect to the time.

To eliminate the dependence on time it is possible to reformulate the expression of the derivative by exploiting some rules of derivation as expressed in eq. (2.11):

$$e_{k_j} = \frac{d\varphi_{PM,k_j}(\theta_e(t))}{dt} = \frac{d\varphi_{PM,k_j}(\theta_e(t))}{dt}\frac{d\theta_e}{dt} = \frac{d\varphi_{PM,k_j}}{d\theta_e}\omega_e = p\frac{d\varphi_{PM,k_j}}{d\theta_e}\omega_m \tag{2.11}$$

With:

- φ_{PM,k_j} linked flux with the k_j-th phase;
- $\theta_e = p\theta_m$ rotor electrical position;
- ω_m rotational mechanical speed [rad/s];
- p pole pairs;

The advantage of adopting this formulation is that once $\frac{d\varphi_{PM,k_j}}{d\theta_e}$ has been calculated, it is possible to calculate the back-EMF for every mechanical speed.

Figure 2.5 shows the linked fluxes with each stator phase produced by magnets and the back-EMFs at 3000 rpm induced in each phase.

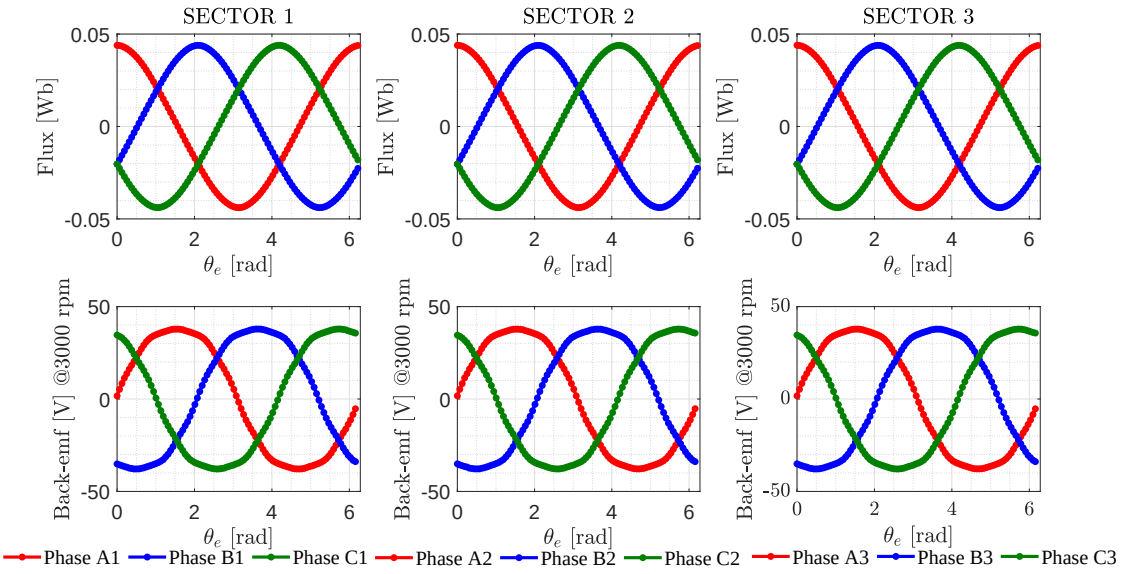

Figure 2.5: Magnets linked fluxes with each stator phase and back-EMF waveforms at 3000rpm

The electrical position of the rotor is shown on the x-axis but it can be converted in time by dividing it by the mechanical speed:

$$\theta_m = \omega_m t \rightarrow t = \frac{\theta_m}{\omega_m} \tag{2.12}$$

Due to the machine symmetry, the flux and the back-emfs are the same in the three sectors of the machine as shown in fig. 2.5, since they are located in an equivalent electrical position. The back-emfs are analyzed using the FFT (Fast Fourier Transform) and the amplitude spectrum of the fluxes is reported in fig. 2.6 While the amplitude spectrum of the back-emfs is reported in fig. 2.7.

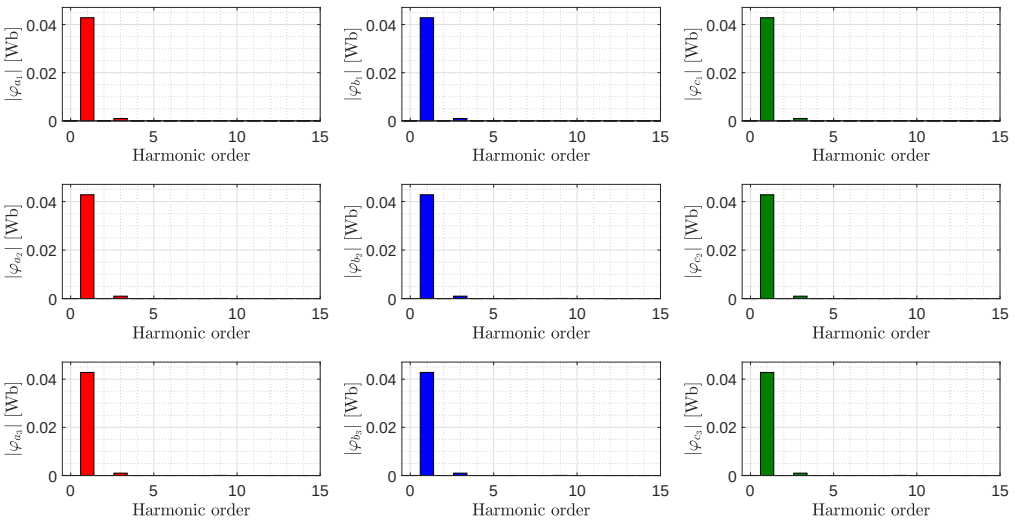

Figure 2.6: Fluxes amplitude spectrum

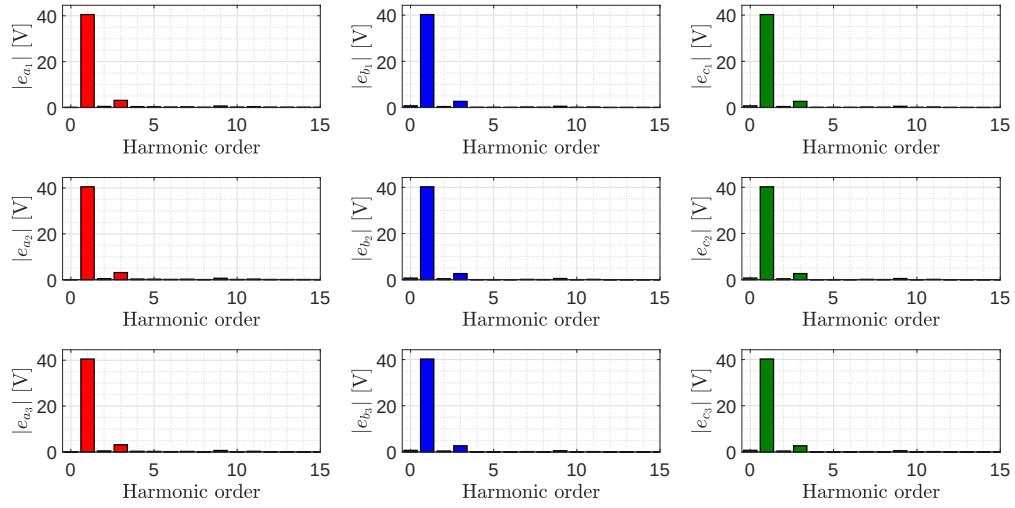

Figure 2.7: Back-emfs amplitude spectrum

The back-emf FFT spectrum is shown also in logarithmic scale in fig. 2.8.

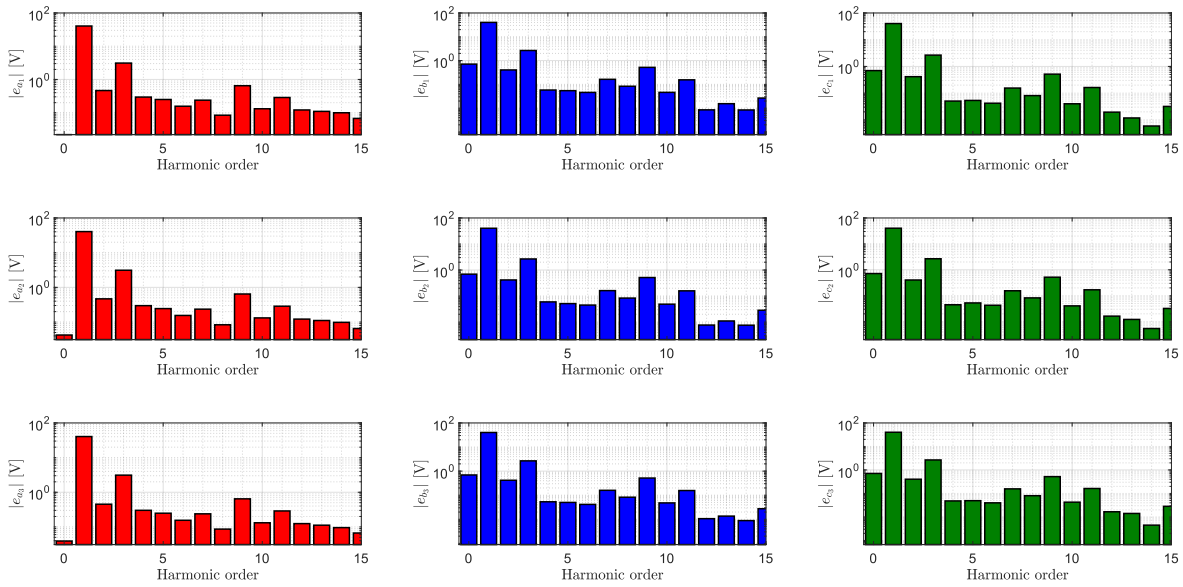

Figure 2.8: Back-emfs amplitude spectrum (log scale)

The harmonic components of the fluxes and back-emf waveforms, higher than the 1st order, present a very low amplitude. This is due to the Halbach array magnet configuration that is able to produce a very sinusoidal and distortion-free waveform of the magnetic field at the air gap.

2.2.3 Wrench Mapping

The relationship between the wrench (torque and forces) acting on the rotor and the currents in the machine can be expressed by using the matrix K_{abc} as explained in eq. (1.2):

$$\overline{W}_E = \mathbf{K}_{abc}(\theta_e)\bar{i}_{abc}$$

Where:

- $\overline{W}_E = [F_x, F_y, T]^T$ is the vector of the wrench components, i.e., the x and y mechanical forces and the torque;
- $\bar{i}_{abc} = [i_{a_1}, i_{b_1}, i_{c_1}, i_{a_2}, i_{b_2}, i_{c_2}, i_{a_3}, i_{b_3}, i_{c_3}]^T$ is the vector of the abc phase currents of each of the three-sector sub windings;
- $\mathbf{K_{abc}}(\theta_e)$ is the $3 \times 3n_s$ matrix that can be expressed as shown in Eq. (2.13):

$$\mathrm{K}_{abc}(\theta_e) = \begin{bmatrix} K_{F_x,a_1}(\theta_e) & K_{F_x,b_1}(\theta_e) & K_{F_x,c_1}(\theta_e) & K_{F_x,a_2}(\theta_e) & K_{F_x,b_2}(\theta_e) & K_{F_x,c_2}(\theta_e) & K_{F_x,a_3}(\theta_e) & K_{F_x,b_3}(\theta_e) & K_{F_x,c_3}(\theta_e) \\ K_{F_y,a_1}(\theta_e) & K_{F_y,b_1}(\theta_e) & K_{F_y,c_1}(\theta_e) & K_{F_y,a_2}(\theta_e) & K_{F_y,b_2}(\theta_e) & K_{F_y,c_2}(\theta_e) & K_{F_y,a_3}(\theta_e) & K_{F_y,b_3}(\theta_e) & K_{F_y,c_3}(\theta_e) \\ K_{T,a_1}(\theta_e) & K_{T,b_1}(\theta_e) & K_{T,c_1}(\theta_e) & K_{T,a_2}(\theta_e) & K_{T,b_2}(\theta_e) & K_{T,c_2}(\theta_e) & K_{T,a_3}(\theta_e) & K_{T,b_3}(\theta_e) & K_{T,c_3}(\theta_e) \end{bmatrix} \quad (2.13)$$

It is important to consider that each coefficient is in general also a function of the stator currents. However, considering the linear behavior of the magnetic material in the main working operation of the electrical machine, for the calculation of these coefficients the current dependency is neglected. Highlighting the coefficient for each sector the relation between the wrench and the stator currents can be expressed as in eq. (2.14):

$$\overline{W}_E = [\mathbf{K}_{abc,1}, \mathbf{K}_{abc,2}, \mathbf{K}_{abc,3}]\,\bar{i}_{abc} \quad (2.14)$$

The wrench mapping consists of the calculation of the suspension forces (along x and y) and the torque, starting from the phases currents for each position of the rotor. Only one phase at a time is supplied and the rotor is rotated, simulating 100 steps, by an angle of $\frac{2\pi}{p}$. Levering on the geometrical and electromagnetic symmetries of the machine, the wrench mapping is made only for sector 1 (only $\mathbf{K}_{abc,1}$ is calculated by using FEMM) and the matrices $\mathbf{K}_{abc,2}$ and $\mathbf{K}_{abc,3}$ are obtained by rotating the first matrix as explained in eq. (2.15):

$$\begin{aligned} \mathbf{K}_{abc,2} &= \mathbf{R_2}\mathbf{K}_{abc,1} \\ \mathbf{K}_{abc,3} &= \mathbf{R_3}\mathbf{K}_{abc,1} \end{aligned} \quad (2.15)$$

Where $\mathbf{R_2}$ and $\mathbf{R_3}$ are the rotational matrix for sectors 2 and 3. In general, the rotational matrix for the k-th sector can be expressed as in eq. (2.16):

$$\mathbf{R_k} = \begin{bmatrix} cos\left(\frac{2\pi}{p}(1-k)\right) & -sin\left(\frac{2\pi}{p}(1-k)\right) & 0 \\ sin\left(\frac{2\pi}{p}(1-k)\right) & cos\left(\frac{2\pi}{p}(1-k)\right) & 0 \\ 0 & 0 & 1 \end{bmatrix} \qquad k = 1, 2, 3 \tag{2.16}$$

The data obtained from the wrench mapping are stored in a $3D$ matrix where every layer (or page) is for a different position of the rotor as shown in fig. 2.9:

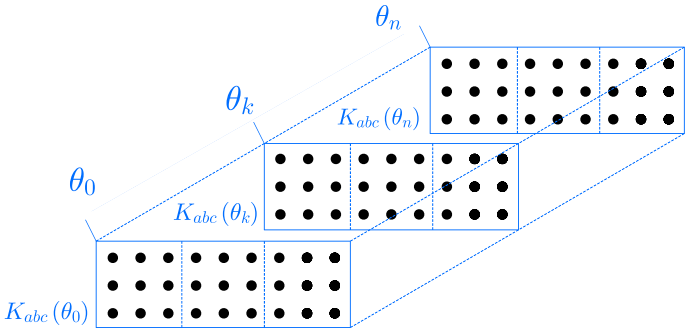

Figure 2.9: Matrix $\mathbf{K_{abc}}(\theta_e)$ data structure

Current Amplitude selection for the Wrench mapping

To comprehend the dependency of the matrix $\mathbf{K_{abc}}$ coefficient on the current, the wrench, for only the $\theta_e = 0°$ rotor position, is calculated for different values of current circulating through phase a_1. Indeed for $\theta_e = 0°$ the force acts only along x as shown in fig. 2.10 and in this way it is possible to understand the dependency of the wrench over the current.

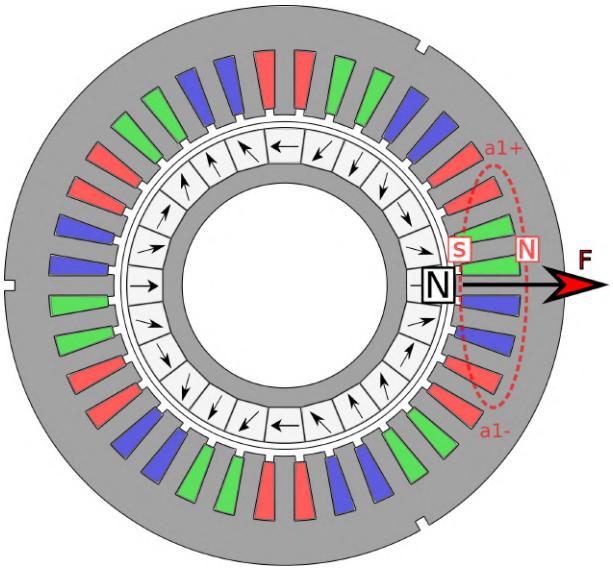

Figure 2.10: $\overline{F}$ direction for $\theta_e = 0°$ and phase a_1 supplied only

The result taken from the FEMM analysis of the force along x for different current amplitude is shown in fig. 2.11:

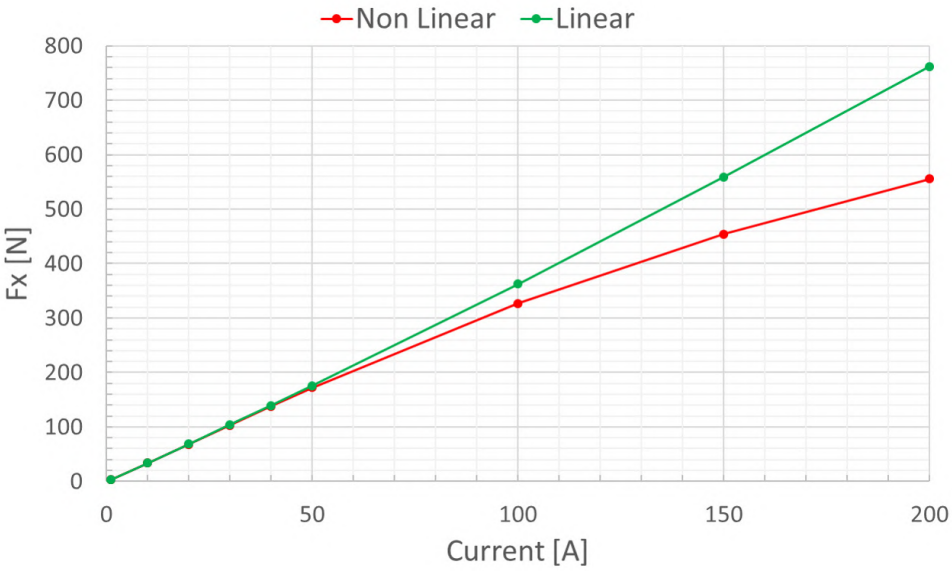

Figure 2.11: Current Amplitude Selection

The wrench mapping is performed in FEMM by setting a current of 50 A (the rated current of the machine). The results of the Wrench mapping obtained supplying one phase of the first sector at a time are reported in fig. 2.12:

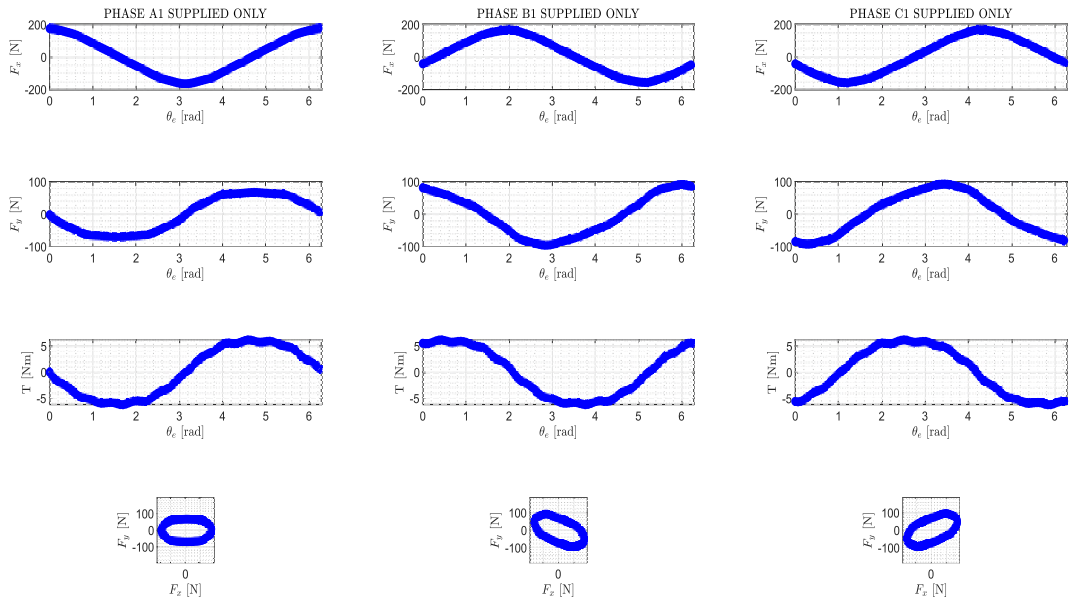

Figure 2.12: FEA (Finite Element Analysis) wrench mapping result for sector 1

Cogging torque mapping

In order to map the cogging torque of the machine zero current is set for each phase and the torque on the rotor is calculated for each position. The result is shown in fig. 2.13:

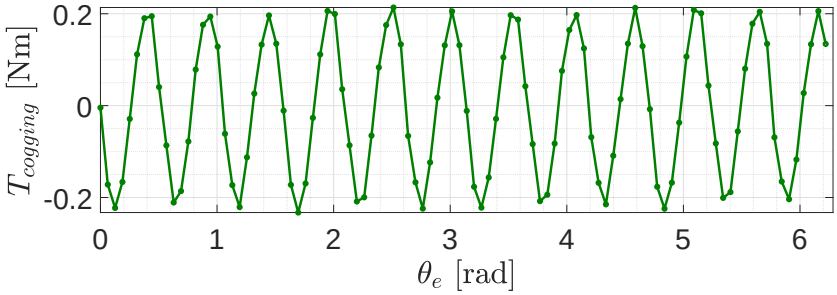

Figure 2.13: Cogging Torque

Matrix $\mathbf{K_{abc}}$ coefficients calculation

Finally, the matrix $\mathbf{K_{abc}}(\theta_e)$ coefficients are calculated as explained in eq. (2.17)

$$\begin{aligned} K_{F_x,k_j}(\theta_e) &= \left.\frac{F_{x,k_j}(\theta_e)}{i_{k_j}}\right|_{\substack{i_{k_j}\neq 0 \\ i_{h_t}=0}} \\ K_{F_y,k_j}(\theta_e) &= \left.\frac{F_{y,k_j}(\theta_e)}{i_{k_j}}\right|_{\substack{i_{k_j}\neq 0 \\ i_{h_t=0}}} \qquad \forall h \wedge \forall t \neq j \\ K_{T,k_j}(\theta_e) &= \left.\frac{T_{k_j}(\theta_e) - T_{cogg}(\theta_e)}{i_{k_j}}\right|_{\substack{i_{k_j}\neq 0 \\ i_{h_t}=0}} \end{aligned} \tag{2.17}$$

In fig. 2.14 is shown the change of the nine $\mathbf{K_{abc,1}}(\theta_\mathbf{e})$ coefficients with respect to the rotor position in an electrical period obtained supplying each phase of the first sector.

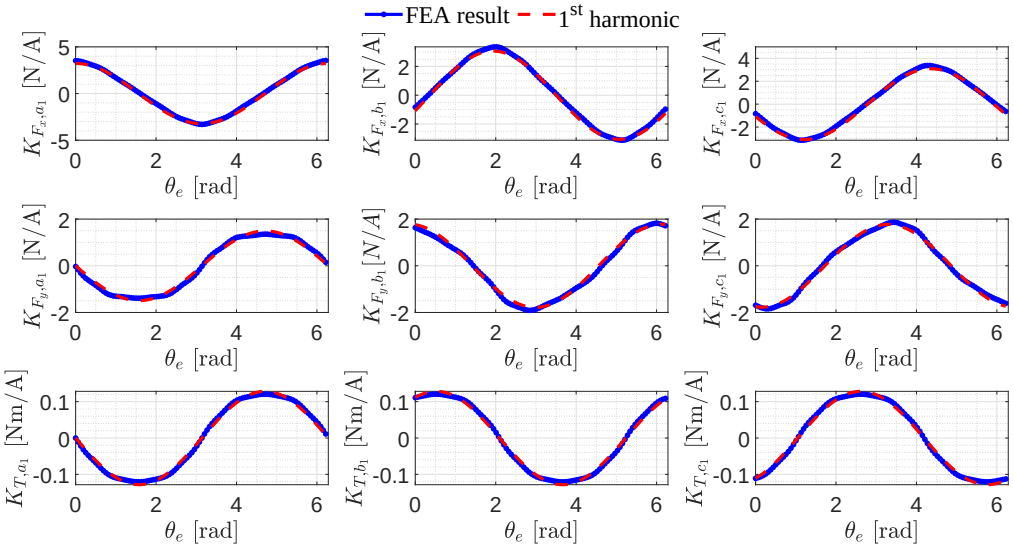

Figure 2.14: Coefficients of the Matrix $\mathbf{K_{abc,1}}(\theta_e)$ for different rotor electrical positions given in an electrical period.

2.2.4 Numerical model of the machine

The numerical model of the machine is implemented in Simulink as shown in fig. 2.15. This model implements the stator phase voltage equations and, starting from the voltages

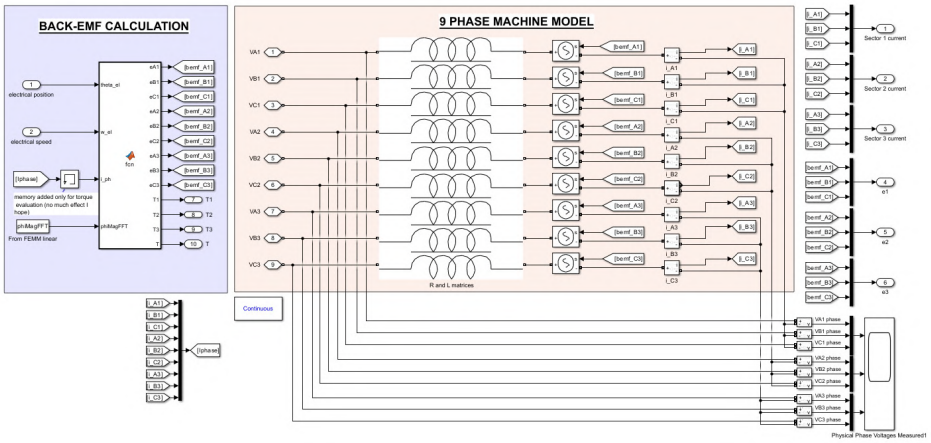

Figure 2.15: Simulink Machine model

applied by the converter, performs the phase currents calculation. The mutual coupling of the stator windings described by the inductance matrix is modelled by using the "Mutual Inductance" Simulink block that allows implementing inductances with mutual coupling.

Simulink Back-emfs calculation

The back-emfs are calculated in Simulink using the FFT Fourier transform and are applied to the machine windings by using a controlled voltage source for each stator winding. Starting from equation (2.11), the linked fluxes produced by the magnets can be expressed in Fourier series as shown in eq. (2.18):

$$\varphi_{PM,k_j}(\theta_e) = \sum_{\rho=0}^{\rho_{max}} |\overline{\varphi}_{PM,k_j,\rho}| cos(\rho\theta_e + \phi_{k_j,\rho}) \tag{2.18}$$

Where:

- ρ is the harmonic order;
- $\phi_{k_j,\rho} = \angle\, \overline{\varphi}_{PM,k_j}$ is the angle of the ρ-th harmonic of the linked flux with phase k_j-th;

The main advantage of adopting the FFT formulation is that it allows the calculation of the back-emf values for every rotor electrical position θ_e.

From (2.18) it is possible to calculate the derivative of the flux with respect to the rotor electrical position as:

$$\frac{d\varphi_{PM,k_j}}{d\theta_e} = -\sum_{\rho=0}^{\rho_{max}} \left[\rho |\overline{\varphi}_{PM,k_j,\rho}| sin(\rho\theta_e + \phi_{k_j,\rho})\right] \tag{2.19}$$

Therefore from eq. (2.11) and eq. (2.19), the back-emfs are calculated as:

$$e_{k_j} = -p\omega_m \sum_{\rho=0}^{\rho_{max}} \left[\rho|\overline{\varphi}_{PM,k_j,\rho}|sin(\rho\theta_e + \phi_{k_j,\rho})\right] \tag{2.20}$$

This calculation has been implemented in a function block in Simulink and, first, tested with a script in Matlab to compare FFT calculation with the FEA results. The comparison, considering up to the 50^{th} harmonic of the FFT series, is represented in fig. 2.16.

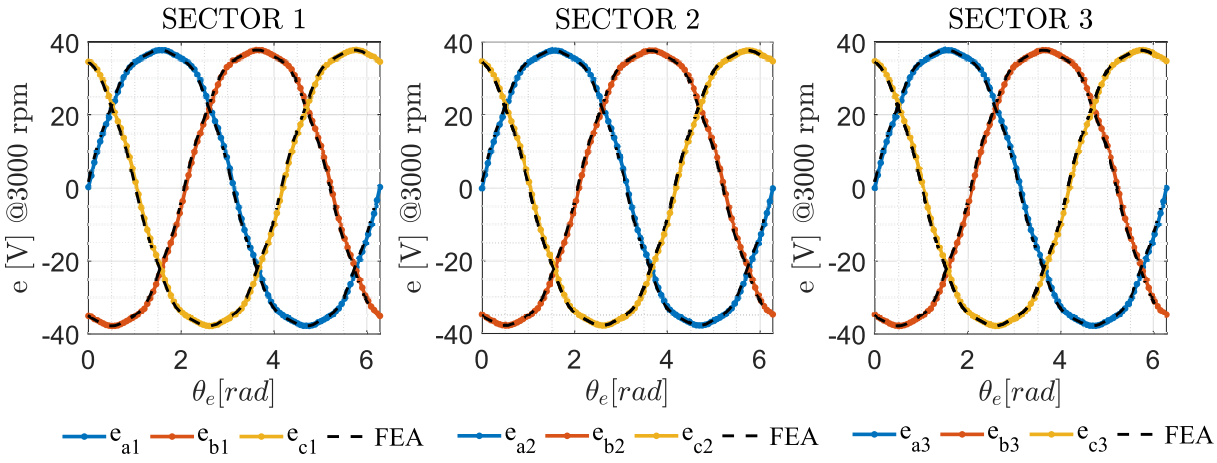

Figure 2.16: FEA and FFT Back-emfs comparison

The calculation performed using the FFT and the calculation obtained for the FEA analysis give the same results.

Wrench Calculation

Considering the phase currents given from the machine model, is it possible to calculate the wrench applied on the machine rotor considering K_{abc} as expressed in the eq. (1.2) reported here:

$$\overline{W}_E = \mathbf{K}_{abc}(\theta_e)\bar{i}_{abc}$$

In order to calculate the wrench for each rotor position (and not only for the rotor position considered during wrench mapping) the coefficients of the matrix $\mathbf{K}_{abc,1}$ are expressed with the FFT series as shown in eq. (2.21):

$$K_{abc,ij}(\theta_e) = \sum_{\rho=0}^{\rho_{max}} |\overline{K}_{abc,ij,\rho}|\ cos(\rho\theta_e + \phi_{ij,\rho})| \tag{2.21}$$

Where:

- ρ is the harmonic order;
- $\overline{K}_{abc,ij,\rho}$ is ρ^{th} harmonic coefficient of the Fourier for the ij^{th} element of the matrix $\mathbf{K_{abc}}$;

- $\phi_{ij,\rho} = \angle\, \overline{K}_{abc,ij,\rho}$ is the angle of the ρ-th harmonic of $K_{abc,ij}$ FFT serial development;

Alternatively, it is also possible to calculate the torque produced by the k_j-th phase current of the machine as:

$$T_{k_j} = \pm \frac{e_{k_j} i_{k_j}}{\omega_m} \tag{2.22}$$

In this way, it is possible to calculate the torque produced by each phase. The total torque is the sum of the torque produced by each phase of each sector:

$$T = \pm \sum_{\substack{k=a,b,c \\ j=1,2,3}} T_{k_j} = \pm \frac{1}{\omega_m} \sum_{\substack{k=a,b,c \\ j=1,2,3}} e_{k_j} i_{k_j} \tag{2.23}$$

In order to verify the torque calculation in Simulink, the torque calculated, by setting $i_q = 10A$ and $i_d = 0A$ in each sector, from:

- eq. (1.2), by using the matrix $\mathbf{K}_{abc}$
- FEA (Finite Element Analysis) performed with FEMM;
- eq. (2.23), by exploiting the product between the currents and the back-emfs

are compared on the same graph in fig. 2.17.

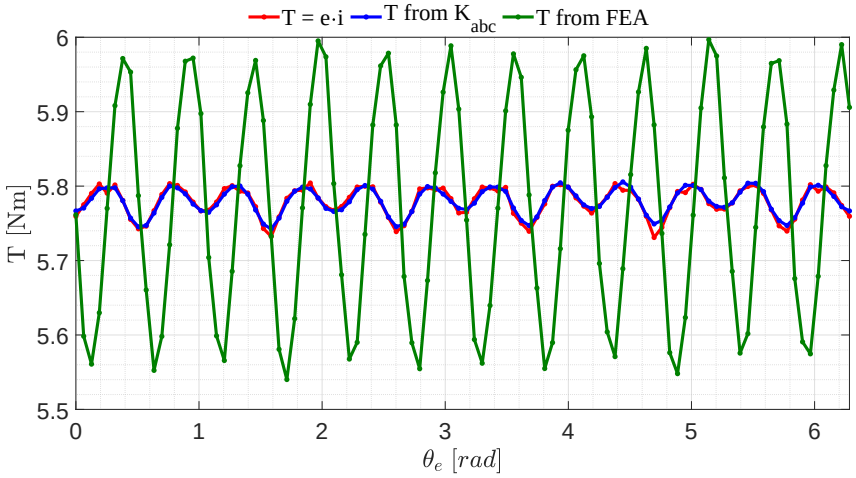

Figure 2.17: Torque Calculation comparison

The mean value of the torque obtained with different calculations is almost the same as in tab. 2.2 but the torque ripple is different.

	Mean Torque
From $\mathbf{K}_{abc}$	5.7615 Nm
$T = \sum e_k i_k$	5.7799 Nm
FEA	5.7789 Nm

Table 2.2: Mean torque comparison

For this reason, the cogging torque has been added to the numerical calculation of the torque performed in Simulink as shown in (2.24).

$$
\begin{aligned}
T &= \pm \frac{1}{\omega_m} \sum_{\substack{k=a,b,c \\ j=1,2,3}} e_{k_j} i_{k_j} + T_{cogg}(\theta_e) \\
[F_x,\ F_y,\ T]^T &= \mathbf{K}_{abc}(\theta_e)\bar{i}_{abc} + [0,\ 0,\ T_{cogg}(\theta_e)]^T
\end{aligned}
\tag{2.24}
$$

The result of this calculation is shown in fig. 2.18. Considering the cogging torque, the torque calculated torque is the same as the torque obtained from the Finite Element Analysis.

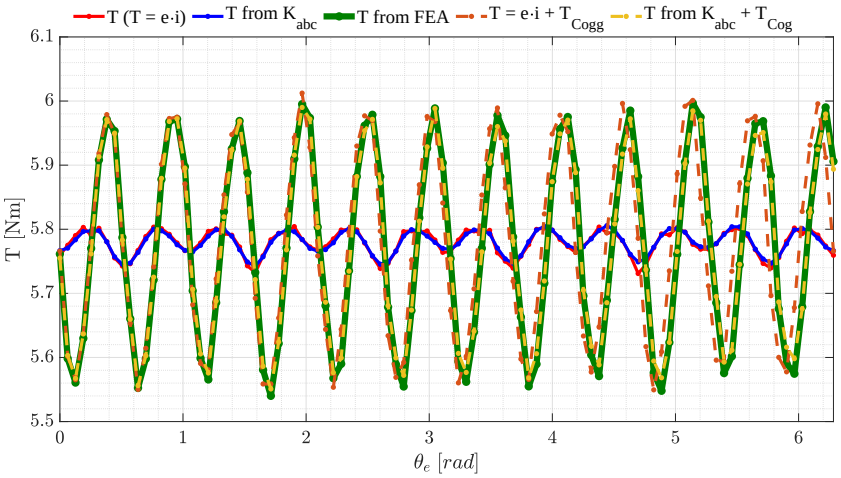

Figure 2.18: Torque Calculation comparison (Cogging Torque considered)

The cogging torque has been processed with FFT in order to obtain the cogging torque for each rotor position.

Chapter 3

Mechanical Model

In this chapter, starting from the second law of the dynamic applied to the rotor, the rotodynamic mechanical model of the machine is developed. The shaft is modeled as a rigid body supported by two flexible supports. Starting from the second law of the dynamic applied to the rotor, the equations that describe the dynamic of the rotor are obtained. Initially, these equations are analyzed neglecting the gyroscopic effect and the elastic coupling, then adding the elastic coupling between the two bearings and the role of the gyroscopic couples. Finally, the damping of the bearings and the out-of-balance force is considered.

3.1 Reference System

In order to develop the rotor mechanical dynamic model is necessary to define a stationary coordinate system, consisting of three mutually perpendicular axes, namely x, y, and z. The three axes intersect at the geometric center of the rotor, initially assumed as the center of the mass of the rotor, i.e., at the point O ($O = [Ox, Oy, Oz]$). The axis of the rotor rotation, at equilibrium, is coincident with the axis z which is assumed to be horizontal. Conversely, the y axis is assumed vertical as shown in fig. 3.1. The axes Ox, Oy, and Oz, in that order, form a right-handed set, which is defined as follows:

- A rotation of a right-handed screw from Ox to Oy advances along Oz;
- A rotation of a right-handed screw from Oy to Oz advances along Ox;
- A rotation of a right-handed screw from Ox to Oz advances along Oy.

The center of mass of the rotor (or the geometric center of the rotor) is allowed to translate along axes Ox, Oy, and Oz by u, v, and w, respectively. The rotor also may rotate (by small amounts) around the axes Ox and Oy by θ_x and θ_y, respectively. Positive values of θ_x and θ_y represent clockwise rotations about axes Ox and Oy, respectively when viewed from the center of mass reference frame (O). Alternatively, it is possible to state that the sense of the rotations is such that positive values of Ox (or Oy), cause a

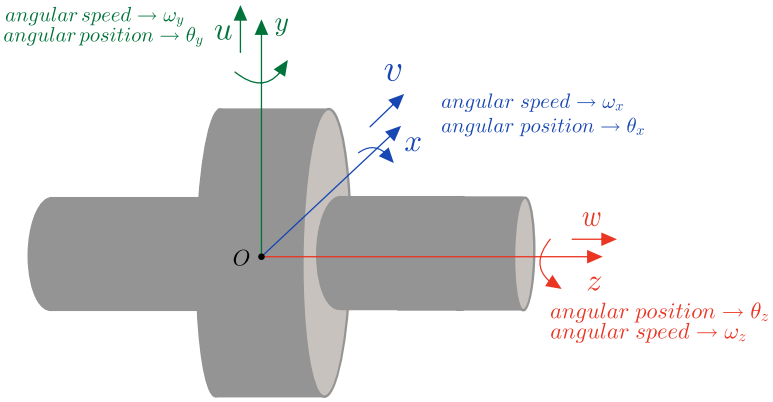

Figure 3.1: Mechanical reference system

right-hand screw to advance along Ox and Oy, respectively. The rotor rotates clockwise about axis Oz with an angular displacement θ_z and an angular velocity $\omega_m = \dot{\theta}_z$. Thus, the sense of this rotation is such that positive values of θ_z cause a right-hand screw to advance along axis Oz.

3.2 Gyroscopic Coupling

In the dynamic analysis of a rotor spinning at speed $\omega_m = \dot{\theta}_z$, it is important to include the effects of gyroscopic couples that arise because of the conservation of angular momentum in the system. These moments are perpendicular to the axis of rotation and are described in detail in [45]. Consider a uniform, circular disk spinning around the z-axis (i.e., the axis of rotation) with a constant angular speed ω_m. The angular momentum of the rotor about Oz is $I_p\omega_m$, where I_p is the polar moment of inertia of the rotor, defined as the moment of inertia around the longitudinal (Oz) or polar axis.
Suppose that the disk now rotates about Oy with an angular velocity of ω_y ($\omega_y = \dot{\theta}_y$). Over time δt, the disk will rotate by an angle of

$$\delta\theta_y = \delta t\dot{\theta}_y \tag{3.1}$$

at the end of this time period, the angular momentum has magnitude $I_p\omega_m$ but its direction is rotated by $\delta\theta_y$, as shown in fig. 3.2.

For an infinitesimal displacement in the axis of rotation $\delta\theta_y$, the vector change in angular momentum has direction Ox and magnitude $M_x\delta t$, where M_x is the clockwise moment about the x-axis. Then:

$$M_x\delta t = I_p\omega_m\delta\theta_y \quad \rightarrow \quad M_x = I_p\omega_m\frac{\delta\theta_y}{\delta t} \tag{3.2}$$

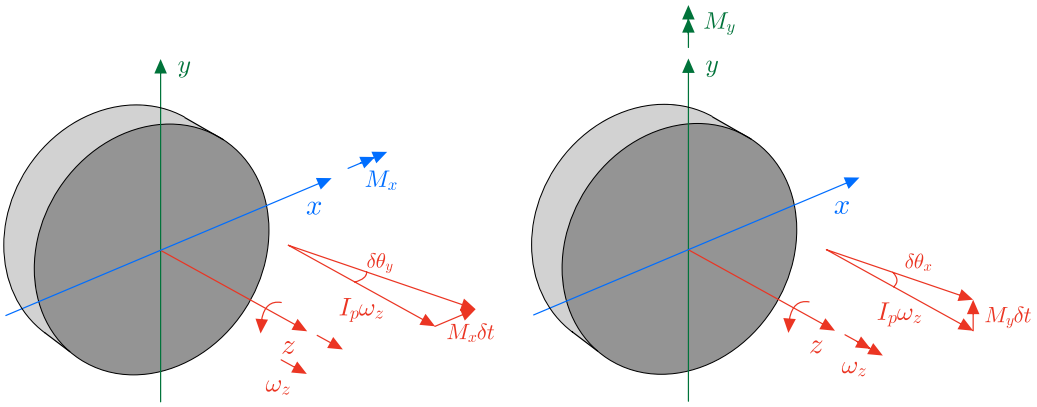

Figure 3.2: Vector diagram showing the effect of a clockwise moment about Ox and Oy

Taking the limit when δt tends to zero:

$$M_x = I_p\omega_m \frac{d\theta_y}{dt} = I_p\omega_m\dot{\theta}_y \tag{3.3}$$

Thus, if a moment M_x is applied about the x-axis, the rotor, while it is spinning about the z-axis, has angular velocity ω_y about the y-axis. This velocity ω_y is referred to as **precession**.

Alternatively, if the spinning rotor is made to precess about the y-axis with an angular velocity ω_y, then a moment M_x must exist about the x-axis in order to close the triangle of momentum vectors and maintain equilibrium.

Consider now that the disk has a constant angular velocity of ω_x about the direction Ox. Over time δt, the disk will rotate by an angle of:

$$\delta\theta_x = \delta t\dot{\theta}_x \tag{3.4}$$

the change in angular momentum is in the negative Oy direction, represented by the screw vector $-M_y\delta t$, in which M_y is the clockwise moment about the y-axis. To close the momentum-vector diagram and maintain equilibrium (fig. 3.2), it must be:

$$-M_y\delta t = I_p\omega_m\delta\theta_x \qquad \rightarrow \qquad M_y = -I_p\omega_m\frac{\delta\theta_x}{\delta t} \tag{3.5}$$

Taking the limit as δt tends to zero:

$$M_y = -I_p\omega_m\frac{d\theta_x}{dt} = -I_p\omega_m\dot{\theta}_x \tag{3.6}$$

In these equations, M_x and M_y are moments due to all the forces acting on the rotor. Because the disk can now rotate simultaneously about the x- and y-axes, the rate of change of angular momentum due to the angular acceleration $I_d\ddot{\theta}_x$ and $I_d\ddot{\theta}_y$ about these axes also needs to be added to the contribution from the disk polar moment of inertia.

Considering the rotational dynamic equation:

$$\begin{aligned} M_x &= I_d \ddot{\theta}_x \\ M_y &= I_d \ddot{\theta}_y \end{aligned} \tag{3.7}$$

Where I_d is the diametral moment of inertia of the disk, defined as the moment of inertia with respect to an axis that is a diameter of the rotor (along x- or y-axis). Hence, Equations (3.4) and (3.6) become:

$$\begin{aligned} M_y = -I_p \omega_m \dot{\theta}_x \quad &\rightarrow \quad I_d \ddot{\theta}_x + I_p \omega_m \dot{\theta}_y = M_x \\ M_x = I_p \omega_m \dot{\theta}_y \quad &\rightarrow \quad I_d \ddot{\theta}_y - I_p \omega_m \dot{\theta}_x = M_y \end{aligned} \tag{3.8}$$

So if the rotor is spinning around the Oz axis:

- a momentum M_x applied along x-axis, causes a variation of the angle θ_y along y and an acceleration $\ddot{\theta}_x$ along x;
- a momentum M_y applied along y-axis, causes a variation of the angle θ_x along x and an acceleration $\ddot{\theta}_y$ along y.

This is explained in figure 3.3:

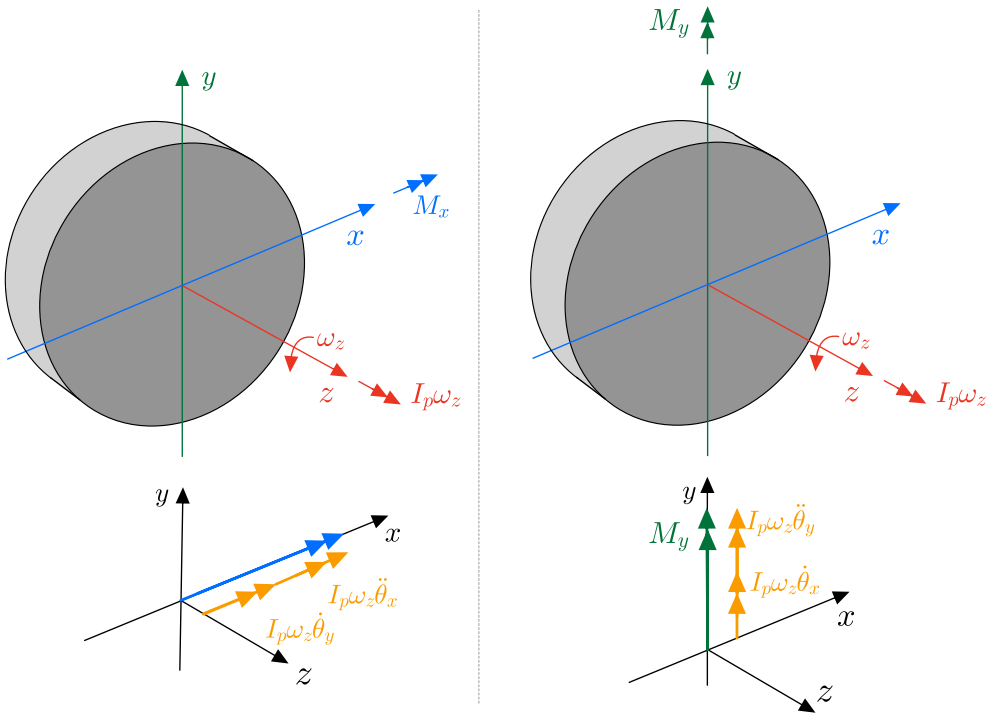

Figure 3.3: Gyroscopic Couples and Vector Diagram

3.3 Rigid Rotor on Flexible supports

The mechanical model developed in this study describes the dynamics of a rigid rotor supported by a pair of bearings, considered flexible as shown in Fig. 3.4.

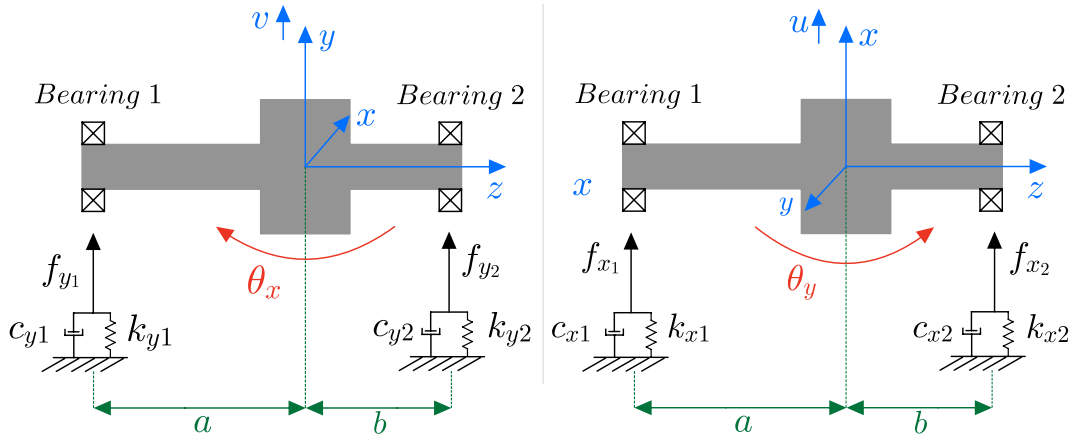

Figure 3.4: Mechanical model: Rigid Shaft supported by two flexible supports

To develop the equations of motion for this system, it is possible to use an energy method (e.g., Lagrange's equations) or, alternatively, directly apply Newton's second law of motion. It has been chosen to use the latter. To do so, the free-body diagram for the system must be drawn as shown in Fig. 3.4. The layout with a permanent rotor is assumed to feature a passive compensation for the translation in the direction Oz (due to the bearings and to the passive magnetic pull of the magnets), and the control of the currents is expected to determine the rotation around this axis. Therefore, the rotor has four degrees of freedom because it can translate in the directions Ox and Oy and it also can rotate about these axes. Often the translation and rotation are called **bounce** and **tilt motion**, respectively.

The description of the rotor movement is performed in terms of the displacements of its center of mass in the directions Ox and Oy, with the coordinates u and v, respectively, and the clockwise rotations about Ox and Oy, θ_x and θ_y, respectively. Applying Newton's second law of motion to the free rotor, yields to:

$$\begin{aligned}
&\textit{Forces along } x \textit{ direction} && -f_{x_1} - f_{x_2} = m\ddot{u} \\
&\textit{Forces along } y \textit{ direction} && -f_{y_1} - f_{y_2} = m\ddot{v} \\
&\textit{Moments along } x \textit{ direction} && -af_{y_1} + bf_{y_2} = I_d\ddot{\theta}_x + I_p\omega_m\dot{\theta}_y \\
&\textit{Moments along } y \textit{ direction} && af_{x_1} - bf_{x_2} = I_d\ddot{\theta}_y - I_p\omega_m\dot{\theta}_x
\end{aligned} \tag{3.9}$$

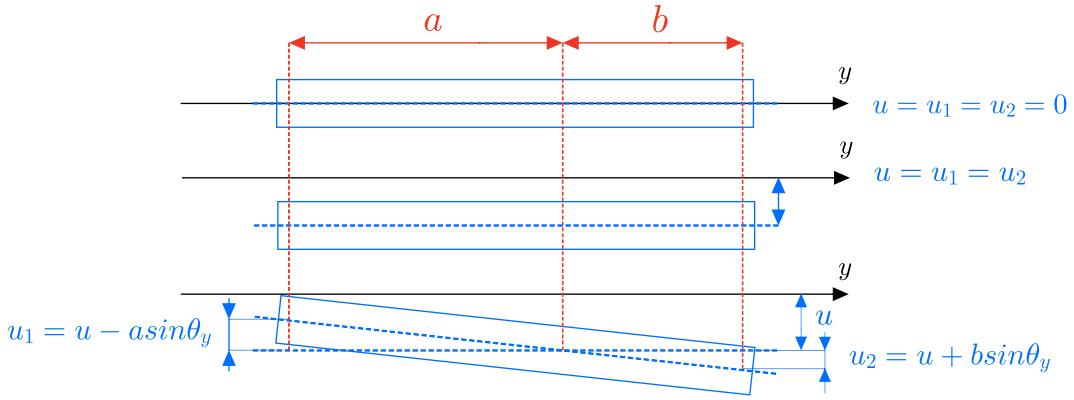

Figure 3.5: Shaft displacement at bearings' locations.

The expressions of the bearings' reaction are in eq. (3.10), and obtained considering fig. 3.5:

$$\begin{aligned} f_{x_1} &= k_{x_1}(u - asin\theta_y) \\ f_{x_2} &= k_{x_2}(u + bsin\theta_y) \\ f_{y_1} &= k_{y_1}(v + asin\theta_x) \\ f_{y_2} &= k_{y_2}(v - bsin\theta_x) \end{aligned} \tag{3.10}$$

Let's assume that the displacements of the rotor from the equilibrium position are small, which is the case in practice (unless there is a catastrophic failure of our rotor-bearing system). This assumption means that the rotations θ_x and θ_y are sufficiently small; hence, it is possible to replace $sin\theta_x$ by θ_x and $sin\theta_y$ by θ_y. Furthermore, the spring supports are assumed linear and the Hooke's law applies.
Then, assuming no elastic coupling between the Ox and Oy directions, the bearing reaction along x at the bearing 1 can be expressed as:

$$f_{x_1} = k_{x_1}(u - asin\theta_y) \approx k_{x_1}(u - a\theta_y) \tag{3.11}$$

where $u - a\theta_y$ is the deflection of the spring due to the force f_{x_1} as shown in fig. 3.5. Applying this argument to each of the forces:

$$\begin{aligned} f_{x_1} &= k_{x_1}(u - a\theta_y) \\ f_{x_2} &= k_{x_2}(u + b\theta_y) \\ f_{y_1} &= k_{y_1}(v + a\theta_x) \\ f_{y_2} &= k_{y_2}(v - b\theta_x) \end{aligned} \tag{3.12}$$

Substituting these forces into equations (3.9) and rearranging gives:

$$\begin{aligned} m\ddot{u} + (k_{x_1} + k_{x_2})u + (-ak_{x_1} + bk_{x_2})\theta_y &= 0 \\ m\ddot{v} + (k_{y_1} + k_{y_2})v + (ak_{y_1} - bk_{y_2})\theta_x &= 0 \\ I_d\ddot{\theta}_x + I_p\omega_m\dot{\theta}_y + (ak_{y_1} - bk_{y_2})v + (a^2k_{y_1} + b^2k_{y_2})\theta_x &= 0 \\ I_d\ddot{\theta}_x - I_p\omega_m\dot{\theta}_y + (ak_{x_1} - bk_{x_2})u + (a^2k_{x_1} + b^2k_{x_2})\theta_y &= 0 \end{aligned} \tag{3.13}$$

Letting:

$$\begin{aligned} k_{x_T} &= k_{x_1} + k_{x_2} & k_{y_T} &= k_{y_1} + k_{y_2} \\ k_{x_C} &= -ak_{x_1} + bk_{x_2} & k_{y_C} &= -ak_{y_1} + bk_{y_2} \\ k_{x_R} &= a^2k_{x_1} + b^2k_{x_2} & k_{y_R} &= a^2k_{y_1} + b^2k_{y_2} \end{aligned} \tag{3.14}$$

where the subscripts T, C, and R have been chosen to indicate transnational, coupling between displacement and rotation, and rotational stiffness coefficients. More specifically, the coefficients k_{x_C} and k_{y_C} describe the coupling between the bearing reactions: the bearing reactions are not independent, but are coupled.
Then, equation (3.13) can be written more concisely as:

$$\begin{aligned} m\ddot{u} + k_{x_T}u + k_{x_C}\theta_y &= 0 \\ m\ddot{v} + k_{y_T}u - k_{y_C}\theta_x &= 0 \\ I_d\ddot{\theta}_x + I_p\omega_m\dot{\theta}_y - k_{y_C}v + k_{y_R}\theta_x &= 0 \\ I_d\ddot{\theta}_x - I_p\omega_m\dot{\theta}_x + k_{x_C}u + k_{x_R}\theta_y &= 0 \end{aligned} \tag{3.15}$$

Finally, the force applied by the multi-sector machine to the rotor $\overline{F} = (F_x, F_y)$ and the second law of the dynamic applied for the rotation around z-axis are added in equations (3.15) as follows:

$$\begin{aligned} m\ddot{u} + k_{x_T}u + k_{x_C}\theta_y &= F_x \\ m\ddot{v} + k_{y_T}u - k_{y_C}\theta_x &= F_y \\ I_d\ddot{\theta}_x + I_p\omega_m\dot{\theta}_y - k_{y_C}v + k_{y_R}\theta_x &= 0 \\ I_d\ddot{\theta}_x - I_p\omega_m\dot{\theta}_x + k_{x_C}u + k_{x_R}\theta_y &= 0 \end{aligned} \tag{3.16}$$

The equation of the rotational dynamic along the z-axis is the well known presented below:

$$T - T_{load} = I_p\frac{d\omega_m}{dt} \tag{3.17}$$

Equations (3.16) and (3.17) are the complete set of equations that describe the lateral response of the shaft when the force $\overline{F} = (F_x, F_y)$ is applied by the electrical machine. The damping of the bearings in these equations is neglected.

3.4 Rigid Rotor on Flexible Isotropic Supports

Let us assume that the flexibility of the bearing supports is the same in both of the transverse directions ($k_{x_1} = k_{y_1}$ and $k_{x_2} = k_{y_2}$); that is, the bearing supports are isotropic. Then, simplifying equation (3.16) by letting:

$$k_{x_T} = k_{y_T} = k_T \qquad k_{x_C} = k_{y_C} = k_C \qquad k_{x_R} = k_{y_R} = k_R \tag{3.18}$$

By introducing these simplifying relationships, equation (3.16) becomes:

$$\begin{aligned} m\ddot{u} + k_T u + k_C \theta_y &= F_x \\ m\ddot{v} + k_T v - k_C \theta_x &= F_y \\ I_d \ddot{\theta}_x + I_p \omega_m \dot{\theta}_y - k_C v + k_R \theta_x &= 0 \\ I_d \ddot{\theta}_x - I_p \omega_m \dot{\theta}_x + k_C u + k_R \theta_y &= 0 \end{aligned} \tag{3.19}$$

3.4.1 Neglecting Gyroscopic Effects and Elastic Coupling

The solutions of the set of equations (3.19) when gyroscopic effects can be neglected are now considered. This is allowed when the speed of rotation is low or the polar moment of inertia is small.
Letting:

$$I_p \omega_m = 0 \tag{3.20}$$

in equations (3.19) gives:

$$\begin{aligned} m\ddot{u} + k_T u + k_C \theta_y &= F_x \\ m\ddot{v} + k_T v - k_C \theta_x &= F_y \\ I_d \ddot{\theta}_x - k_C v + k_R \theta_x &= 0 \\ I_d \ddot{\theta}_x + k_C u + k_R \theta_y &= 0 \end{aligned} \tag{3.21}$$

Now let's consider a solution for the case when

$$k_C = 0 \tag{3.22}$$

This situation arises, for example, if the shaft lengths a and b are equal and the stiffnesses of the bearings are the same at each end of the rotor.

Thus, (3.21) become:

$$\begin{aligned} m\ddot{u} + k_T u &= F_x \\ m\ddot{v} + k_T u &= F_y \\ I_d\ddot{\theta}_x + k_R\theta_x &= 0 \\ I_d\ddot{\theta}_x + k_R\theta_y &= 0 \end{aligned} \tag{3.23}$$

These differential equations are uncoupled and can be solved independently of one another.

Simulink Implementation

In order to implement the differential equations (3.23) in Simulink, the transformation in the Laplace Domain is applied and the second-order derivative term in each equation has been isolated as explained in eq. (3.24):

$$\begin{aligned} \ddot{u} = \frac{F_x - k_T u}{m} \quad &\rightarrow \quad \mathcal{L} \quad \rightarrow \quad u = \frac{1}{s^2}\left(\frac{F_x - k_T u}{m}\right) \\ \ddot{v} = \frac{F_y - k_T u}{m} \quad &\rightarrow \quad \mathcal{L} \quad \rightarrow \quad v = \frac{1}{s^2}\left(\frac{F_y - k_T v}{m}\right) \\ \ddot{\theta}_x = -\frac{k_R}{I_d}\theta_x \quad &\rightarrow \quad \mathcal{L} \quad \rightarrow \quad \theta_x = -\frac{1}{s^2}\frac{k_R}{I_d}\theta_x \\ \ddot{\theta}_y = -\frac{k_R}{I_d}\theta_y \quad &\rightarrow \quad \mathcal{L} \quad \rightarrow \quad \theta_y = -\frac{1}{s^2}\frac{k_R}{I_d}\theta_y \end{aligned} \tag{3.24}$$

Equations (3.24) are implemented in Simulink as explained in fig. 3.6 where is also possible to insert the initial conditions:

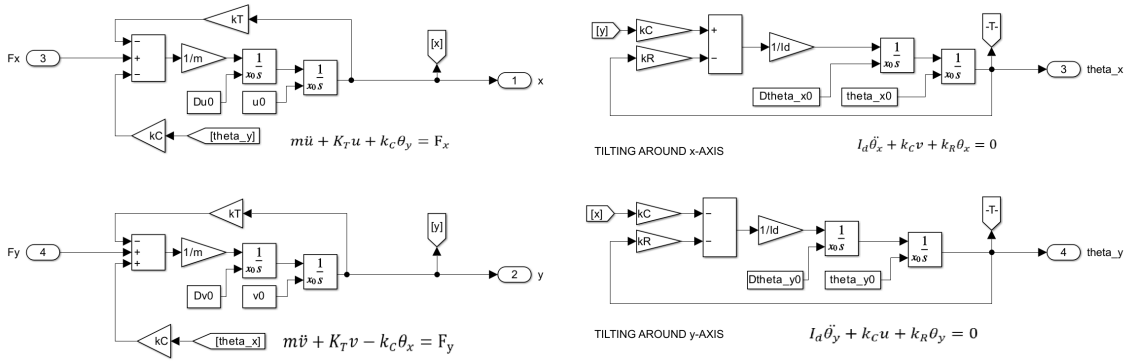

Figure 3.6: Differential equations implemented in Simulink

Setting the parameters in tab. 3.1, a simulation has been run giving as results the shaft displacement at bearings' and center of mass locations shown in fig. 3.7.

Mechanical parameters			Initial Conditions		
k_{x_1}	10	MN/m	$u(t=0)$	10	μm
k_{y_1}	10	MN/m	$v(t=0)$	5	μm
k_{x_2}	10	MN/m	$\theta_x(t=0)$	0	rad
k_{y_2}	10	MN/m	$\theta_y(t=0)$	0	rad
a	0.1769	m	$\dot{u}(t=0)$	30	$\mu m/s$
b	0.2175	m	$\dot{v}(t=0)$	0	$\mu m/s$
I_d	0.156502	kg m^2	$\dot{\theta}_x(t=0)$	0	s^{-1}
I_p	0.010468	kg m^2	$\dot{\theta}_y(t=0)$	0	s^{-1}

Table 3.1: Simulation parameters

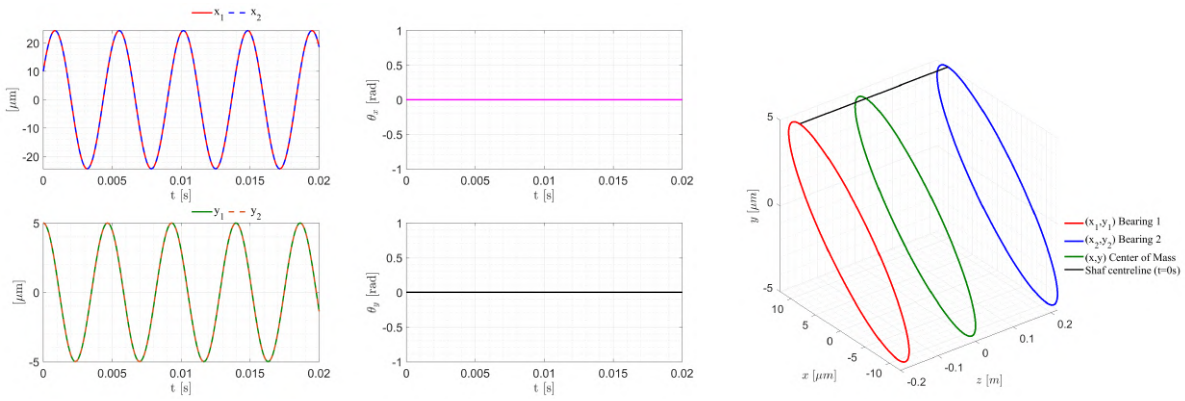

Figure 3.7: x and y displacement of the shaft

From these results, if the gyroscopic effect and the elastic coupling ($k_C = 0$) are neglected, the tilting is zero ($\theta_x = 0$ and $\theta_y = 0$). It is possible to determine the shaft displacement at the location of the bearings considering the shaft as rigid and by applying the eq. (3.25):

$$\begin{aligned} x_1 &= u - asin\theta_y \approx u - a\theta_y \\ x_2 &= u + bsin\theta_y \approx u + b\theta_y \\ y_1 &= v + asin\theta_x \approx v + a\theta_x \\ y_2 &= v - bsin\theta_x \approx v - b\theta_x \end{aligned} \tag{3.25}$$

3.4.2 Neglecting Gyroscopic Effects, Including Elastic Coupling

Now the elastic coupling is considered, so $k_C \neq 0$ and the equations that describe the dynamic of the rotor are:

$$\begin{aligned} m\ddot{u} + k_T u + k_C \theta_y &= F_x \\ m\ddot{v} + k_T v - k_C \theta_x &= F_y \\ I_d\ddot{\theta}_x - k_C v + k_R \theta_x &= 0 \\ I_d\ddot{\theta}_x + k_C u + k_R \theta_y &= 0 \end{aligned} \tag{3.26}$$

Simulink Implementation

In order to implement the differential equations in Simulink, the transformation in the Laplace Domain is applied and the second-order derivative term in each equation has been isolated as explained in eq. (3.27):

$$\begin{aligned}
\ddot{u} &= \frac{F_x - k_T u - k_C \theta_y}{m} \quad \rightarrow \quad \mathcal{L} \quad \rightarrow \quad u = \frac{1}{s^2}\left(\frac{F_x - k_T u - k_C \theta_y}{m}\right) \\
\ddot{v} &= \frac{F_y - k_T v + k_C \theta_x}{m} \quad \rightarrow \quad \mathcal{L} \quad \rightarrow \quad v = \frac{1}{s^2}\left(\frac{F_y - k_T v + k_C \theta_x}{m}\right) \\
\ddot{\theta}_x &= \frac{k_C v - k_R \theta_x}{I_d} \quad \rightarrow \quad \mathcal{L} \quad \rightarrow \quad \theta_x = \frac{1}{s^2}\left(\frac{k_C v - k_R \theta_x}{I_d}\right) \\
\ddot{\theta}_y &= -\frac{k_C u + k_R \theta_y}{I_d} \quad \rightarrow \quad \mathcal{L} \quad \rightarrow \quad \theta_y = -\frac{1}{s^2}\left(\frac{k_C u + k_R \theta_y}{I_d}\right)
\end{aligned} \tag{3.27}$$

Equations (3.27) are implemented in Simulink as explained in fig. 3.8 where is also possible to insert the initial conditions:

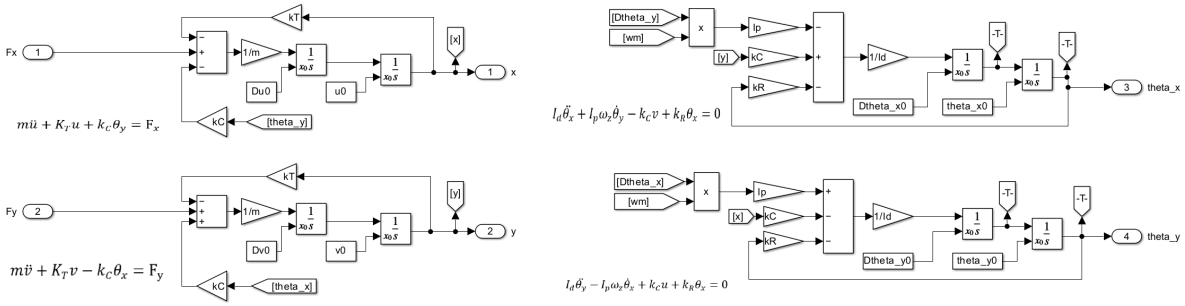

Figure 3.8: Differential equations Simulink implementation

Setting the parameters in tab. 3.1 and the rotational speed $\omega_m = 0$, a simulation has been run giving as results the shaft displacement at bearings' and centre of mass locations shown in fig. 3.9.

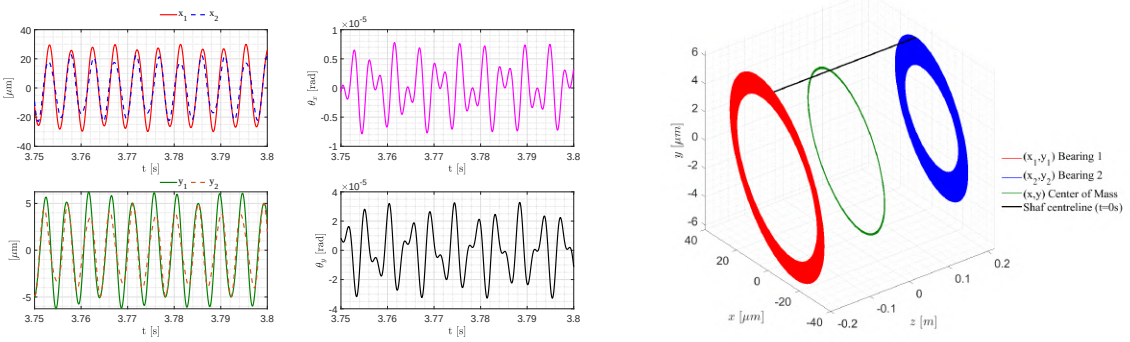

Figure 3.9: x and y displacement of the shaft

As it is possible to see from these results, the effect of the elastic coupling is to introduce a tilting ($\theta_x \neq 0$ and $\theta_y \neq 0$). In particular, the effect of having $\theta_x \neq 0$ and $\theta_y \neq 0$ can lead

to a bounce mode (also called cylindrical mode if the gyroscopic effect is acting) or to a tilting mode (also called conical mode if the gyroscopic effect is acting) as shown in 3.10.

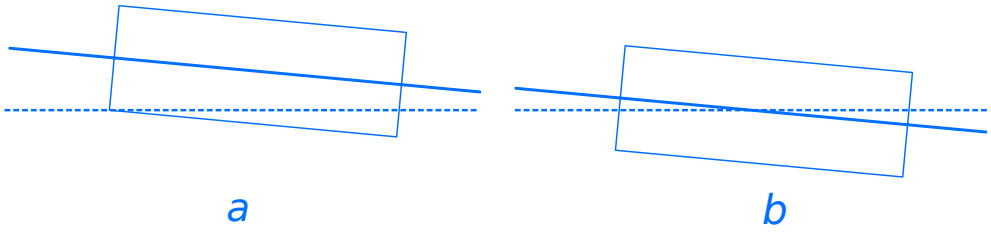

Figure 3.10: Bounce (a) and Tilting (b) mode (the dashed line denotes zero displacement)

3.4.3 Including Gyroscopic Effect

In the previous analysis presented, the effect of gyroscopic couples is neglected. However, in many situations such as overhung rotors or rotors spinning at high speed, it is necessary to consider the effect of gyroscopic couples. To include gyroscopic effects in the analysis of a rigid rotor on isotropic supports, at the beginning Equation (3.19) is considered, which is repeated here for convenience:

$$\begin{aligned} m\ddot{u} + k_T u + k_C \theta_y &= F_x \\ m\ddot{v} + k_T u - k_C \theta_x &= F_y \\ I_d \ddot{\theta}_x + I_p \omega_m \dot{\theta}_y - k_C v + k_R \theta_x &= 0 \\ I_d \ddot{\theta}_x - I_p \omega_m \dot{\theta}_y + k_C u + k_R \theta_y &= 0 \end{aligned} \tag{3.28}$$

Plus the equation of the rotational dynamic along the z-axis:

$$T - T_{load} = I_p \frac{d\omega_m}{dt} \tag{3.29}$$

Simulink Implementation

To implement these equations in Simulink the second-order derivative are isolated and integrated two times:

$$\begin{aligned} \ddot{u} &= \frac{F_x - k_T u - k_C \theta_y}{m} \quad \rightarrow \quad \mathcal{L} \quad \rightarrow \quad u = \frac{1}{s^2}\left(\frac{F_x - k_T u - k_C \theta_y}{m}\right) \\ \ddot{v} &= \frac{F_y - k_T v + k_C \theta_x}{m} \quad \rightarrow \quad \mathcal{L} \quad \rightarrow \quad v = \frac{1}{s^2}\left(\frac{F_y - k_T v + k_C \theta_x}{m}\right) \\ \ddot{\theta}_x &= \frac{k_C v - I_p \omega_m \dot{\theta}_y - k_R \theta_x}{I_d} \quad \rightarrow \quad \mathcal{L} \quad \rightarrow \quad \theta_x = \frac{1}{s^2}\left(\frac{k_C v - I_p \omega_m s\theta_y - k_R \theta_x}{I_d}\right) \\ \ddot{\theta}_y &= \frac{I_p \omega_m \dot{\theta}_x - k_C u - k_R \theta_y}{I_d} \quad \rightarrow \quad \mathcal{L} \quad \rightarrow \quad \theta_y = \frac{1}{s^2}\left(\frac{I_p \omega_m s\theta_x - k_C u - k_R \theta_y}{I_d}\right) \end{aligned} \tag{3.30}$$

The Simulink implementation is the same as the one shown in fig. 3.8, but now the rotational speed ω_m is set to 10000 rpm (in the previous case it was zero, so the gyroscopic effect doesn't affect the dynamic of the rotor).
The results of this simulation are shown in 3.11 and 3.12.

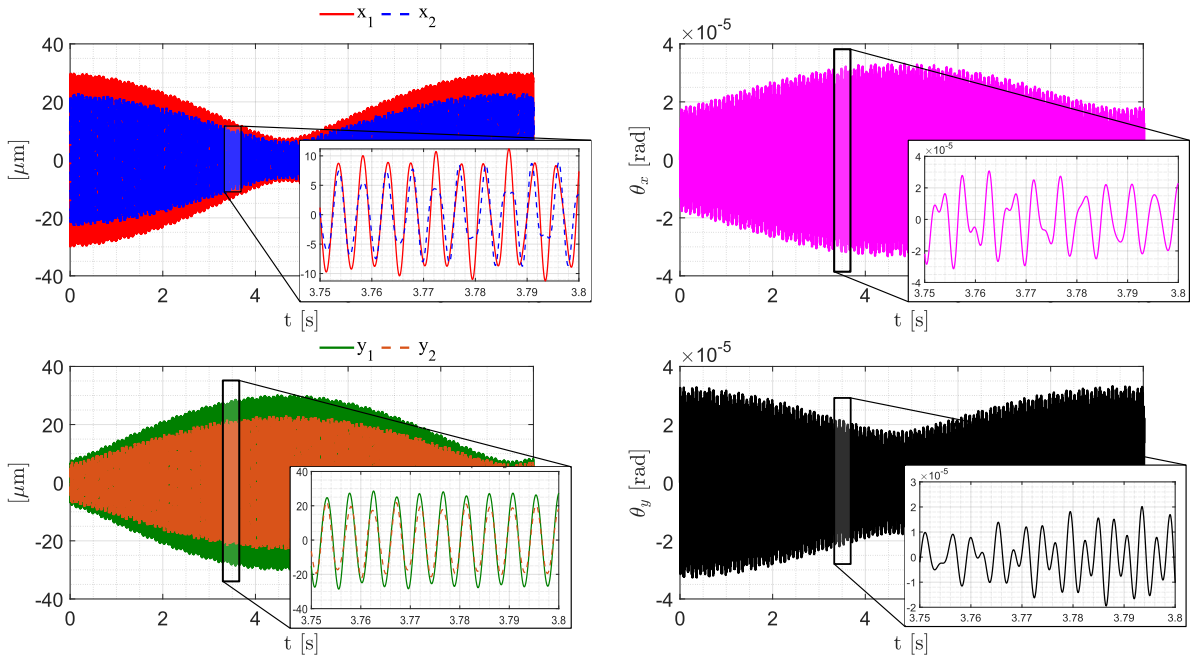

Figure 3.11: Simulation results including gyroscopic effect (x_1, x_2, θ_x and θ_y).

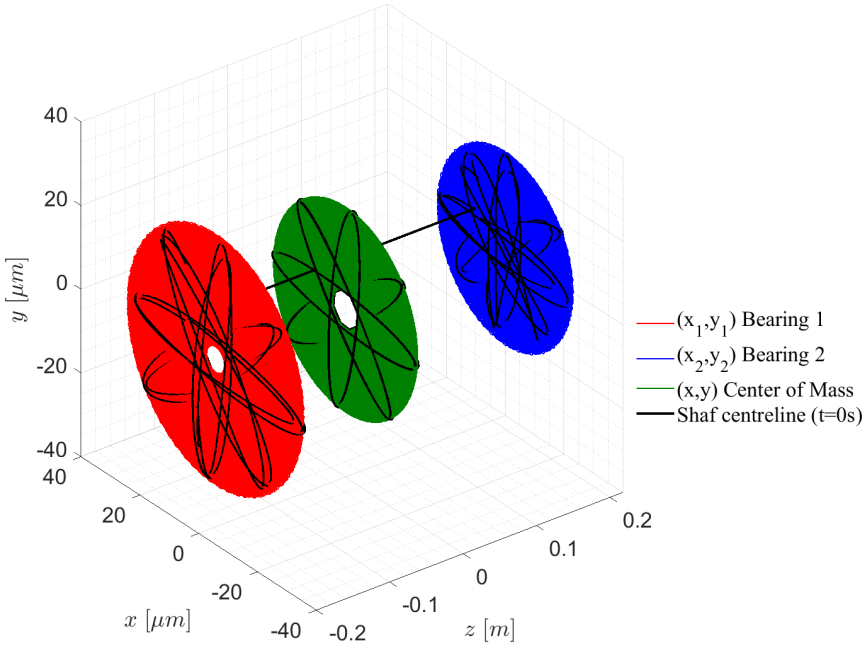

Figure 3.12: Simulation results including gyroscopic effect (x_1, x_2, θ_x and θ_y).

As shown in the figures 3.11 and 3.12, the gyroscopic effect makes the orbit of the shaft at the bearing locations rotate around the z-axis.

3.4.4 Including Damping

The effect of viscous damping in the bearings is now considered. Assuming that a viscous damper is placed in parallel with each spring element supporting the bearing, the bearings reaction forces f_{x_1}, f_{y_1}, f_{x_2} and f_{y_2} contain also the damping component and they are:

$$\begin{aligned} f_{x_1} &= k_{x_1}(u - a\theta_y) + c_{x_1}(\dot{u} - a\dot{\theta}_y) \\ f_{x_2} &= k_{x_2}(u + b\theta_y) + c_{x_2}(\dot{u} - a\dot{\theta}_y) \\ f_{y_1} &= k_{y_1}(v + a\theta_x) + c_{y_1}(\dot{v} - a\dot{\theta}_x) \\ f_{y_2} &= k_{y_2}(v - b\theta_x) + c_{y_2}(\dot{v} - a\dot{\theta}_x) \end{aligned} \tag{3.31}$$

where c is the viscous-damping coefficient and is defined as the force required to produce a unit velocity across the damping element. Let:

$$\begin{aligned} c_{x_T} &= c_{x_1} + c_{x_2} & \qquad c_{y_T} &= c_{y_1} + c_{y_2} \\ c_{x_C} &= -ac_{x_1} + bc_{x_2} & \qquad c_{y_C} &= -ac_{y_1} + bc_{y_2} \\ c_{x_R} &= a^2c_{x_1} + b^2c_{x_2} & \qquad c_{y_R} &= a^2c_{y_1} + b^2c_{y_2} \end{aligned} \tag{3.32}$$

For simplicity isotropic supports ($c_{x1} = c_{y1} = c_1$ and $c_{x2} = c_{y2} = c_2$) are considered so:

$$\begin{aligned} c_T &= c_{x_T} = c_{y_T} = c_1 + c_2 \\ c_C &= c_{x_C} = c_{y_C} = -ac_1 + bc_2 \\ c_R &= c_{x_R} = c_{y_R} = a^2c_1 + b^2c_2 \end{aligned} \tag{3.33}$$

Using these definitions, substituting equations (3.31) into (3.9) and rearranging these equations gives:

$$\begin{aligned} m\ddot{u} + c_T\dot{u} + c_C\dot{\theta}_y + k_Tu + k_C\theta_y &= F_x \\ m\ddot{v} + c_T\dot{v} - c_C\dot{\theta}_x + k_Tv - k_C\theta_x &= F_y \\ I_d\ddot{\theta}_x + I_p\omega_m\dot{\theta}_y - c_C\dot{v} + c_R\dot{\theta}_x - k_Cv + k_R\theta_x &= 0 \\ I_d\ddot{\theta}_y - I_p\omega_m\dot{\theta}_x + c_C\dot{u} + c_R\dot{\theta}_y + k_Cu + k_R\theta_y &= 0 \end{aligned} \tag{3.34}$$

This is the complete set of equations that allows the description of the dynamic of the rotor while taking into account the damping of the supports.

Simulink Implementation

In order to implement these equations the second-order derivative in each equation is isolated as it follows and then integrated twice in the Laplace domain as shown previously:

$$\begin{aligned}
\ddot{u} &= \frac{F_x - c_T\dot{u} - c_C\dot{\theta}_y - k_T u - k_C\theta_y}{m} \\
\ddot{v} &= \frac{F_y - c_T\dot{v} + c_C\dot{\theta}_x - k_T v + k_C\theta_x}{m} \\
\ddot{\theta}_x &= \frac{k_C v + c_C\dot{v} - c_R\dot{\theta}_x - I_p\omega_m\dot{\theta}_y - k_R\theta_x}{I_d} \\
\ddot{\theta}_y &= \frac{I_p\omega_m\dot{\theta}_x - c_C\dot{u} - c_R\dot{\theta}_y - k_C u - k_R\theta_y}{I_d}
\end{aligned} \tag{3.35}$$

The Simulink implementation is shown in 3.13:

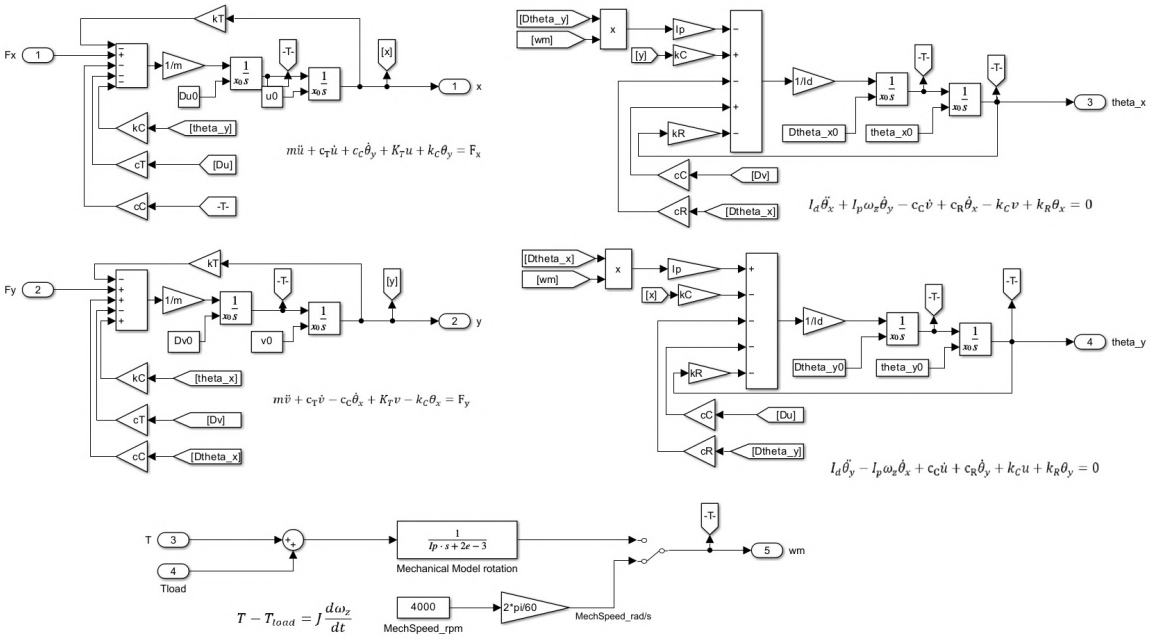

Figure 3.13: Simulink differential equation implementation (including damping)

in order to understand the role of the damping, a simple simulation has been run neglecting the gyroscopic effect ($\omega_m = 0$). The results of the simulation are in figure 3.14 where $c_{x_1} = c_{x_2} = c_{y_1} = c_{y_1} = 500Nm/s$:

As it is possible to see, in the absence of any other forces the damping brings the shaft displacement toward the origin.

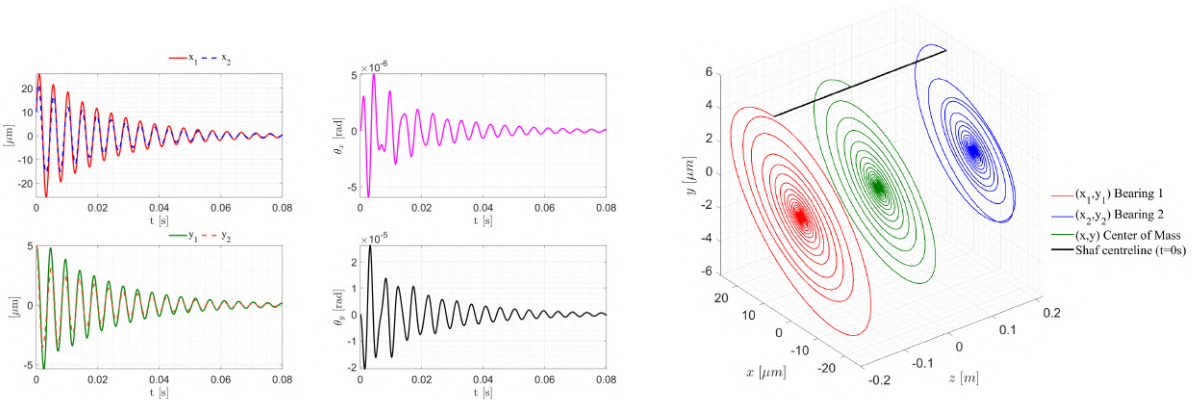

Figure 3.14: x and y displacement of the shaft

3.4.5 Including Out-of-Balance Forces

The most significant lateral forces and moments are usually caused by an imperfect distribution of mass in the rotor. Due to manufacturing tolerances and other factors, it is not possible to ensure that rotors are perfectly balanced. Although when new or recently commissioned, a rotor is balanced so that the residual out-of-balance is minimal, this out-of-balance may increase with the passage of time. As the rotor spins about its equilibrium position, forces and moments are generated that are called out-of-balance forces and moments. The direction of these forces and moments is fixed relative to the rotor. Therefore, their direction rotates with the rotor and for this reason, they are synchronous forces and moments.

To model the out-of-balance force acting on the rotor, the displacement of the rotor centre of mass along axes Ox and Oy must be considered. The instantaneous position of the rotor centerline S is described by (u, v) and the position of the mass centre of the rotor and G is described by (u_G, v_G), while the centre of the references system is O. The distance between S and G two points is $|SG| = \varepsilon$ and the instantaneous angle between the line SG (which represents a line on the rotor) and the Ox axis is θ_z as shown in fig. 3.15.

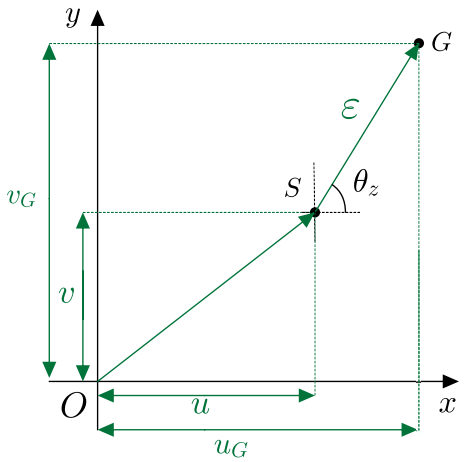

Figure 3.15: Instantaneous position of bearing centerline S and rotor mass center G

From figure 3.15, it is shown that:

$$\begin{aligned} u_G &= u + \varepsilon cos\theta_z \\ v_G &= v + \varepsilon sin\theta_z \end{aligned} \tag{3.36}$$

Differentiating these equations twice with respect to time, with ε constant, gives:

$$\begin{aligned} \ddot{u}_G &= \ddot{u} + \varepsilon(-\dot{\theta}_z^2 cos\theta_z - \ddot{\theta}_z sin\theta_z) \\ \ddot{v}_G &= \ddot{v} + \varepsilon(-\dot{\theta}_z^2 sin\theta_z + \ddot{\theta}_z cos\theta_z) \end{aligned} \tag{3.37}$$

In deriving the previous equation, the analysis of the case of a rotor spinning with a constant angular velocity is not restricted. If now this simplification is introduced, then at a constant speed of rotation $\dot{\theta}_z = \omega_z = \omega_m$, it becomes $\ddot{\theta}_z = 0$. Thus:

$$\begin{aligned} \ddot{u}_G &= \ddot{u} - \varepsilon\omega_z^2 cos\theta_z \\ \ddot{v}_G &= \ddot{v} - \varepsilon\omega_z^2 sin\theta_z \end{aligned} \tag{3.38}$$

For the rotor being considered, the center of mass is offset from the shaft centerline at equilibrium by a small quantity ε, and the displacement of the center of mass is given by u_G and v_G, However, the displacements of the springs and dampers (at the bearings) are still in terms of u and v. Thus, replacing $\ddot{u}$ by $\ddot{u}_G$ and $\ddot{v}$ by $\ddot{u}_G$ in (3.34):

$$\begin{aligned} m\ddot{u}_G + c_T\dot{u} + c_C\dot{\theta}_y + k_T u + k_C\theta_y &= F_x \\ m\ddot{v}_G + c_T\dot{v} - c_C\dot{\theta}_x + k_T v - k_C\theta_x &= F_y \\ I_d\ddot{\theta}_x + I_p\omega_z\dot{\theta}_y - c_C\dot{v} + c_R\dot{\theta}_x - k_C v + k_R\theta_x &= 0 \\ I_d\ddot{\theta}_y - I_p\omega_z\dot{\theta}_x - c_C\dot{u} + c_R\dot{\theta}_y + k_C u + k_R\theta_y &= 0 \end{aligned} \tag{3.39}$$

The equations of motion of this rotor, including damping at the supports and gyroscopic effects, are given in equations (3.34). Substituting for $\ddot{u}_G$ and $\ddot{u}_G$ from equation (3.38) and rearranging gives:

$$\begin{aligned} m\ddot{u} + c_T\dot{u} + c_C\dot{\theta}_y + k_T u + k_C\theta_y &= F_x + m\varepsilon\omega_z^2 cos(\omega_m t) \\ m\ddot{v} + c_T\dot{v} - c_C\dot{\theta}_x + k_T v - k_C\theta_x &= F_y + m\varepsilon\omega_z^2 sin(\omega_m t) \\ I_d\ddot{\theta}_x + I_p\omega_m\dot{\theta}_y - c_C\dot{v} + c_R\dot{\theta}_x - k_C v + k_R\theta_x &= 0 \\ I_d\ddot{\theta}_y - I_p\omega_m\dot{\theta}_x + c_C\dot{u} + c_R\dot{\theta}_y + k_C u + k_R\theta_y &= 0 \end{aligned} \tag{3.40}$$

Equation (3.40) shows that the lateral offset of the mass center from the equilibrium position causes out-of-balance forces to act on the system. Thus, the equations of motion for a system with a disk or rotor with an offset either can be developed by modifying the position of the center of mass or more directly by adding forces on the right-hand side of the equations of motion.

Simulink Implementation

In order to implement these equations the second-order derivative in each equation is isolated as already presented and then integrated twice in the Laplace domain as shown previously:

$$\begin{aligned}
\ddot{u} &= \frac{F_x + m\varepsilon\omega_z^2 cos(\omega_z t) - c_T\dot{u} - c_C\dot{\theta}_y - k_T u - k_C\theta_y}{m} \\
\ddot{v} &= \frac{F_y + m\varepsilon\omega_z^2 sin(\omega_z t) - c_T\dot{v} + c_C\dot{\theta}_x - k_T v + k_C\theta_x}{m} \\
\ddot{\theta}_x &= \frac{k_C v + c_C\dot{v} - c_R\dot{\theta}_x - I_p\omega_m\dot{\theta}_y - k_R\theta_x}{I_d} \\
\ddot{\theta}_y &= \frac{I_p\omega_m\dot{\theta}_x - c_C\dot{u} - c_R\dot{\theta}_y - k_C u - k_R\theta_y}{I_d}
\end{aligned} \tag{3.41}$$

The Simulink implementation is shown in figure 3.16. Considering an acceleration of

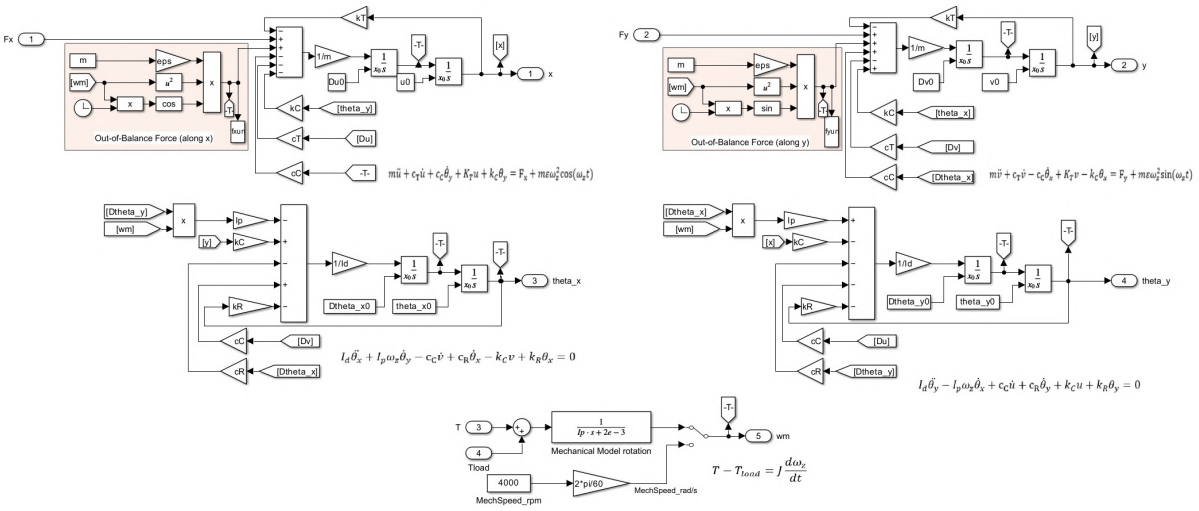

Figure 3.16: Simulink implementation of the differential equations (3.41).

the rotor from 0 rpm to 10000 rpm, the results of the simulation, with the considered parameter in table 3.2, are shown in 3.17, 3.18 and 3.19.

Mechanical parameters			Initial Conditions		
k_{x_1}	10	MN/m	$u(t=0)$	0	μm
k_{y_1}	10	MN/m	$v(t=0)$	0	μm
k_{x_2}	10	MN/m	$\theta_x(t=0)$	0	rad
k_{y_2}	10	MN/m	$\theta_y(t=0)$	0	rad
a	0.1769	m	$\dot{u}(t=0)$	0	$\mu m/s$
b	0.2175	m	$\dot{v}(t=0)$	0	$\mu m/s$
I_d	0.156502	kg m^2	$\dot{\theta}_x(t=0)$	0	s^{-1}
I_p	0.010468	kg m^2	$\dot{\theta}_y(t=0)$	0	s^{-1}
m	10.9904	kg			
c_1	500	Nm/s			
c_2	500	Nm/s			
ε	10	μm			

Table 3.2: Simulation parameters

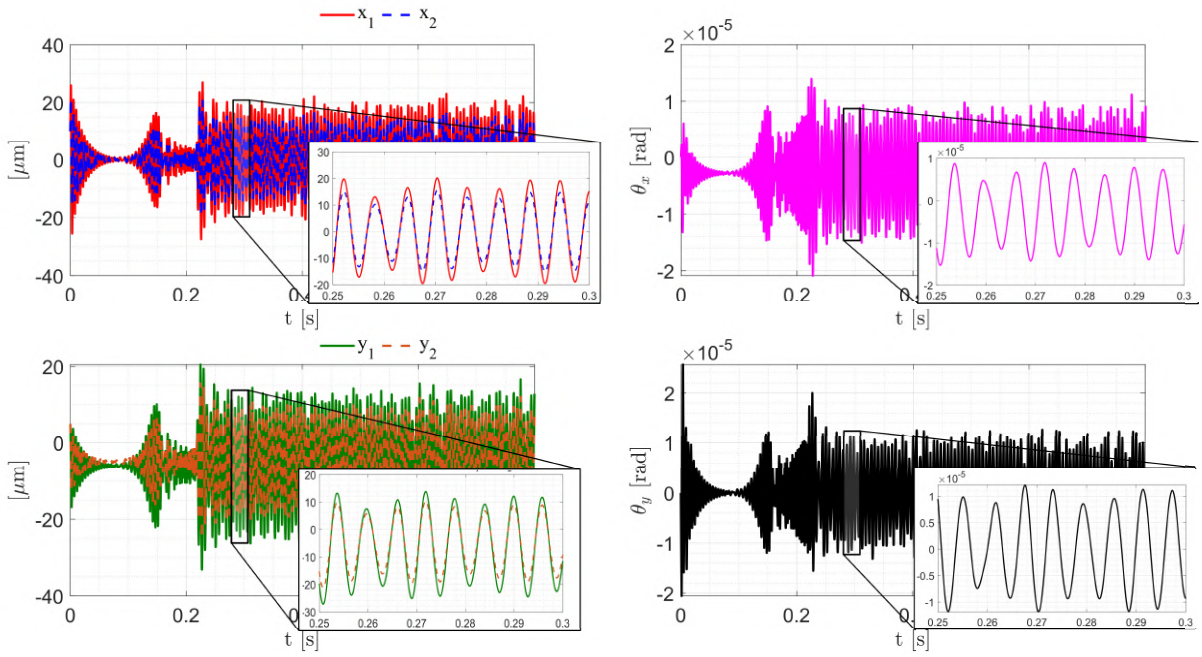

Figure 3.17: θ_x and θ_y displacements at bearings' locations and θ_x and θ_y tilting angles.

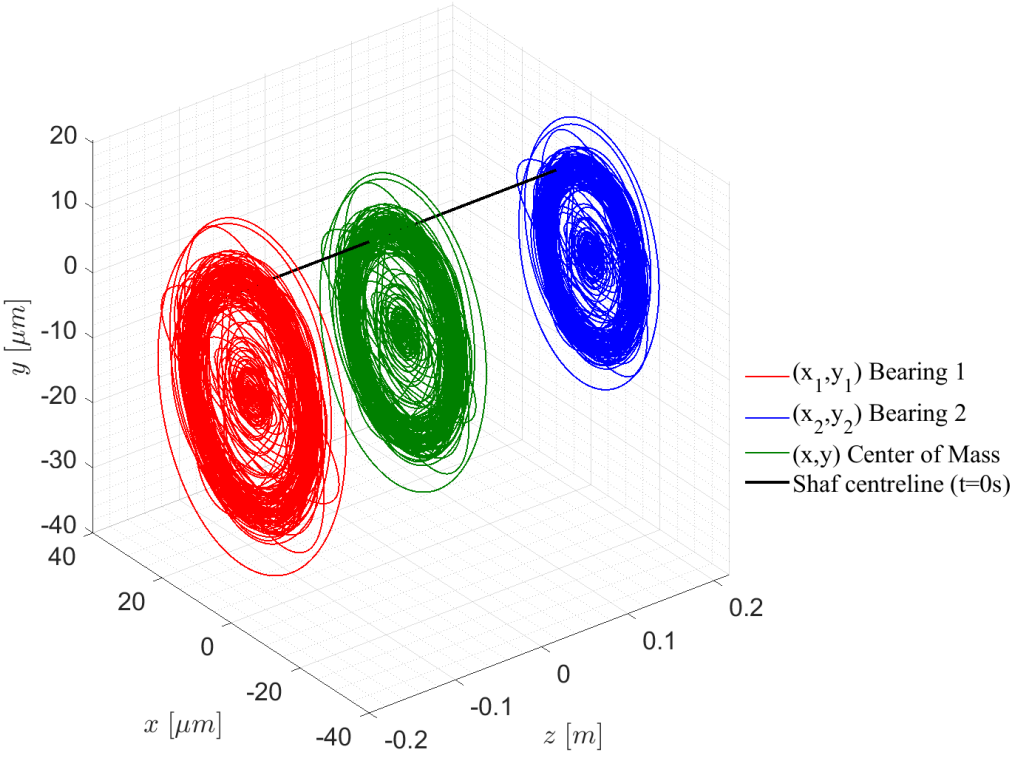

Figure 3.18: Position displacements at bearings' locations (3D plot)

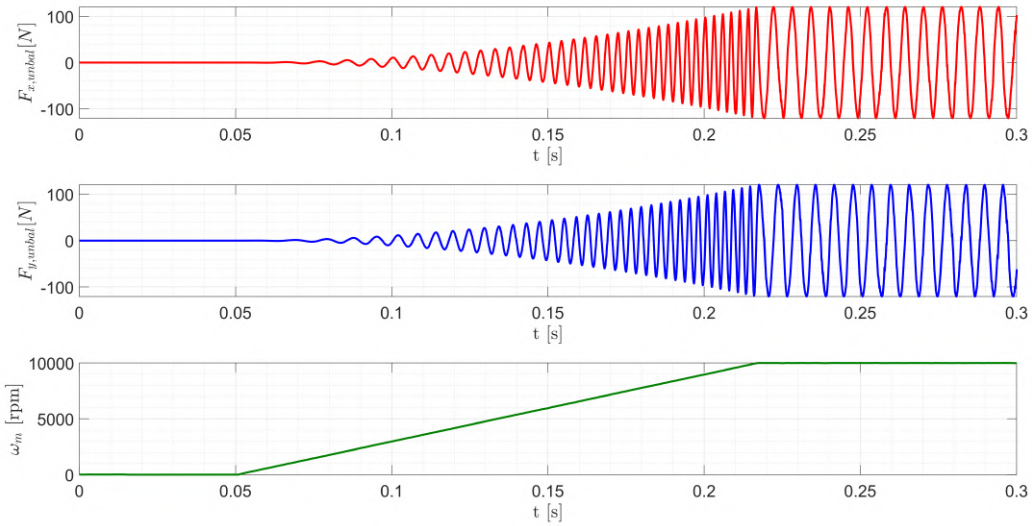

Figure 3.19: Out-of-Balance force components

3.5 Free and Forced Lateral Response of a Rotating Shaft

3.5.1 Natural frequencies

Natural frequency, also known as eigen frequency, is the frequency at which a mechanical system tends to oscillate in the absence of any driving force. The motion pattern of a system oscillating at its natural frequency is called the normal mode (if all parts of the system move sinusoidally with that same frequency). Natural frequencies and mode shapes are usually considered the most critical properties of virtually any system. In fact, excessive vibrations in any system lead to structural and functional issues. It is possible to determine the natural frequencies of a system analytically or by considering its free response and determine the frequencies of its oscillations. The reason for this is that the natural frequencies can match with a system's vibration frequencies leading to resonances. For example, if a time-varying force is applied to a system and a frequency equivalent to one of the natural frequencies is included in its time waveshape, this may result in immense amplitude vibrations which risk putting the system in jeopardy. This is why when designing a mechanical system it is important to calculate and ensure the natural frequencies of vibration are far enough from any possible excitation frequency that the system is likely to encounter during normal operation. For this reason, it is appropriate to plot a graph showing the variation (i.e., the absolute values) of natural frequencies with shaft speed. That graph is called *Natural frequency maps* and it can also illustrate the relationship between resonances and parameters other than rotational speed. It is usual to express the natural frequencies in Hz and the speed of rotation in rpm (revolutions per minute).
In the machine design, there are some parameters that directly affect the rotodynamic of the machine (bearing stiffness, shaft length, the mass of the rotor, the inertia of the rotor, etc). Bearing-support stiffness is a particularly relevant example of such variable parameters. Maps of critical speed allow obtaining rapidly an impression of how the uncertainty in one of the parameters affects the behavior of the machine. The most relevant concern is that a parameter cannot assume a value that causes one of the machine's critical speeds to occur at an undesirable part of the running range of speeds.
The natural frequencies obtained from the FFT free response of the rotor machine considered in this thesis are reported in figure 3.20 (the damping has been neglected in order to perform the FFT analysis).

For the considered mechanical system, the machine has a natural frequency of 215 Hz roughly. It has to be noticed that this system has only one natural frequency (this is mainly due to equal bearings at both sides of the shaft) but if the bearings are different, it is more likely that the system presents two or more natural frequencies.

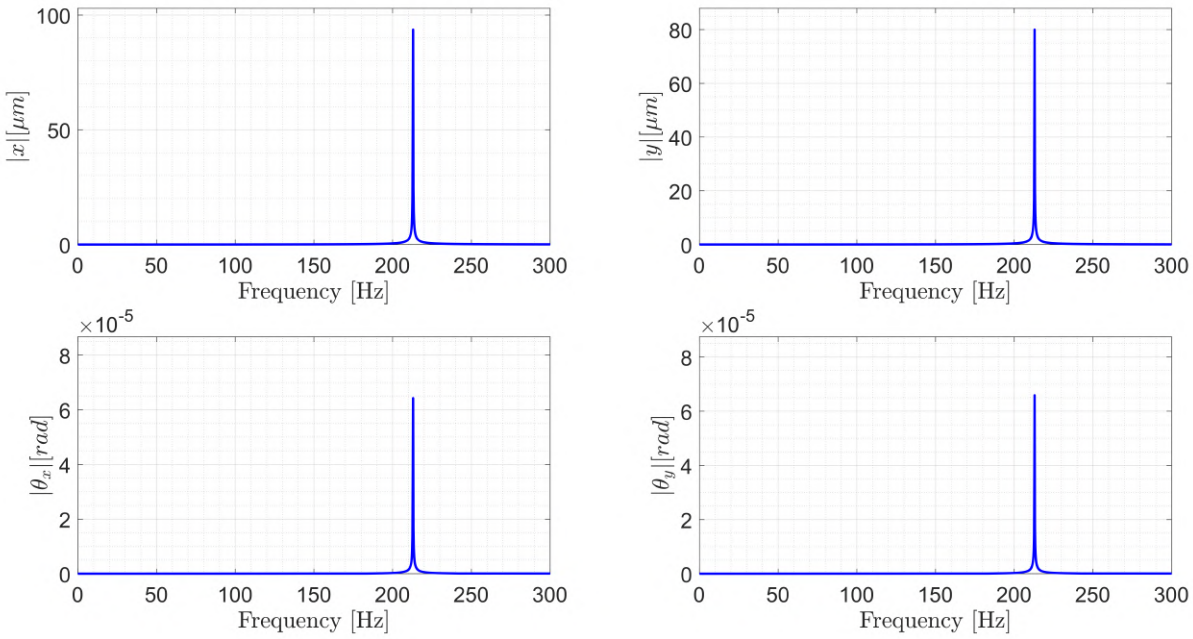

Figure 3.20: Natural frequencies

3.5.2 Critical speeds

In some cases, the rotor of a machine experiences exciting forces from external sources that have no direct connection with its own spin speed. It is occasionally found that fixed-frequency lateral forcing exists on an electrical machine that is modulated by a multiple of rotational speed because of some type of asymmetry on the rotor. Other forces acting on rotors include foundation forces that are transmitted to the rotor via the bearings; gravity forces on large horizontal rotors; and effects of rotor bow, misaligned couplings, and cracks. Some of these forces rotate at the rotor speed or multiples of it, others act in a fixed direction with excitation frequencies unrelated to rotor speed.
The response of a rotor-bearing system to various types of excitation can be large. The speeds at which such large responses occur are called *critical speeds* and locating them is of the utmost importance to designers. Simply stated, a critical speed is the rotational speed of a machine or shaft line at which the machine behaves poorly, and large vibrations or shaft whirls occur. If a machine is run continuously at a critical speed, then damage can occur very quickly. Often, this happens when an excitation frequency coincides with a resonance frequency of the machine. The maximum response criterion or the coincidence of excitation and resonance frequency may be used to estimate critical speeds for lightly damped, simple systems. From the natural frequencies results, a critical speed around 13000 rpm ($215Hz \cdot 60 \approx 13000rpm$) is expected.

3.5.3 Mode Shapes

In rotodynamic, mode shapes are a manifestation of eigenvectors which describe the relative displacement of two or more elements in a mechanical system as, in this case, the shaft displacement at the bearings locations. A mode shape is a pattern related to a particular natural frequency and represents the relative displacement of all parts of a structure for that particular mode. Mode shapes are strictly related to the system parameters (bearing stiffness, mass and inertia of the shaft, length of the shaft, etc.), to the speed of rotation, and to the forces applied to the shaft. For a rotating shaft, there are two main mode shapes as shown in 3.21:

- *Cylindrical mode shape*: the x and y shaft displacement oscillates with the same angle. The trajectory of the shaft during the motion describes a cylinder.
- *Conical mode shape*: the x and y shaft displacement oscillates with the same angle. The trajectory of the shaft during the motion describes a double cone.

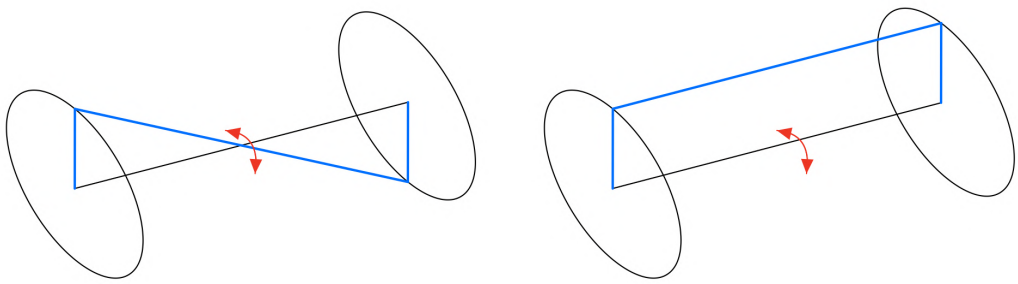

Figure 3.21: Conical (left) and cylindrical (right) mode shapes

Mode shapes simulation results

From simulation results, it has been proved that if the two isotropic bearings have the same stiffness, the mode shape is cylindrical. On the other hand, if the two bearings present significantly different stiffness (e.g., one stiffness is more than 5 times bigger than the other) the mode shape is conical. The simulation results are shown in fig. 3.22 where per Table 3.3.

As it is possible to see if the two bearings present different stiffness ($k_{x_1} = k_{y_1} = 10MN/m$ and $k_{x_2} = k_{y_2} = 80MN/m$) the mode shape is conical. In fact, from 3.22 it is possible to notice that x_1 has the opposite phase of x_2 and y_1 has the opposite phase of y_2. This doesn't happen when the two bearings are equal as shown in figure 3.17.

Mechanical parameters			Initial Conditions		
k_{x_1}	10	MN/m	$u(t=0)$	0	μm
k_{y_1}	10	MN/m	$v(t=0)$	0	μm
k_{x_2}	80	MN/m	$\theta_x(t=0)$	0	rad
k_{y_2}	80	MN/m	$\theta_y(t=0)$	0	rad
a	0.1769	m	$\dot{u}(t=0)$	0	$\mu m/s$
b	0.2175	m	$\dot{v}(t=0)$	0	$\mu m/s$
I_d	0.156502	kg m^2	$\dot{\theta}_x(t=0)$	0	s^{-1}
I_p	0.010468	kg m^2	$\dot{\theta}_y(t=0)$	0	s^{-1}
ε	10	μm			

Table 3.3: Simulation parameters

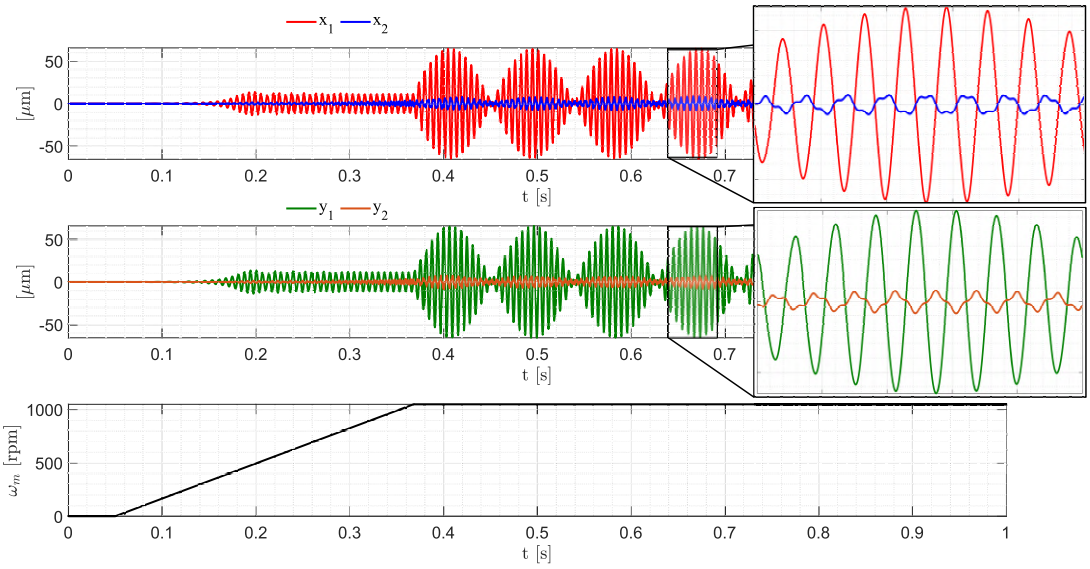

Figure 3.22: x and y displacement at bearings locations

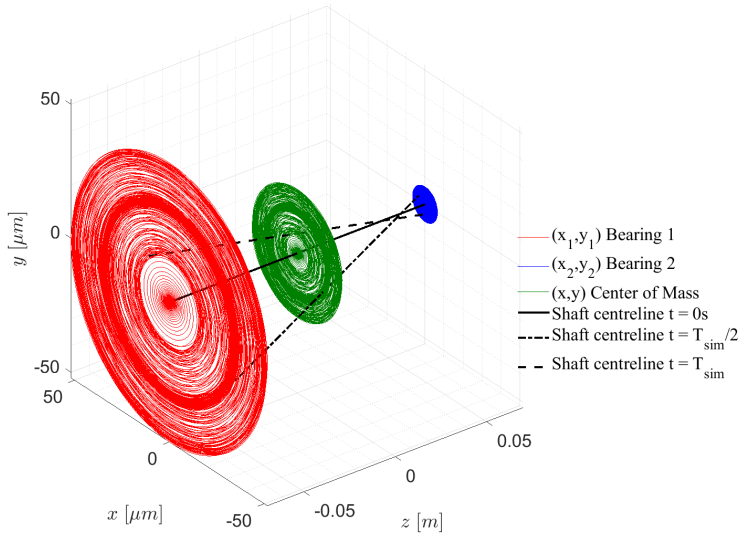

Figure 3.23: x and y displacement at bearings locations (3D plot)

In addition, with different bearings, the system has two natural frequencies as shown in fig. 3.24.

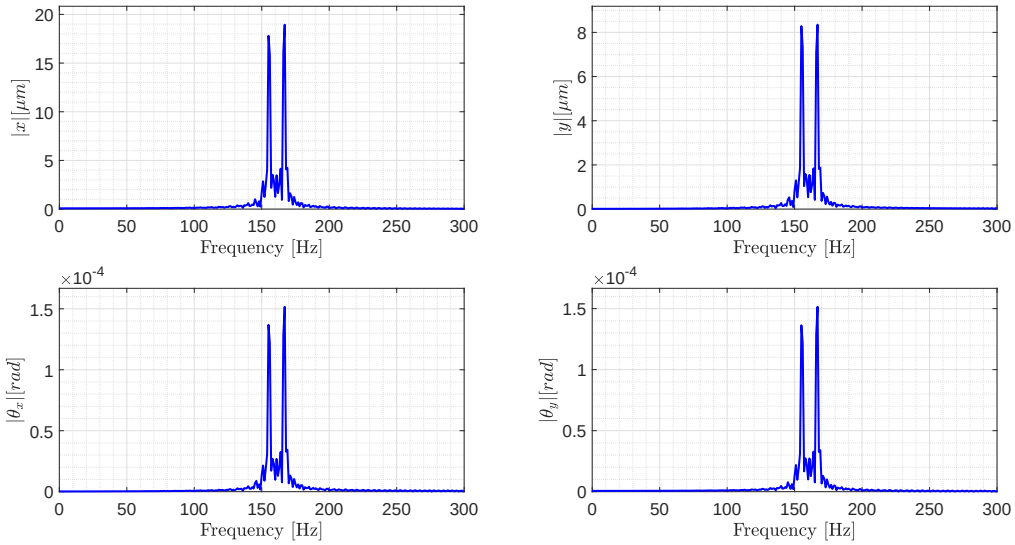

Figure 3.24: Natural frequencies (different bearings)

Chapter 4

Control Architecture

This Chapter deals with the radial force control implemented in this thesis in order to control the displacement at the bearing locations. The control system consists of three control loops: the current control loop, resulting from the wrench control set points, and the position and speed control loop. The implementation and the criticality of these two cascaded control loops are presented in this chapter.

4.1 Voltage modulation and converter architecture

The voltages are applied to the machine terminals by using a three-phase inverter for each three-phase subwinding (i.e., motor sector) as shown in figure 4.1. The three inverters share the same DC bus.

Thanks to the star connection of the motor winding in each sector, it is possible to control the phase currents of the motor with three conventional three-phase converters (each sector has a star connection galvanically isolated from the others).

In Simulink, the three inverters have been implemented in such a way that the user

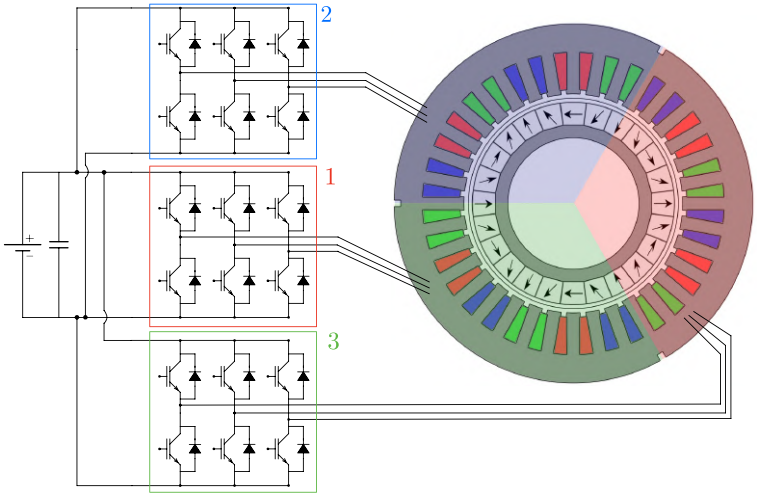

Figure 4.1: Converter Architecture

can select their representation with Simscape blocks (which represent the behavior of a real inverter with good accuracy) or with ideal voltage sources for each branch voltage (ideal inverter). In this way, it is possible to simulate the ideal and the real converter and see the effect it has on the control of the machine. The Simulink implementation is shown in fig. 4.2 and the set of parameters is listed in 4.1. In both real and Ideal inverters the PWM delay due to the modulation is simulated in the PWM modulation block.

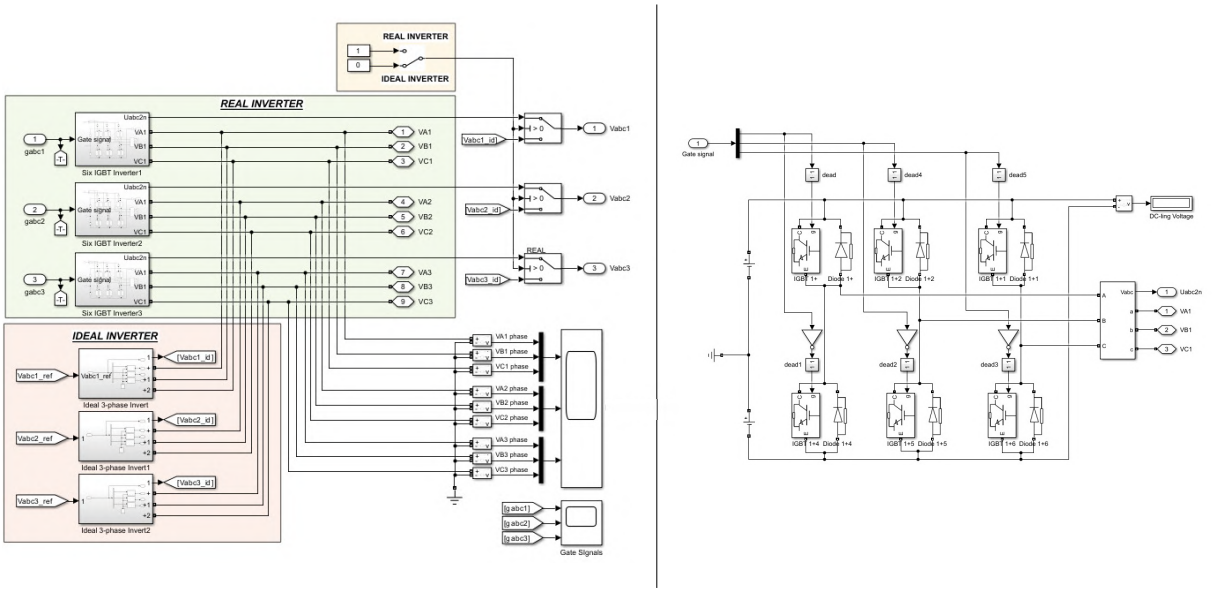

Figure 4.2: Ideal and real inverter implementation in Simulink (left) and one real inverter view block view (right).

REAL INVERTERS PARAMETERS	
Swithing frequency	$f_s = 10$ kHz
DC link Voltage	$V_{DC} = 700$ V
Death Time	$T_{death} = 1.5\ \mu m$
Forward ON Voltage (IGBT)	$V_{f,IGBT} = 0.9\ V$
ON Resistance (IGBT)	$R_{ON,IGBT} = 00.018\ \Omega$
Forward ON Voltage (Diode)	$V_{f,D} = 0.8\ V$

Table 4.1: Real Inverter Parameters

4.2 Current control

The control of the currents is performed by using a classic PWM modulation which controls each three-phase inverter. The current-voltage references are determined by a PI controller for the d and q axes as usually done for a classic FOC (Field Orientation Control) used for the torque control. The current references are obtained from the wrench reference by using the Pseudo Inverse Matrix (PIM) approach as described in the 4.3.

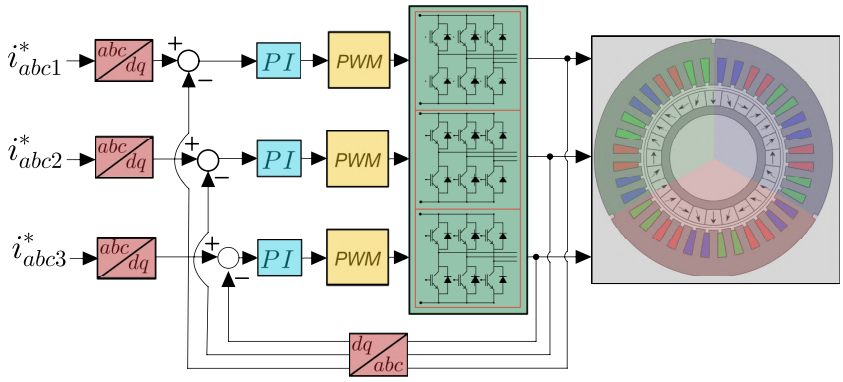

Figure 4.3: Current Control

The voltage references are obtained with a PI controller for each sector as the machine was composed of three three-phase independent machines sharing the same shaft. It must be noticed that in the current control scheme, the mutual coupling between the sectors is neglected and each three-phase sector is controlled independently from the others (in the machine model the mutual coupling between the sectors is considered with the inductance matrix but not in the wrench mapping). However, there are control strategies in the literature that also take into account the mutual coupling between sectors. For example, a control strategy based on the space vector decomposition approach that takes into account the inductive mutual coupling between sectors has been proposed in [46].

4.3 Wrench Control

The following section presents the technique for radial force and torque control based on the pseudo-inverse matrix approach applied to the MSPM machine. The SPM rotor layout and the distribution of the three-phase windings (sectors) enable, with a good approximation, the achievement of the independent control of the x and y force and torque contributions attributed to each sector. Based on the superposition principle, these contributions are then added up to track the desired force and torque control.

4.3.1 Matrix K Inversion

In order to control the sectored multi-three-phase bearingless SPM motor, the current references must be calculated to produce the desired torque and radial forces. The relation between the wrench and the currents is expressed through the matrix as shown in eq. (4.1) here reported:

$$\overline{W}_E = \mathbf{K_{abc}}(\theta_e)\bar{i}_{abc} \tag{4.1}$$

The matrix K is not a square matrix so it is not possible to calculate the inverse matrix to determine the currents that give the desired force. For this reason, the pseudo-inverse

matrix (or Penrose inverse matrix) is calculated to determine the current references. Furthermore, the constraint (4.2) due to the star connection must be included to impose the sum of the currents in each sector as zero:

$$\mathbf{S}\bar{i}_{abc} = 0 \tag{4.2}$$

Where S is the matrix that imposes the zero-sum in each machine sector:

$$\mathbf{S} = \begin{bmatrix} 1 & 1 & 1 & 0 & 0 & 0 & 0 & 0 & 0 \\ 0 & 0 & 0 & 1 & 1 & 1 & 0 & 0 & 0 \\ 0 & 0 & 0 & 0 & 0 & 0 & 1 & 1 & 1 \end{bmatrix} \tag{4.3}$$

In this way the system of equations to be solved is:

$$\begin{aligned} \overline{W}_E &= \mathbf{K_{abc}}\bar{i}_{abc} \\ \mathbf{S}\bar{i}_{abc} &= 0 \end{aligned} \tag{4.4}$$

which can be rewritten as:

$$\overline{W}_E = \mathbf{K}_e\bar{i}_{abc} \tag{4.5}$$

with:

- $\mathbf{K}_e = [\mathbf{K}_{abc},\ \mathbf{S}]^T$
- $\overline{W}_E = [F_x,\ F_y,\ T,\ 0,\ 0,\ 0]^T$

The resulting $\mathbf{K_e}$ matrix, written keeping the dependency from θ_e implicit is:

$$\mathbf{K_e} = \begin{bmatrix} K_{F_x,a_1} & K_{F_x,b_1} & K_{F_x,c_1} & K_{F_x,a_2} & K_{F_x,b_2} & K_{F_x,c_2} & K_{F_x,a_3} & K_{F_x,b_3} & K_{F_x,c_3} \\ K_{F_y,a_1} & K_{F_y,b_1} & K_{F_y,c_1} & K_{F_y,a_2} & K_{F_y,b_2} & K_{F_y,c_2} & K_{F_y,a_3} & K_{F_y,b_3} & K_{F_y,c_3} \\ K_{T,a_1} & K_{T,b_1} & K_{T,c_1} & K_{T,a_2} & K_{T,b_2} & K_{T,c_2} & K_{T,a_3} & K_{T,b_3} & K_{T,c_3} \\ 1 & 1 & 1 & 0 & 0 & 0 & 0 & 0 & 0 \\ 0 & 0 & 0 & 1 & 1 & 1 & 0 & 0 & 0 \\ 0 & 0 & 0 & 0 & 0 & 0 & 1 & 1 & 1 \end{bmatrix} \tag{4.6}$$

In this way, for each rotor position, it is possible to calculate the pseudoinverse and the current references:

$$\bar{i}^*_{abc} = \mathbf{K}_{e,psi}W^*_E \tag{4.7}$$

Where the pseudo inverse matrix $\mathbf{K}_{e,psi}$ is defined as it follows:

$$\mathbf{K}_{e,psi} = K_e^T[K_eK_e^T]^{-1} \tag{4.8}$$

In Matlab, the command to calculate the Pseudo-inverse matrix is *pinv()*.

As we can see from the calculation of the current references, the last 3 columns of the matrix $\mathbf{K}_{e,psi}$ are unnecessary and they can be deleted (all the coefficients of these columns are multiplied by zero since the last three elements of $W^*_E = [F_x,\ F_y,\ T,\ 0,\ 0,\ 0]$

are zeros). So the matrix $\mathbf{K}_{e,psi}$ (9×6 matrix), by eliminating the last three columns becomes K_{psi} (9×6 matrix):

$$\mathbf{K}_{e,psi} \quad \rightarrow \quad \textit{eliminating columns } 4,5,6 \quad \rightarrow \quad \mathbf{K}_{psi} \tag{4.9}$$

$$K_{psi} = \begin{bmatrix} K'_{psi,F_xA_1}(\theta) & K'_{psi,F_yA_1}(\theta) & K'_{psi,TA_1}(\theta) \\ K'_{psi,F_xB_1}(\theta) & K'_{psi,F_yB_1}(\theta) & K'_{psi,TB_1}(\theta) \\ K'_{psi,F_xC_1}(\theta) & K'_{psi,F_yC_1}(\theta) & K'_{psi,TC_1}(\theta) \\ K'_{psi,F_xA_2}(\theta) & K'_{psi,F_yA_2}(\theta) & K'_{psi,TA_2}(\theta) \\ K'_{psi,F_xB_2}(\theta) & K'_{psi,F_yB_2}(\theta) & K'_{psi,TB_2}(\theta) \\ K'_{psi,F_xC_2}(\theta) & K'_{psi,F_yC_2}(\theta) & K'_{psi,TC_2}(\theta) \\ K'_{psi,F_xA_3}(\theta) & K'_{psi,F_yA_3}(\theta) & K'_{psi,TA_3}(\theta) \\ K'_{psi,F_xB_3}(\theta) & K'_{psi,F_yB_3}(\theta) & K'_{psi,TB_3}(\theta) \\ K'_{psi,F_xC_3}(\theta) & K'_{psi,F_yC_3}(\theta) & K'_{psi,TC_3}(\theta) \end{bmatrix}$$

SECTOR 1 — SECTOR 2 — SECTOR 3

F_x F_y T

Figure 4.4: Matrix $\mathbf{K}_{psi}$

The results of the matrix $\mathbf{K}_{psi}$ coefficients calculation for each rotor position are shown in fig. 4.5 and their FFT analysis in fig. 4.6.

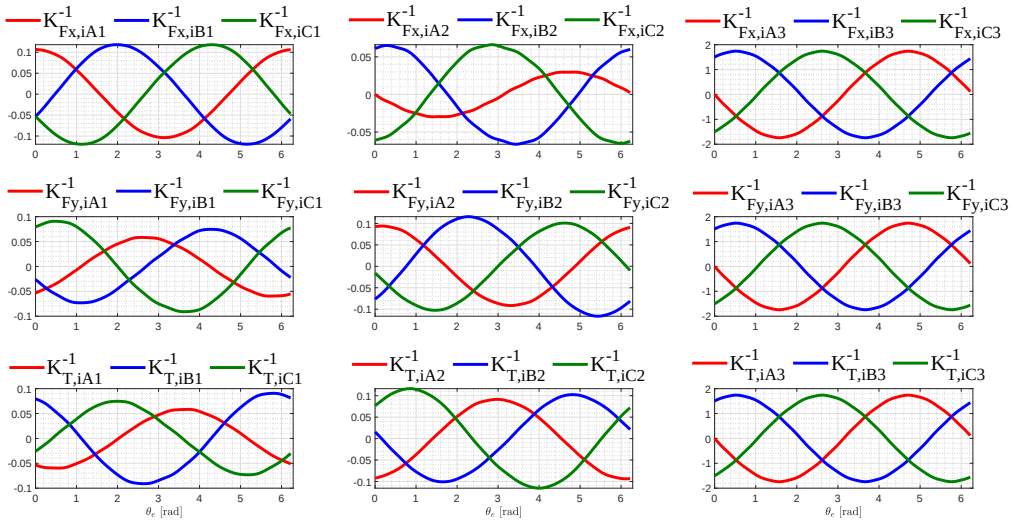

Figure 4.5: Matrix $\mathbf{K}_{psi}$ coefficients versus rotor position (all the coefficients are expressed in A/N for the coefficients of the forces and in A/Nm for the coefficients of the torque).

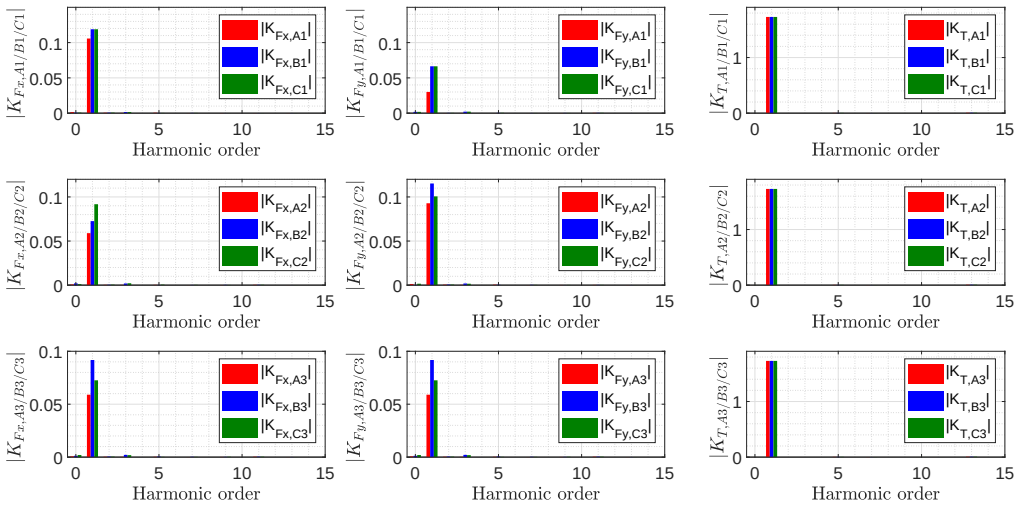

Figure 4.6: Matrix $\mathbf{K}_{psi}$ coefficients FFT Amplitude (all the coefficients are expressed in A/N for the coefficients of the forces and in A/Nm for the coefficients of the torque).

Numerical Implementation

The pseudoinverse matrix coefficients must be known for each rotor position in order to determine the current references starting from the wrench references. For this reason, the coefficients can be calculated offline and then stored in the DSP by using a look-up table, avoiding computing the pseudoinverse in real time. Differently, it is possible to calculate the pseudoinverse matrix coefficients for each rotor position starting from the FFT analysis computed offline and consequently calculate the $\mathbf{K}_{psi}$ coefficient for the current rotor position by using the FFT:

$$K_{psi,ij}(\theta_e) = \sum_{\rho=0}^{\rho_{max}} |\overline{K}_{psi,ij,\rho}| \; cos(\rho\theta_e + \phi_{psi,ij,\rho})| \tag{4.10}$$

where:

- ρ is the harmonic order;
- $\overline{K}_{psi,ij,\rho}$ is ρ^{th}-harmonic coefficient of the FFT serial development of ij^{th} element of the matrix $\mathbf{K}_{psi}$;
- $\phi_{psi,ij,\rho} = \angle\, \overline{K}_{psi,ij,\rho}$ is the angle of the ρ-th harmonic of the FFT series complex coefficient $\overline{K}_{psi,ij}$;

In the Simulink model, the FFT approach has been used. To reduce the computational load and make the control algorithm faster, it is possible to calculate the pseudo-inverse matrix by using only the 1^{st} harmonic ($\rho_{max} = 1$). This is allowed by the Halbach array magnets layout that has been optimized specifically for this kind of application and that

produces really sinusoidal matrix $\mathbf{K}_{abc}$ coefficients. Differently, in order to create the motor model (the Simulink model that allows, starting from the current, to calculate the wrench) all the harmonics of the matrix $\mathbf{K}_{abc}$ must be considered as shown in the chapter 2.2.4.

On the Pseudo-Inverse Matrix

In mathematics, and in particular linear algebra, the Moore–Penrose inverse $\mathbf{A}^+$ of a matrix $\mathbf{A}$ is the most widely known generalization of the inverse matrix. It was independently described by E. H. Moore in 1920, Arne Bjerhammar in 1951, and Roger Penrose in 1955. When referring to a matrix, the term pseudoinverse, without further specification, is often used to indicate the Moore–Penrose inverse. The term "generalized inverse" is sometimes used as a synonym for pseudoinverse. A common use of the pseudoinverse is to compute a "best fit" (least squares) solution to a system of linear equations that lacks a solution. Another use is to find the minimum (Euclidean) norm solution to a system of linear equations with multiple solutions. The pseudoinverse facilitates the statement and proof of results in linear algebra. The pseudoinverse is defined and unique for all matrices whose entries are real or complex numbers.
When $\mathbf{A}$ has linearly independent rows (matrix $\mathbf{A}^T$ is invertible) $\mathbf{A}^+$ can be computed as a normal inverse:

$$\mathbf{A}^+ = \mathbf{A}^T(\mathbf{A}\mathbf{A}^T)^{-1} \tag{4.11}$$

This is a normal inverse matrix so $\mathbf{A}\mathbf{A}^+ = I$.
The pseudoinverse provides a least squares solution to a system of linear equations. For $\mathbf{A} \in \mathbb{K}^{(m\times n)}$ (with $\mathbb{K}$ denotes one of the fields of real or complex numbers, denoted $\mathbb{R}$, $\mathbb{C}$ respectively), given a system of linear equations:

$$\mathbf{A}\bar{x} - \bar{B} = 0 \tag{4.12}$$

In general, a vector $\bar{x}$ that solves the system may not exist, or if one does exist, it may not be unique. The pseudoinverse solves the "least-squares" problem as follows:

$$\forall\ \bar{x} \in \mathbb{K}^{(m\times n)}, \quad ||\mathbf{A}\bar{x} - \bar{B}||_F \geq ||\mathbf{A}\bar{z} - \bar{B}||_F \tag{4.13}$$

with $||\cdot||_F$ the Frobenius norm and $\bar{B} \in \mathbb{K}^{m\times 1}$, and:

$$\bar{z} = \mathbf{A}^+\bar{B} \tag{4.14}$$

where $\bar{z}$ is the "least-squares" problem solution.

Demostration
As already mentioned, the pseudoinverse provides a least squares solution to a system of

linear equations. The least-square condition is:

$$\begin{cases} min \sum_{i=1}^{M} x_i^2 \\ \mathbf{A}\bar{x} - \bar{B} = 0 \end{cases} \tag{4.15}$$

The sum of the squares can be expressed as:

$$\sum_{i=1}^{M} x_i^2 = \bar{x}^T \bar{x} \tag{4.16}$$

Considering the Lagrange function, defined as:

$$\mathcal{L}(x) = \bar{x}^T \bar{x} - \bar{\lambda}^T \left(\mathbf{A}\bar{x} - \bar{B} \right) = 0 \tag{4.17}$$

The minimum of the Lagrange function (i.e. the minimum of $\bar{x}^T \bar{x}$ that satisfies $\mathbf{A}\bar{x} - \bar{B}$ is:

$$\frac{\partial \mathcal{L}(x)}{\partial x_i} = 0 \ \ \forall x_i \quad \rightarrow \quad \frac{\partial \mathcal{L}(x)}{\partial x_i} = \frac{\partial \left[\bar{x}^T \bar{x} + \bar{\lambda}^T \left(\mathbf{A}\bar{x} - \bar{B} \right) \right]}{\partial x_i} \ \ \forall i = 1, 2, 3... \tag{4.18}$$

Considering that $\bar{x}^T \bar{x} = \sum_{i=1}^{M} x_i^2$ and:

$$\bar{\lambda}^T \left(\mathbf{A}\bar{x} - \bar{B} \right) = [\lambda_1, ..., \lambda_i, ..., \lambda_M] \left(\begin{bmatrix} A_{1,1} & ... & A_{1,i} & ... & A_{1,M} \\ ... & ... & ... & ... & ... \\ ... & ... & A_{i,i} & ... & ... \\ ... & ... & ... & ... & ... \\ A_{M,1} & ... & A_{M,i} & ... & A_{M,M} \end{bmatrix} \begin{bmatrix} x_1 \\ ... \\ x_i \\ ... \\ x_M \end{bmatrix} + \begin{bmatrix} B_1 \\ ... \\ B_i \\ ... \\ B_M \end{bmatrix} \right) \tag{4.19}$$

The optimal solution $\bar{x} = [x_1, x_2, \ldots, x_M]^T$ is the one that satisfies:

$$\frac{\partial \left[\bar{x}^T \bar{x} + \bar{\lambda}^T \left(\mathbf{A}\bar{x} - \bar{B} \right) \right]}{\partial x_i} = 2x_i - \bar{\lambda}^T A(:, i) = 0 \quad \rightarrow \quad \bar{x} = \frac{1}{2} \mathbf{A}^T \bar{\lambda} \tag{4.20}$$

Considering the expression (4.20) of $\bar{x}$, and inserting it in (4.12):

$$\frac{1}{2} \mathbf{A}\mathbf{A}^T \bar{\lambda} - \bar{B} = 0 \tag{4.21}$$

From this:

$$\bar{\lambda} = 2 \left(\mathbf{A}\mathbf{A}^T \right)^{-1} \bar{B} \tag{4.22}$$

And the optimal solution of the system from eq. (4.20) becomes:

$$\bar{x} = \frac{1}{2}\mathbf{A}^T\bar{\lambda} = \frac{1}{2}\mathbf{A}^T\left[2\left(\mathbf{A}\mathbf{A}^T\right)^{-1}\bar{B}\right] = \mathbf{A}^T\left(\mathbf{A}\mathbf{A}^T\right)^{-1}\bar{B} \tag{4.23}$$

where:

$$\mathbf{A}^+ = \mathbf{A}^T\left(\mathbf{A}\mathbf{A}^T\right)^{-1}\bar{B}. \tag{4.24}$$

$\mathbf{A}^+$ is the pseudoinverse matrix of A. So the least squares solution of the system is:

$$\bar{x} = \mathbf{A}^+\bar{B} \tag{4.25}$$

In the case of the motor and of the wrench calculation, among the infinite solutions to the problem, the one that minimizes the stator copper losses is considered (i.e., which minimizes the square values of the inputs, i.e. the phase currents). The problem is described as:

$$\begin{aligned} \bar{x} &= \bar{i_{abc}} \\ \mathbf{A} &= \mathbf{K_{abc}} \\ \bar{B} = \bar{W_E} &= \begin{bmatrix} F_x \\ F_y \\ T \end{bmatrix} \end{aligned} \tag{4.26}$$

And the optimal solution (phase currents) of the system to track a reference wrench $\bar{W_E}$ is:

$$\bar{i}_{abc} = \mathbf{K_{psi}}\bar{W}_E \tag{4.27}$$

with $\mathbf{K_{psi}}$ the reduced pseudoinverse matrix as shown in Fig. 4.4. Thus, the pseudo-inverse matrix approach allows the minimization of the sum of the square of the stator currents and, as consequence, the Joule losses.

4.4 Speed control

The speed control is performed by using a classical approach based on a PI controller: starting from the speed reference, the speed error is calculated, and from this the torque reference. The torque reference is used for the calculation of the average value of the q-axis current of the three sectors. This calculation is directly obtained thanks to the pseudoinverse matrix.

4.5 Position Control

The speed control is performed by using a PID controller for the x-position and a PID controller for the y-position: starting from the position references (both set to zero $x^* = 0$, $y^* = 0$), the position error and, from this, the force components (F_x^* and F_y^*) references are calculated. The force components references are used for the calculation of current references for each sector thanks to the pseudoinverse matrix. The position feedback can be chosen as:

- position feedback x_1 and y_1 measured at the bearing 1 location;
- position feedback x_2 and y_2 measured at the bearing 2 location;
- position feedback calculated as the mean of the position $x = \dfrac{x_1 + x_2}{2}$ and $y = \dfrac{y_1 + y_2}{2}$ measured at both bearings locations;

The complete control diagram is shown in fig. 4.7.

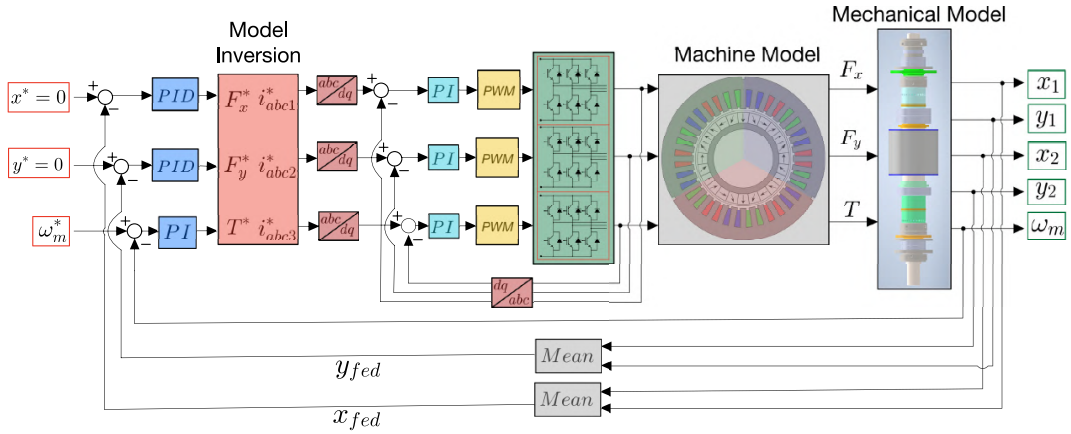

Figure 4.7: Complete control diagram and model overview

4.5.1 On the PID controllers

In order to understand radial force control and why a PID controller is required, it is useful to understand the general principles behind a simple mono-dimensional levitation system analyzed in [47]. Simplifying, electromagnetic force production can be easily understood based on the principle of attraction between a magnet (or electromagnet) on a mover.

The attractive magnetic force F_m must compensate for the weight of the mover $w = mg$:

$$F_m \approx k_m h_0^2 \tag{4.28}$$

Where k_m is proportional to the area S of the airgap and h_0 is the magnetic field at

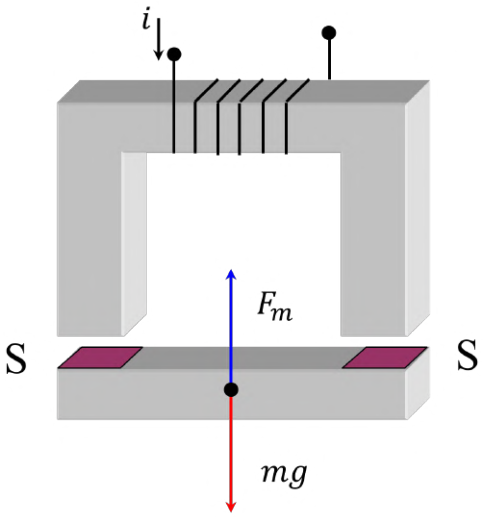

Figure 4.8: Attraction between an electromagnet on a mover

the airgap. Assuming negligible damping of the air, the dynamic equation for the mover is:

$$mg - k_m h_0^2 = m\frac{d^2x}{dt^2} \tag{4.29}$$

And in order to describe the system, the circulation of the field h must be considered:

$$Ni = L_f h_f + 2xh_0 \approx 2xh_0 \tag{4.30}$$

where L_f and h_f are the length of the circulation line and the magnetic field in the iron respectively.
Assuming that for each position x_0 there is a current i_0 that keeps the system in its equilibrium point, by producing a force F_{m0} (and a corresponding field H_0 in the airgap), the stability of the system can be analyzed for an infinitesimal perturbation:

$$h_0 = H_0 + \Delta h_0 \quad x = x_0 + \Delta x_0 \quad i = i_0 + \Delta i \tag{4.31}$$

With the introduction of the infinitesimal variation (4.31), the equations (4.30) and (4.29), neglecting the second order infinitesimal variations, result:

$$\begin{aligned} mg - k_m h_0^2 - 2k_m \Delta h_0 H_0 - 2k_m \Delta h_0^2 = m\frac{d^2x_0}{dt^2} + m\frac{d^2\Delta x}{dt^2} \quad &\rightarrow \quad -2k_m \Delta h_0 H_0 = m\frac{d^2\Delta x}{dt^2} \\ Ni_0 + N\Delta_i = 2x_0 H_0 + 2x_0 \Delta h_0 + 2\Delta x_0 H_0 + \Delta x_0 \Delta h_0 \quad &\rightarrow \quad N\Delta_i = 2x_0 \Delta h_0 + 2\Delta x_0 H_0 \end{aligned} \tag{4.32}$$

Obtaining Δh_0 from the second of (4.32) and inserting in the first one:

$$\frac{k_m H_0 N}{x_0}\Delta i = \frac{2k_m H_0^2}{x_0}\Delta x - m\frac{d^2\Delta x}{dt^2} \quad \rightarrow \quad A\Delta i = B\Delta x - C\frac{d^2\Delta x}{dt^2} \tag{4.33}$$

In the Laplace Domain:

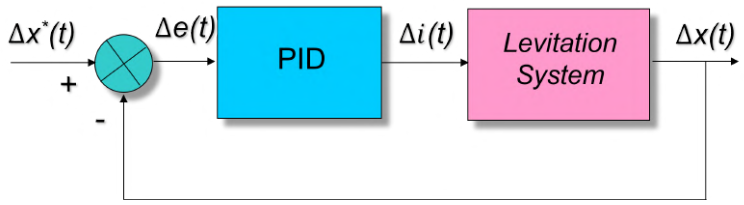

Figure 4.9: Current Control loop based on PID controller [47]

$$A\Delta i = (B - Cs^2)\Delta x \quad \rightarrow \quad s = \pm\sqrt{\frac{B}{C}} = \sqrt{\frac{2k_m H_0^2}{x_0}} \tag{4.34}$$

From eq. (4.34) the system presents two conjugate poles. This means that the levitation system is unstable. If the current i in the coil is constant and the mover goes up, the attraction force increases and vice-versa. For this reason, a closed-loop control that determines the current necessary to control the position is required. A suitable controller can be a conventional PID regulator:

The current reference is calculated by the PID controller from the position error as:

$$\Delta i(t) = K_p\Delta e(t) + K_i \int \Delta e(t)dt + K_d\frac{d\Delta e(t)}{dt} \quad \rightarrow \quad \mathcal{L} \quad \rightarrow \quad \Delta I = K_p\Delta E + \frac{K_i}{s}\Delta E + K_d s\Delta E \tag{4.35}$$

Considering equations (4.34), (4.35) and $\Delta E = \Delta X^* - \Delta X$, the total transfer function of the system is:

$$\Delta E = \frac{Bs - Cs^3}{AK_i + (AK_p + B)s + AK_d s^2 - Cs^3}\Delta X^* \tag{4.36}$$

The characteristic polynomial corresponding to the transfer function is:

$$s^3 - \frac{AK_d}{C}s^2 - \frac{(AK_p + B)}{C}s - \frac{AK_i}{C} = 0 \tag{4.37}$$

And in according to the Routh Criteria, following the procedure presented in [47], the result of the stability condition is:

$$\begin{aligned} &K_d < 0 \\ &K_p < -\frac{B}{A} - \frac{C}{A}\frac{K_i}{K_d} \\ &K_i < 0 \end{aligned} \tag{4.38}$$

Considering now the general expression of a third-order characteristic polynomial:

$$(s\text{-}s_1)(s - s_2)(s - s_3) = 0 \quad \rightarrow \quad s^3 + (-s_1 - s_2 - s_3)s^2 + s(s_1s_2 + s_es_3 + s_3s_1)s - s_1s_2s_3 = 0 \tag{4.39}$$

From the comparison of the second-order term's coefficient results in eq. (4.37) and

(4.39), it results:

$$-s_1 - s_2 - s_3 = -\frac{AK_d}{C} \quad \rightarrow \quad K_d = -\frac{C}{A}(s_1 + s_2 + s_3) \tag{4.40}$$

In order to have 3 poles with a negative real part (stability condition), it's necessary to have the derivative term in the controller, so a PID controller is mandatory for this kind of application. In fact, if $K_d = 0$ (the controller would be a PI instead of a PID) means that $s_1 + s_2 + s_3$ is equal to zero, so one of the poles has a necessarily positive real part.

Chapter 5

System Simulations and Results

In this chapter, the simulation results are presented and analyzed. First, a simulation with only the torque control is presented and the currents, back-EMFs, torque, and shaft displacement are analyzed. Then, force control is introduced. First, a constant force reference is set and the currents, back-EMFs, torque, and shaft displacements are analyzed. After that, the position control for the vibration suppression is activated and two cases are considered: equal bearings and different bearings at the shaft's ends. The type of bearings determines the mode shape of the dynamic of the rotor and the consequence performance of the control. Finally, the performance of the control, in the case of equal bearings, for different rotational speeds is presented.

5.1 Simulink Complete System Model

Fig. 5.1 shows the complete Simulink model used to simulate the system.

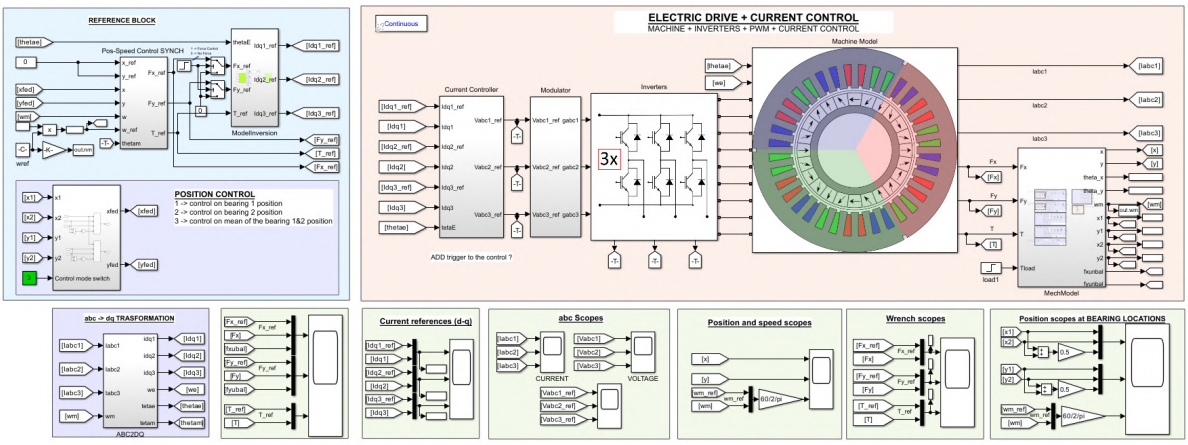

Figure 5.1: Complete Simulink model

5.2 Speed Control Simulation (Equal Bearings)

In this section, the speed control is presented: a constant speed reference is set and the reference torque is calculated by using the pseudo-inverse matrix approach. Subsequently, the currents and back-emf waveforms are shown. The parameters set to carry out this simulation are in 5.1.

Mechanical parameters			**Initial Conditions**		
k_{x_1}	10	MN/m	$u(t=0)$	0	μm
k_{y_1}	10	MN/m	$v(t=0)$	0	μm
k_{x_2}	10	MN/m	$\theta_x(t=0)$	0	rad
k_{y_2}	10	MN/m	$\theta_y(t=0)$	0	rad
a	0.1769	m	$\dot{u}(t=0)$	0	$\mu m/s$
b	0.2175	m	$\dot{v}(t=0)$	0	$\mu m/s$
I_d	0.156502	kg m^2	$\dot{\theta}_x(t=0)$	0	s^{-1}
I_p	0.010468	kg m^2	$\dot{\theta}_y(t=0)$	0	s^{-1}
m	10.9904	kg			
c_1	500	Nm/s			
c_2	500	Nm/s			
ε	10	μm			

Table 5.1: Simulation parameters

5.2.1 Wrench results

A speed reference of $\omega_m^* = 10000 rpm$ is set at $t = 0.05 s$ and the wrench and the speed scopes are shown in fig. 5.2.

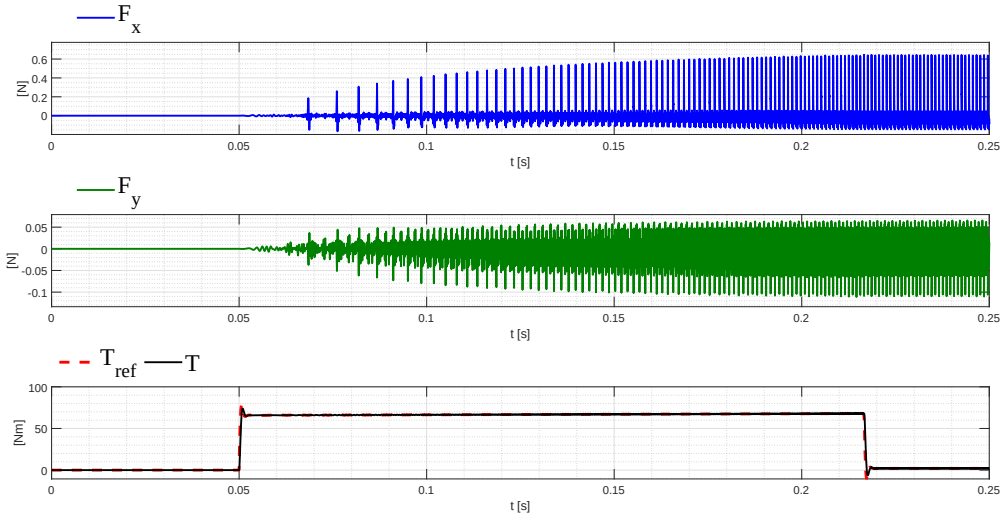

Figure 5.2: Wrench results (constant speed, no force control)

Even if the force reference is set to zero, there is a small force ripple attributed to the not perfect tracking performed by the current regulator or due to the numerical error in the Simulink model or in the FEA wrench mapping. Anyway, this force ripple is negligible compared to the rated force of the machine (2000 N).

5.2.2 Current and Back-emf waveforms

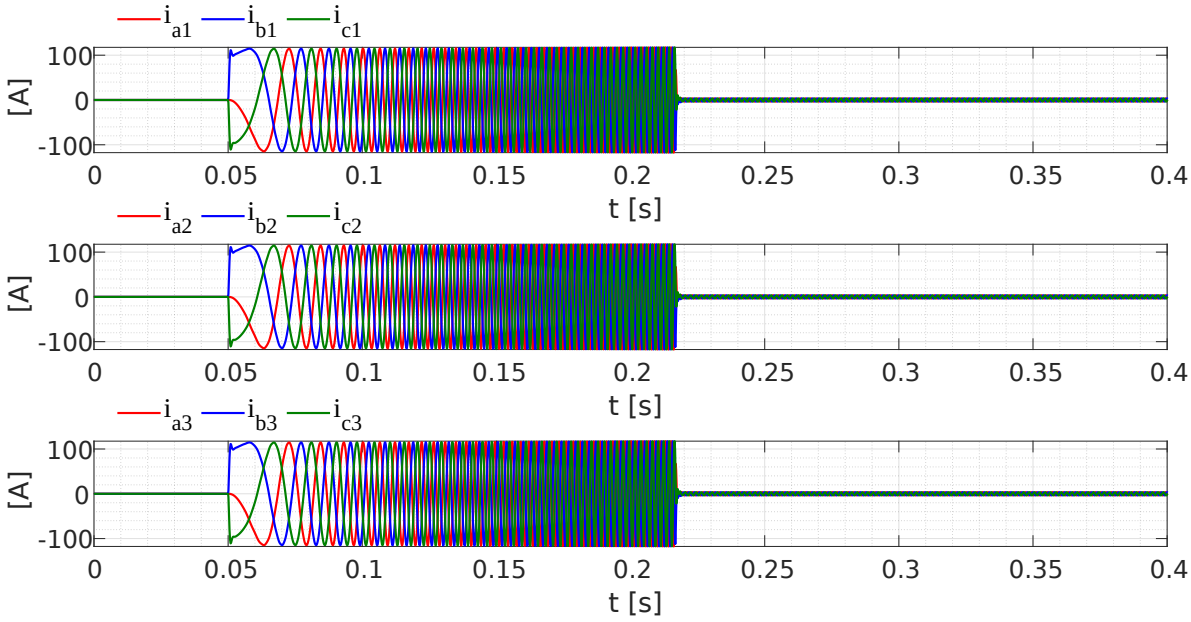

Figure 5.3: Currents waveforms (constant speed, no force control)

For torque control only, in each sector, the currents are three symmetrical sinusoidal waveforms shifted by 120 electrical degrees each.

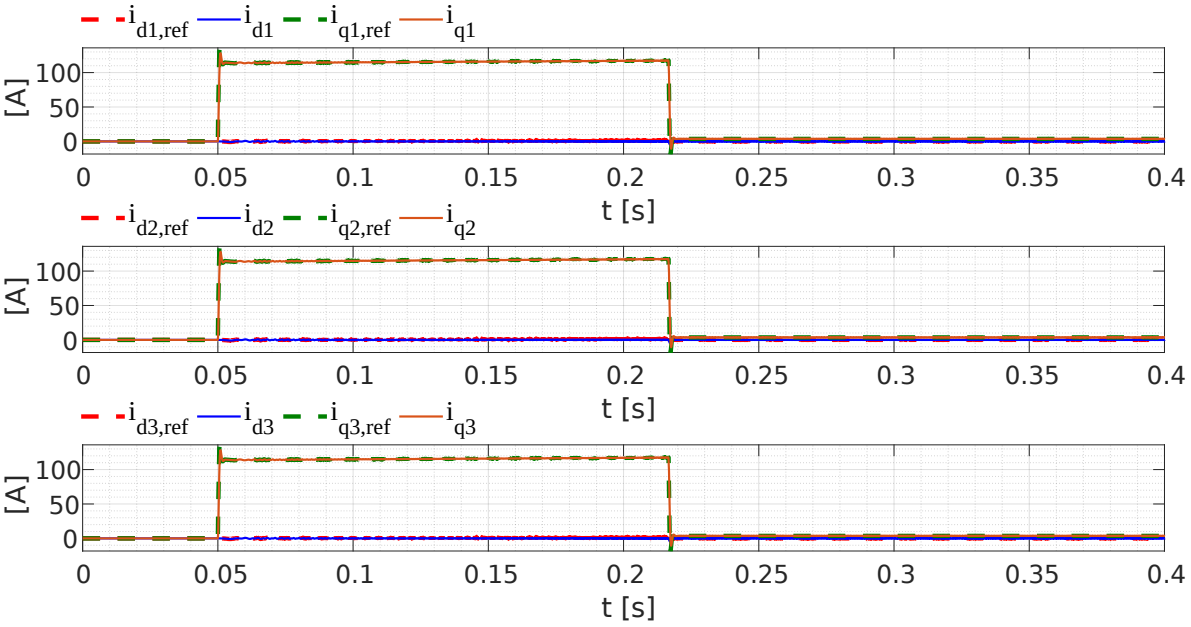

Figure 5.4: $d-q$ currents (constant speed, no force control)

As expected, even with the pseudo matrix approach, for the only torque control, the d-axis current is zero and only the q-axis current produces torque. Furthermore, in each sector, the q current is the same. This means that each sector contributes equally to torque production.

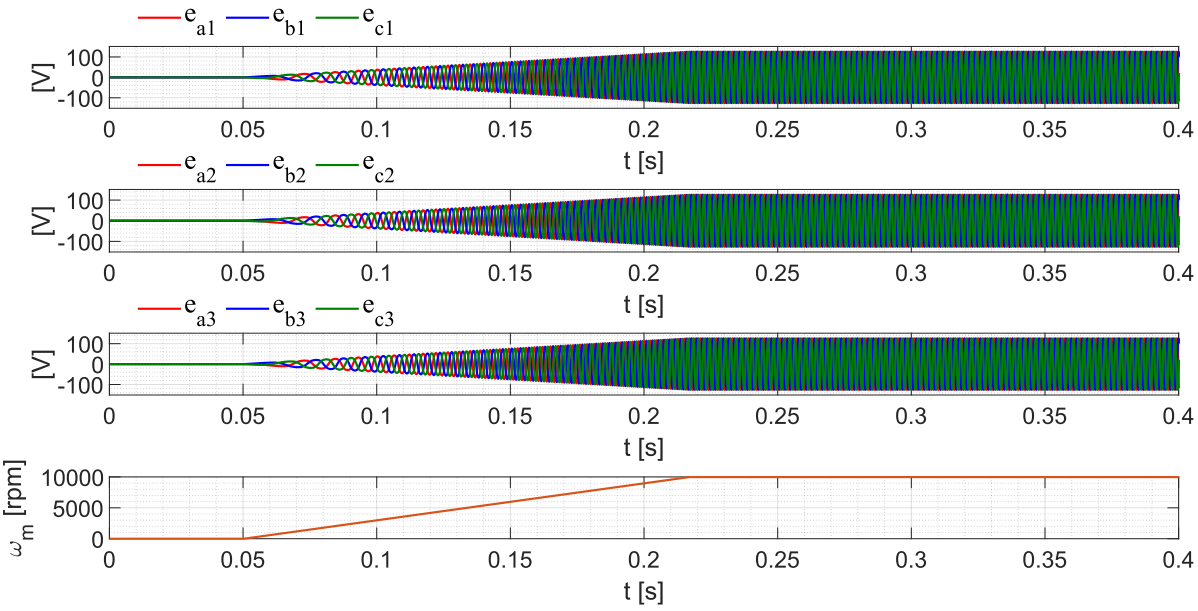

Figure 5.5: Back-emf waveform (constant speed, no force control)

The back-emfs are three symmetrical sinusoidal waveforms shifted by 120 electrical degrees each. Their amplitude is proportional to the speed and they are equal in each sector.

5.2.3 Displacement at the bearing locations

Figure 5.6 shows the displacement of the shaft at the bearing locations and the rotational speed of the shaft.

The shaft displacements at the bearing locations are equal and with the same phase. This means that the mode shape is cylindrical (equal bearings simulated).

5.3 Constant Force Simulation

In this section, a constant force reference along y-axis is set. The force reference is set as equal to the shaft weight $F_y^* = 500\ N$. The speed reference of $\omega_m^* = 10000\ rpm$ is set at $t = 0.05s$ and the simulation parameters are in tab. 5.1.

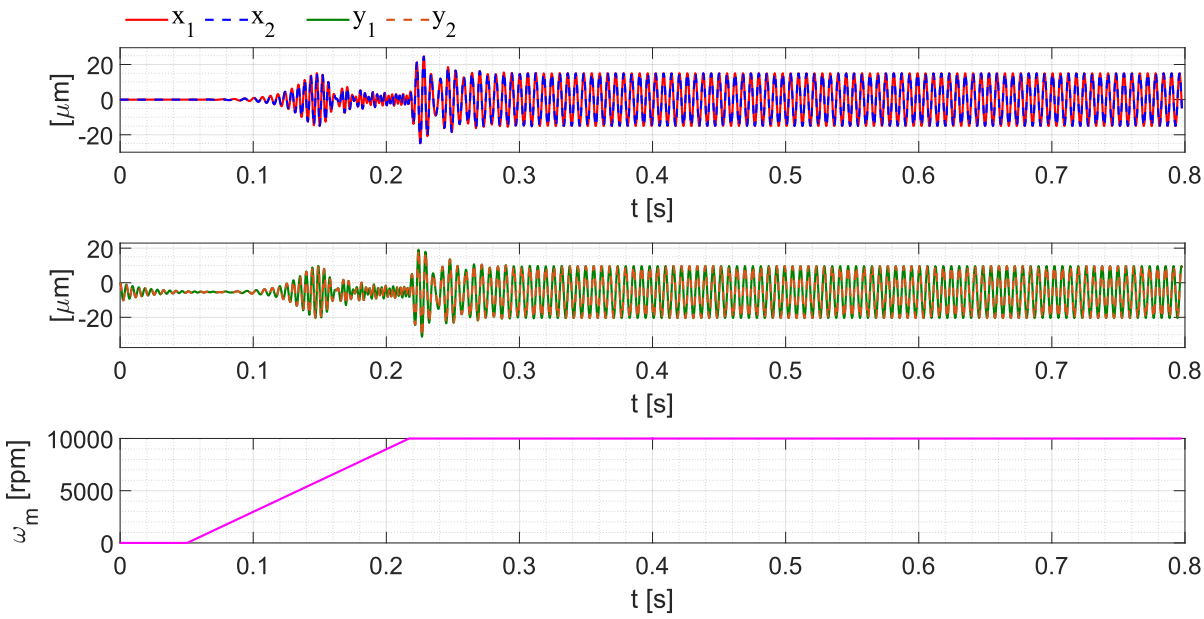

Figure 5.6: Shaft Displacement at the bearing locations

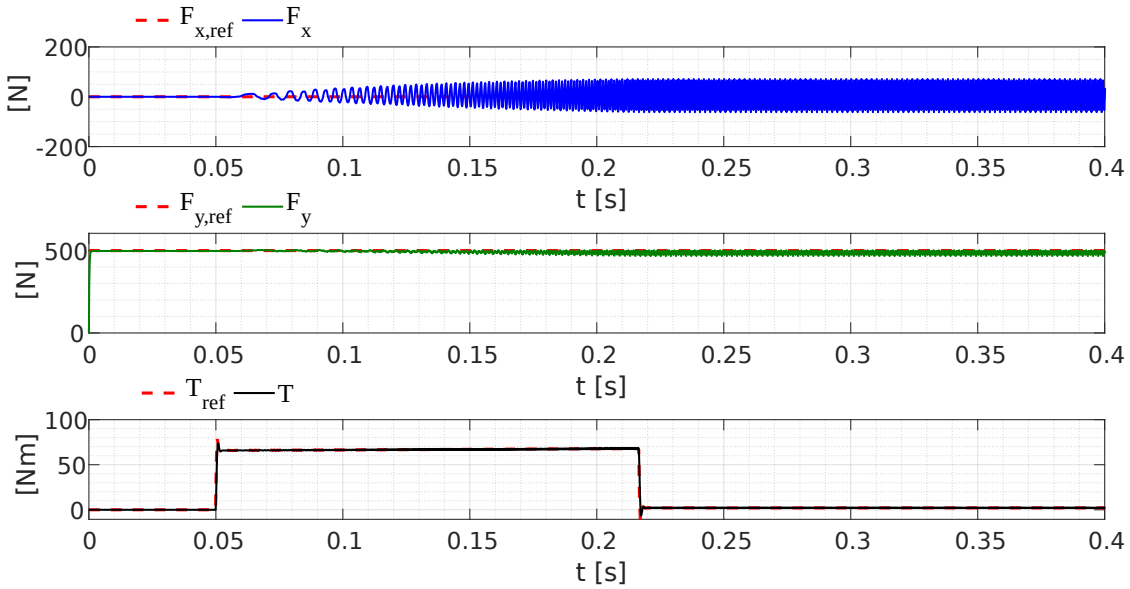

Figure 5.7: Wrench results (constant force control)

The force along the x-axis has a mean value equal to zero with an oscillation of $\pm 40N$. The force along the y-axis reaches the reference of 500 N with a negligible oscillation.

5.3.1 Current and Back-emf waveforms

The phase currents are shown in fig. 5.8

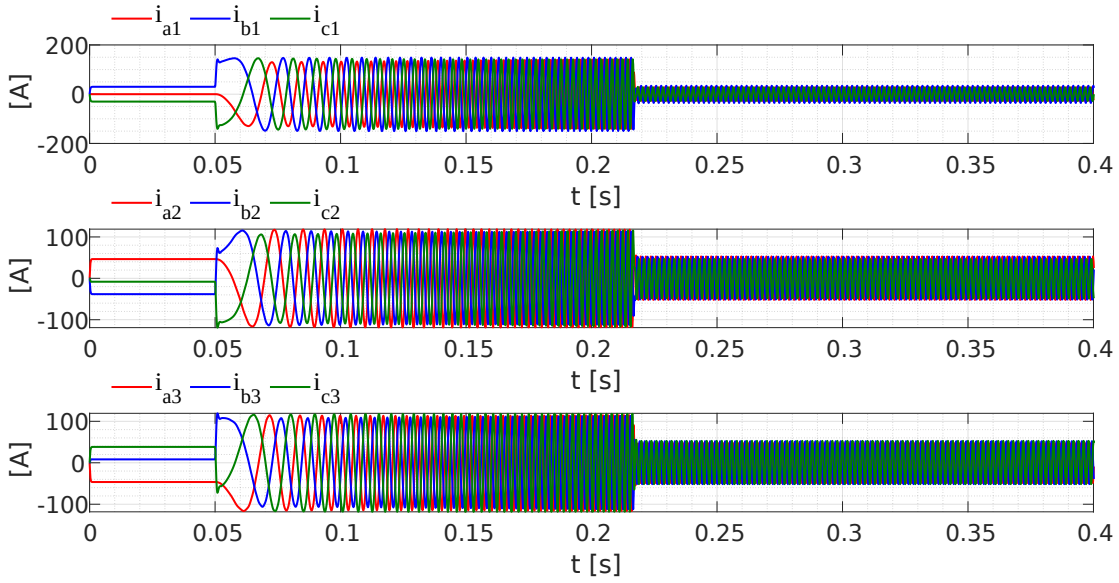

Figure 5.8: Currents waveforms (constant force control)

Figure 5.9 shows the $d-q$ currents.

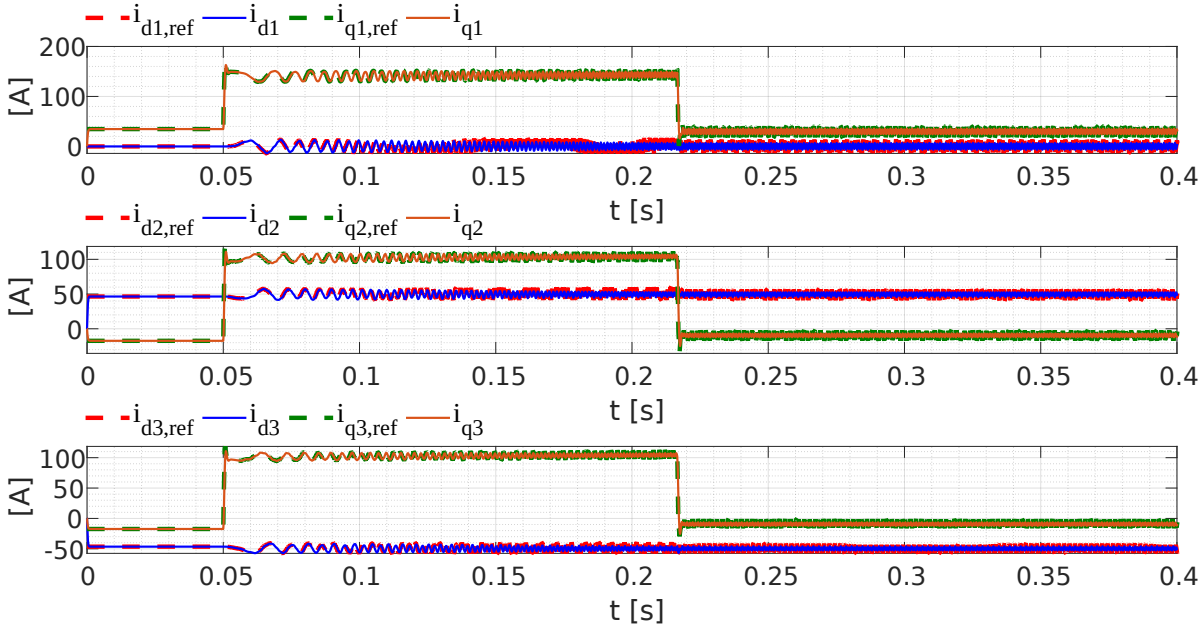

Figure 5.9: $d-q$ currents (constant force control)

To allow the force production, the d and q references present an oscillation with a frequency double the fundamental ($n_m = 10000\ rpm \ \rightarrow \ f = pn_m/60 = 500Hz,\ T = 0.002\ s$) as it possible in the focus (the currents waveforms are considered after the acceleration transient) in fig. 5.10.

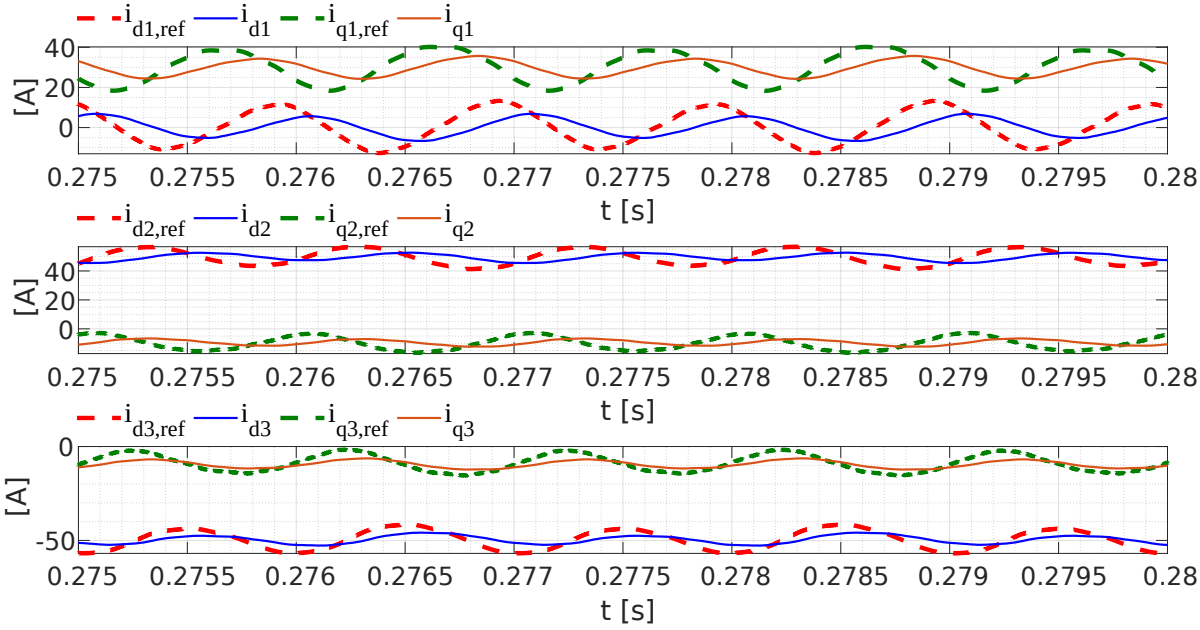

Figure 5.10: $d-q$ currents (constant force control) focus

As it is possible to see, both d and q currents contribute to the force production. In addition, the current references calculated with the pseudoinverse approach are not constant so, the PI current controllers follow the reference with delay.
The back-emf waveforms are the same as the previous case (they are determined only by the rotational speed), as it is possible to see in 5.11.

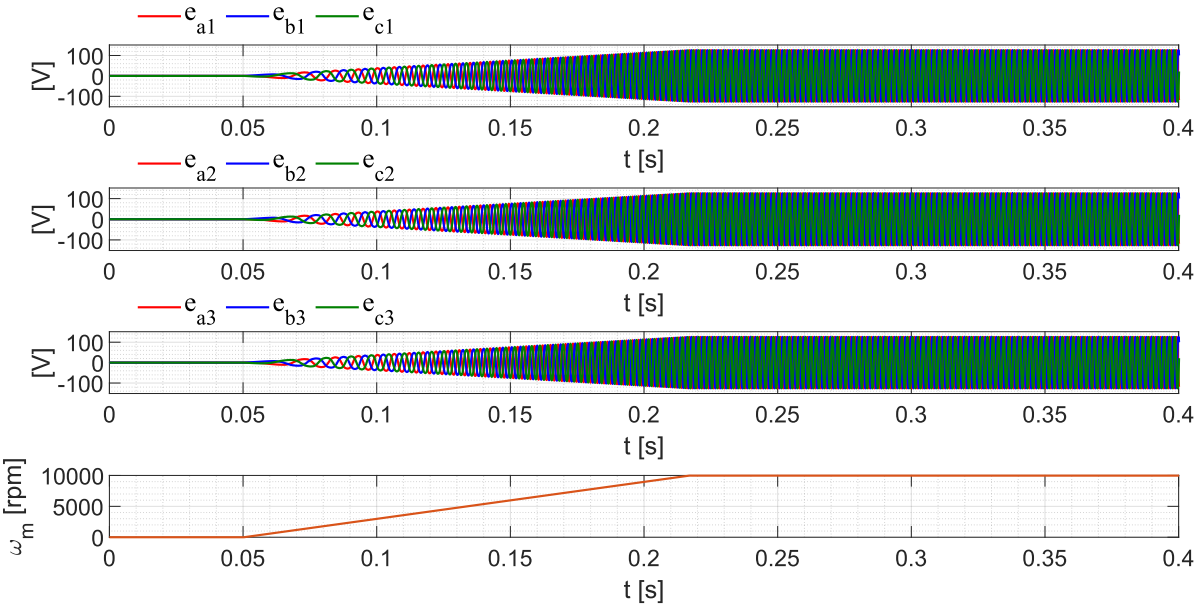

Figure 5.11: Back-emf waveform (constant force control)

5.3.2 Displacement at the bearing locations

Figure 5.12 shows the displacement of the shaft at the bearing locations and the rotational speed of the shaft.

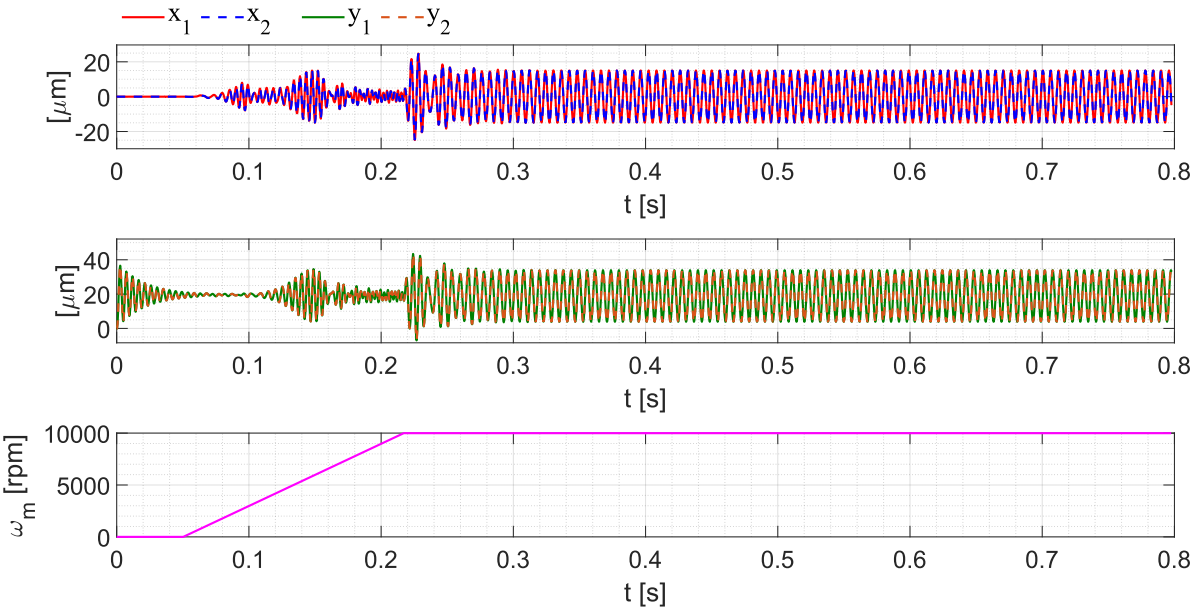

Figure 5.12: Shaft Displacement at the bearing locations

The shaft displacements at the bearing locations are equal and with the same phase. This means that the mode shape is cylindrical (equal bearings simulated).

5.4 Vibration Suppression control

In this section, the vibration suppression control is activated. This means that the displacement references are set to zero ($x^* = 0$ and $y^* = 0$) and the forces references are calculated in order to suppress the vibration of the shaft. In particular, the displacement feedback is:

- the mean of the shaft displacements x_1, x_2 and y_1, y_2 at bearing locations in the case of equal bearings;
- the shaft displacement x_1 and y_1 of the less rigid bearing in the case of different bearings.

5.4.1 Different Bearings

In this case, equal bearings are considered and the simulation parameters are in 5.2.

Mechanical parameters			**Initial Conditions**		
k_{x_1}	10	MN/m	$u(t=0)$	0	μm
k_{y_1}	10	MN/m	$v(t=0)$	0	μm
k_{x_2}	70	MN/m	$\theta_x(t=0)$	0	rad
k_{y_2}	70	MN/m	$\theta_y(t=0)$	0	rad
a	0.1769	m	$\dot{u}(t=0)$	0	$\mu m/s$
b	0.2175	m	$\dot{v}(t=0)$	0	$\mu m/s$
I_d	0.156502	kg m^2	$\dot{\theta}_x(t=0)$	0	s^{-1}
I_p	0.010468	kg m^2	$\dot{\theta}_y(t=0)$	0	s^{-1}
m	10.9904	kg			
c_1	500	Nm/s			
c_2	500	Nm/s			
ε	10	μm			

Table 5.2: Simulation parameters

The vibration suppression control is activated at $t = 0.5s$ when the speed has already reached the reference of 10000 rpm and all the transients are extinct. Figure 5.13 shows the wrench applied before and during the vibration control.

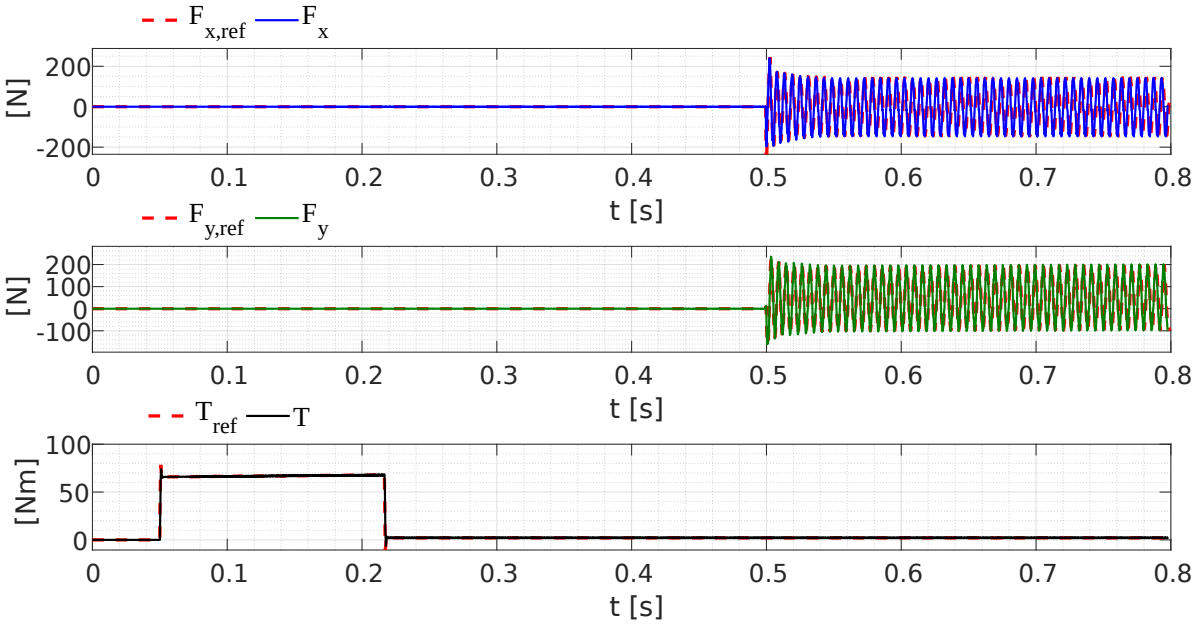

Figure 5.13: Wrench and speed results

As it is possible to see, the force applied is zero before $t = 0.5\ s$, and after the force, control is activated the force applied starts to follow the references calculated by the position control by using the shaft displacement at bearing 1 location as position feedback.

In figure 5.13, it is possible to see how the force applied by the machine is opposite to the out-of-balance force in order to compensate for the oscillations caused by the unbalanced rotor mass.

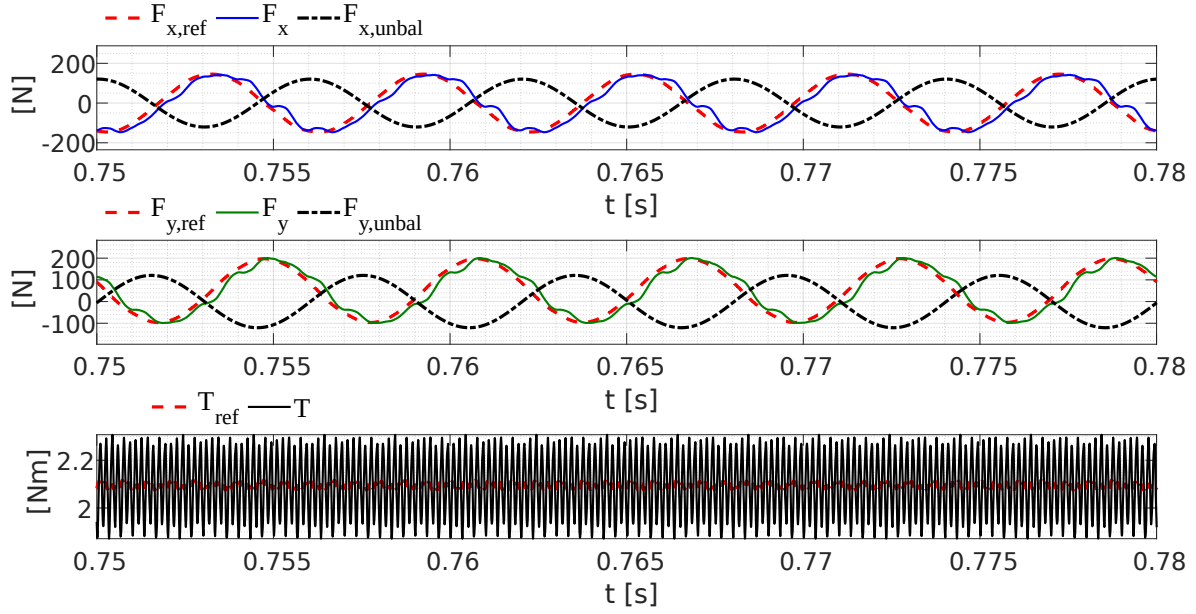

Figure 5.14: Wrench details

Currents and Back-emf waveforms

The Back-emf waveforms are the same as shown in figure 5.11 since the acceleration transient is the same.
The phase currents are shown in fig. 5.23

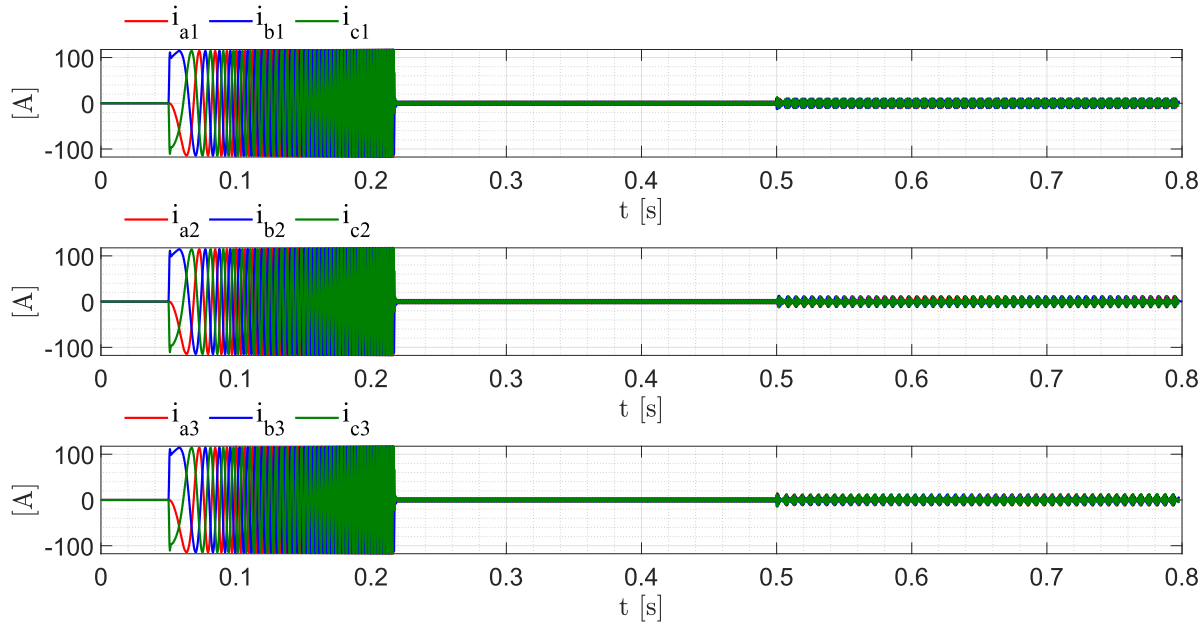

Figure 5.15: Currents waveforms (constant force control)

Before the activation of the force control (at $t = 0.3\ s$) the currents are three symmetrical sinusoidal waveforms (only torque the torque control is working).
In fig. 5.26 is shown a focus of the phase current waveforms during the force control:

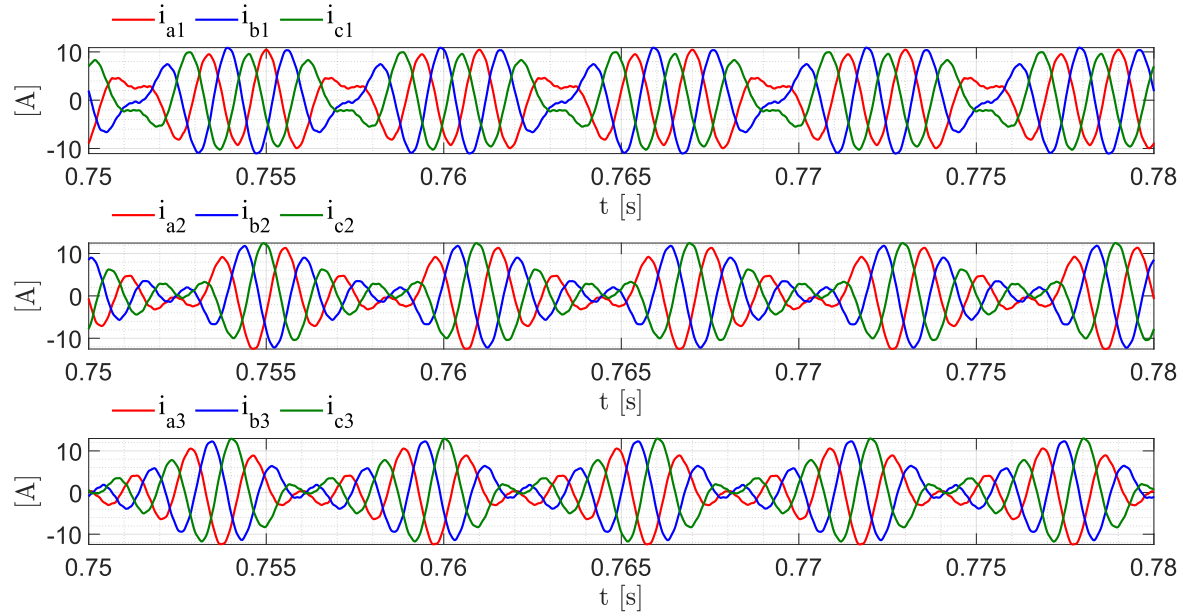

Figure 5.16: Currents waveforms focus (constant force control)

Figure 5.25 shows the $d-q$ currents and their references of each sector.

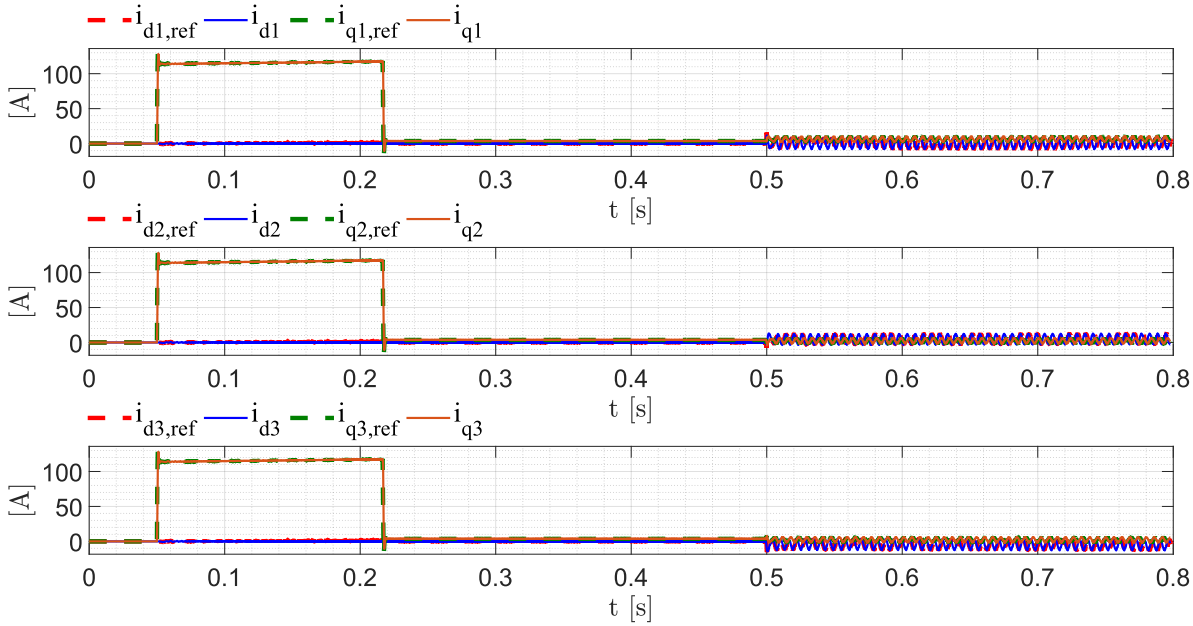

Figure 5.17: $d-q$ currents (constant force control)

The focus on the $d-q$ currents shows that the current control can follow the reference calculated from the pseudo-inverse approach with a small delay.

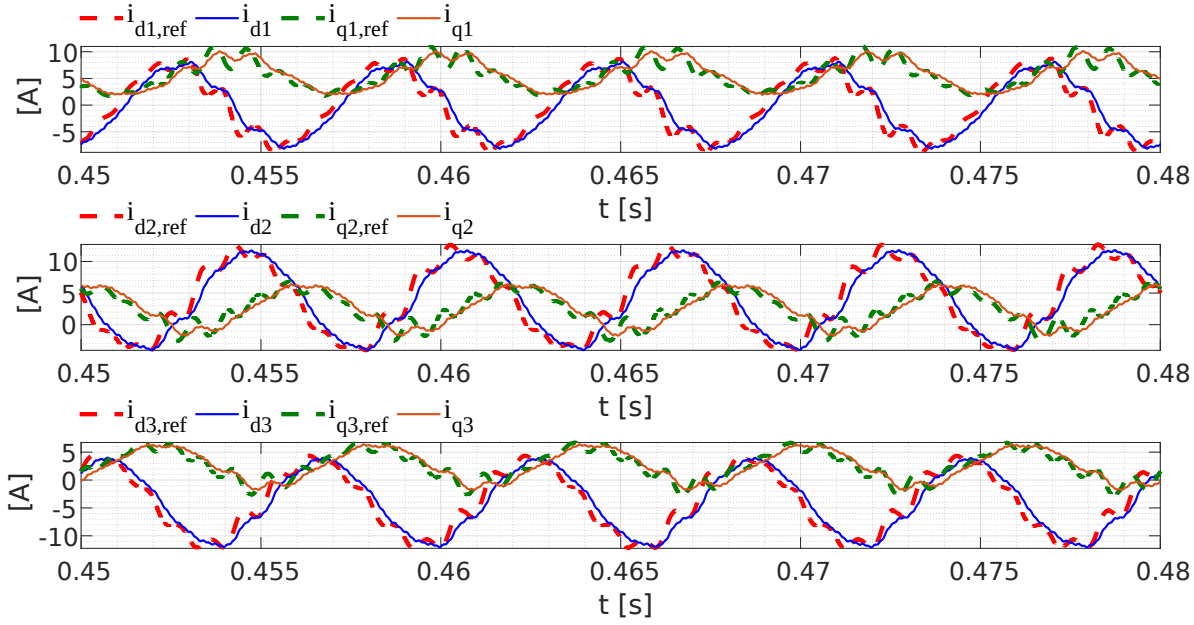

Figure 5.18: $d-q$ currents focus (constant force control)

Displacement at the bearing locations

Figure 5.19 shows the displacement of the shaft at the bearing locations and the rotational speed of the shaft.

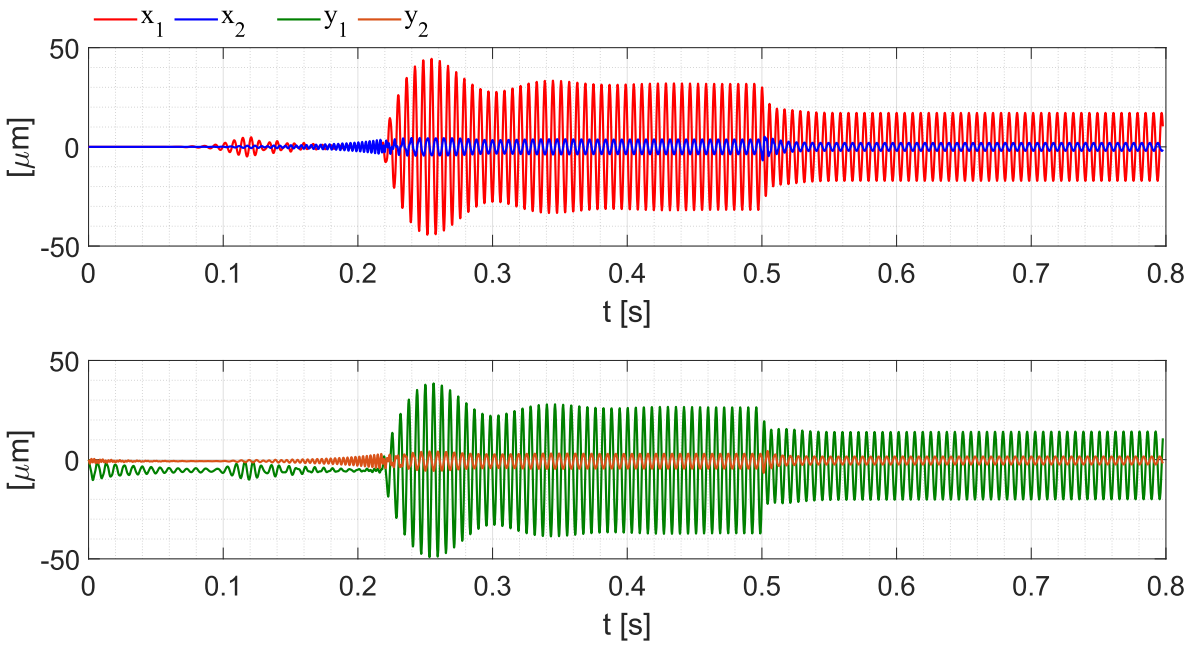

Figure 5.19: Shaft Displacement at the bearing locations

After the position control activation, the vibration of the shaft at the bearing locations is slightly reduced (the force control is not so effective in the vibration suppression).

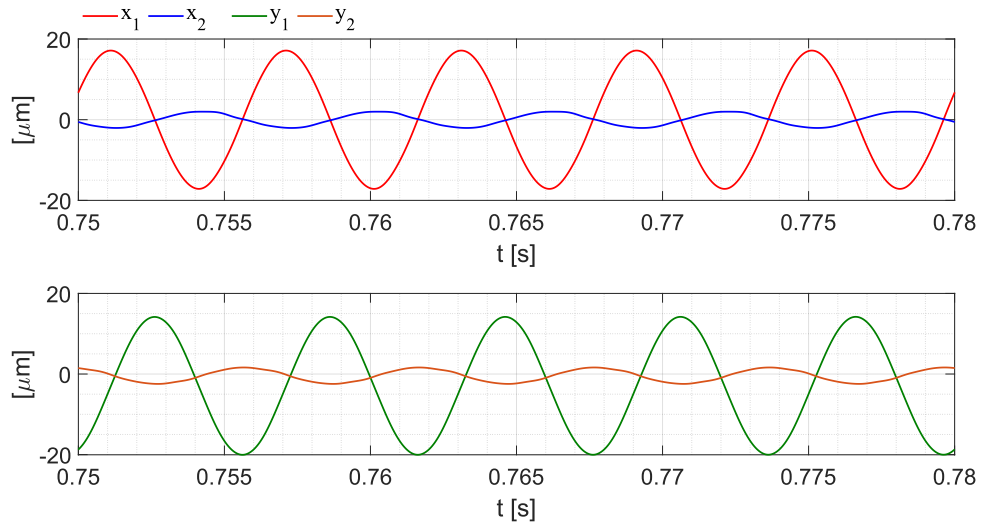

Figure 5.20: Shaft Displacement at the bearing locations

From figure 5.20, the mode shape remains conical after the force control activation since the displacements at bearings locations have opposite phases.

5.4.2 Equals Bearings

In this case, equal bearings are considered and the simulation parameters are in 5.1. The Vibration suppression control is activated at $t = 0.5s$ when the reference speed of 10000 rpm already reached and all the transients are ended. Figure 5.21 shows the wrench applied before and during the vibration control.

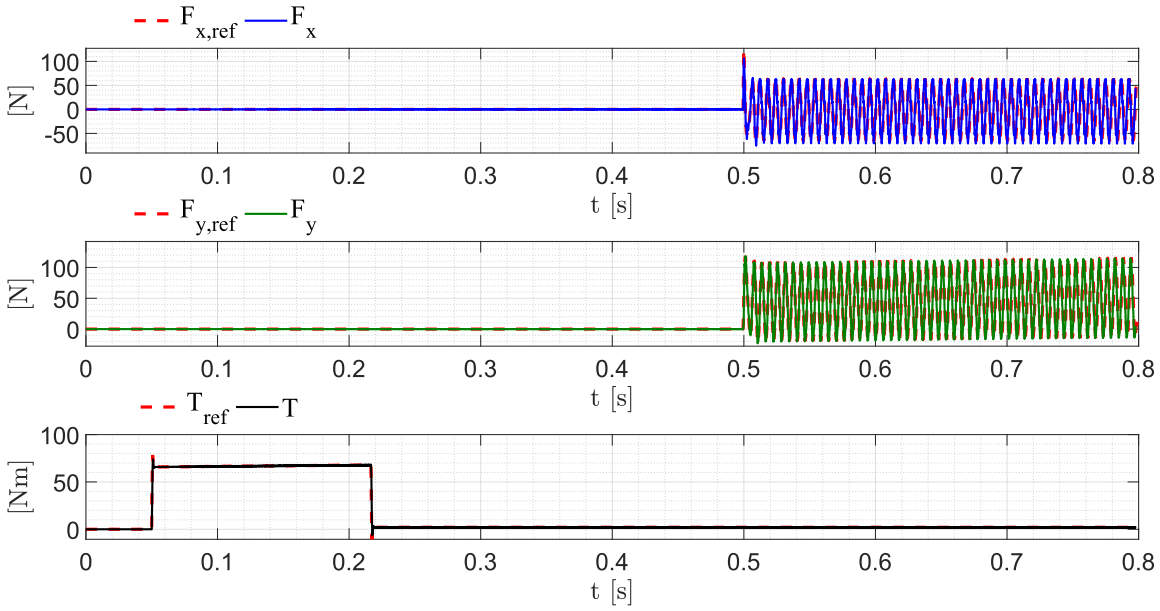

Figure 5.21: Wrench and speed results (constant force control)

As it is possible to see, the force applied is zero before $t = 0.5\ s$, and after the force, control is activated the force applied starts to follow the references calculated by the position control.

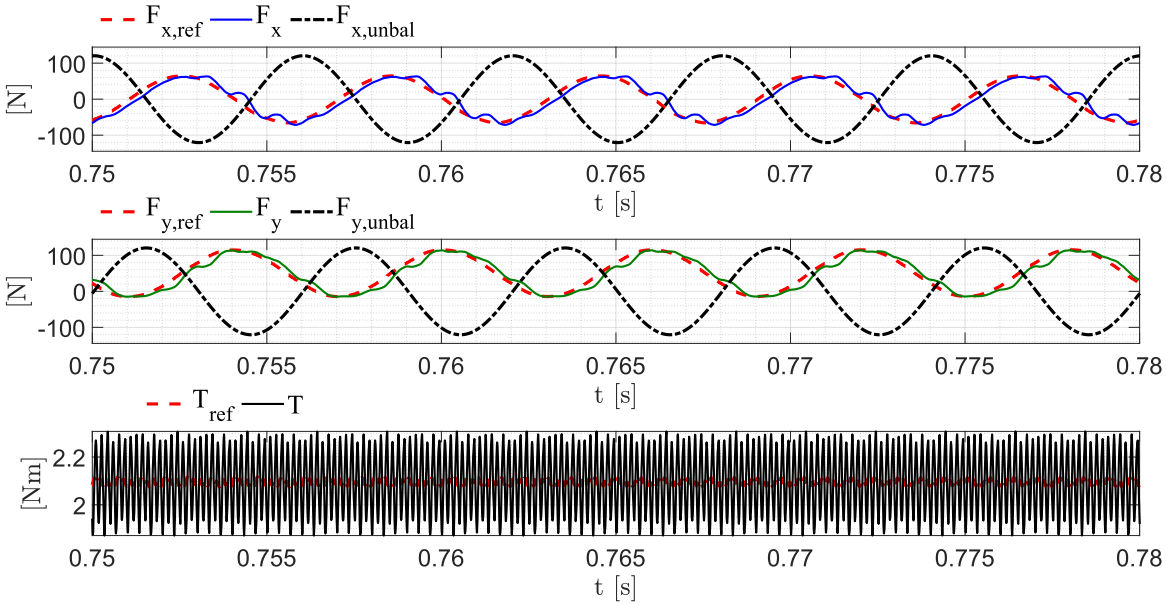

Figure 5.22: Wrench and speed results (constant force control)

From figure 5.20, the mode shape remains conical after the force control activation since the displacements at bearings locations have opposite phases.

Current and Back-emf waveforms

The Back-emf waveforms are the same as shown in figure 5.11 since the acceleration transient is the same.
The phase currents are shown in fig. 5.23

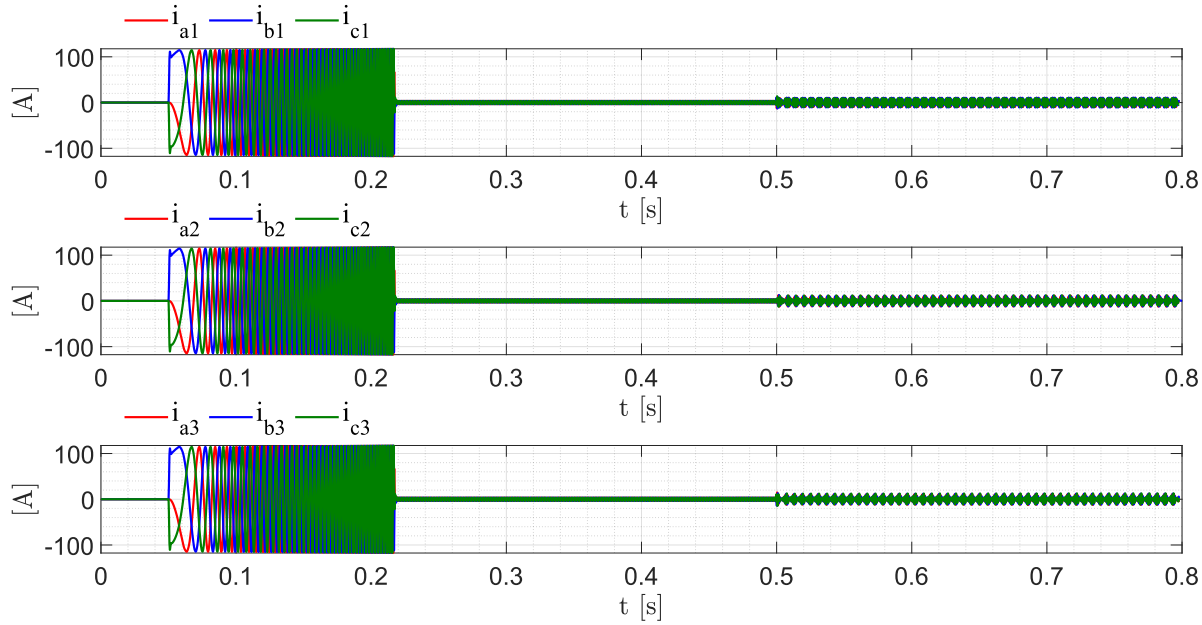

Figure 5.23: Currents waveforms (constant force control)

Before the activation of the force control (at $t = 0.3\ s$) the currents are three symmetrical sinusoidal waveforms (only torque the torque control is working).
In fig. 5.26 is shown a focus of the current waveforms during the force control:

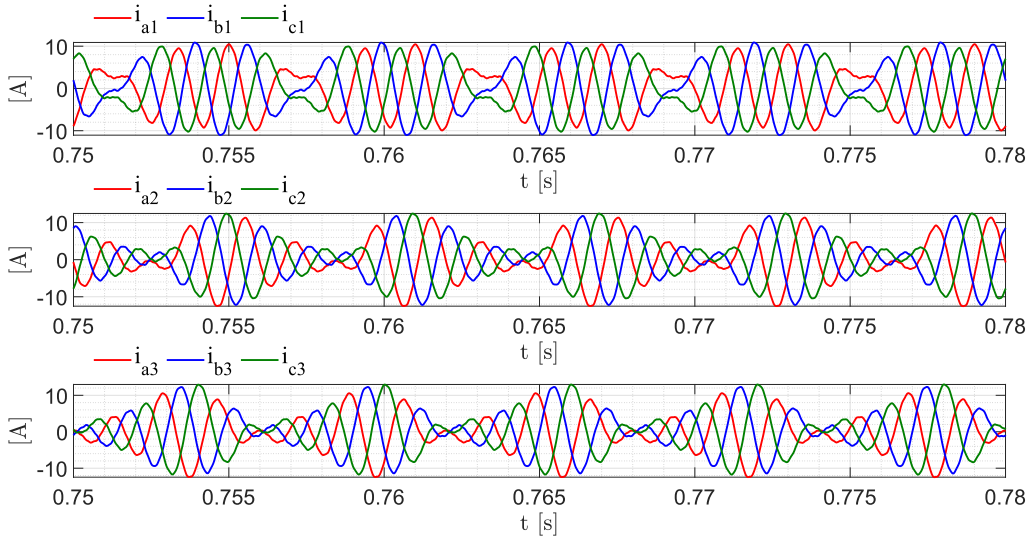

Figure 5.24: Currents waveforms focus (constant force control)

Figure 5.25 shows the $d-q$ currents of each sector.

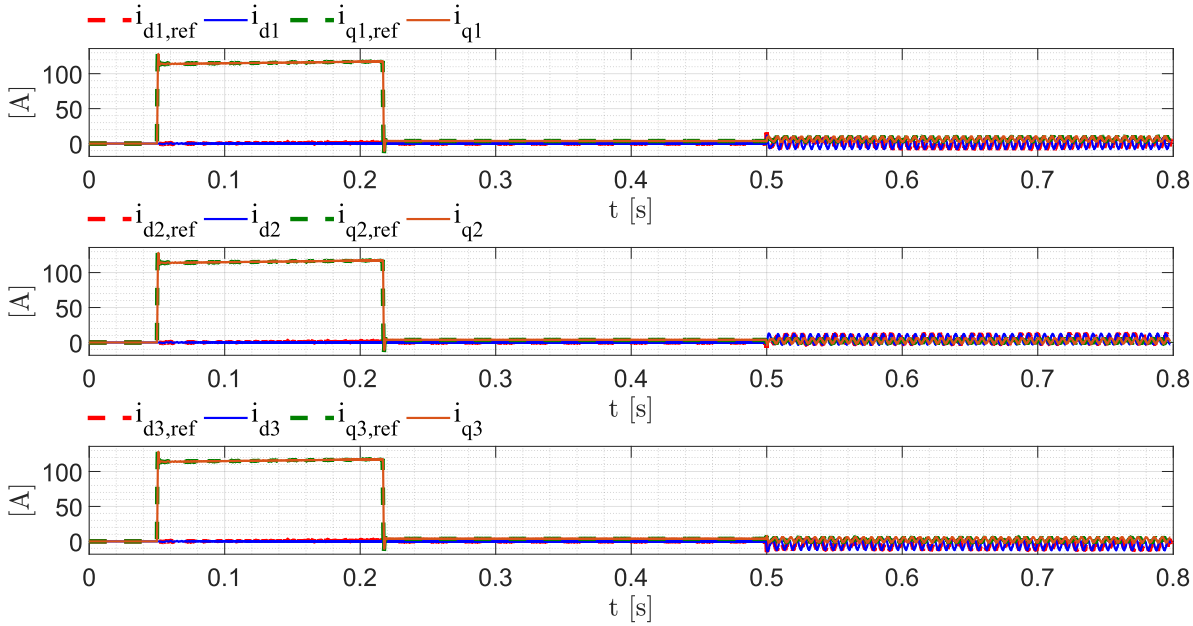

Figure 5.25: $d-q$ currents (constant force control)

The focus on the $d-q$ currents shows that the current control can follow the reference calculated from the pseudo-inverse approach.

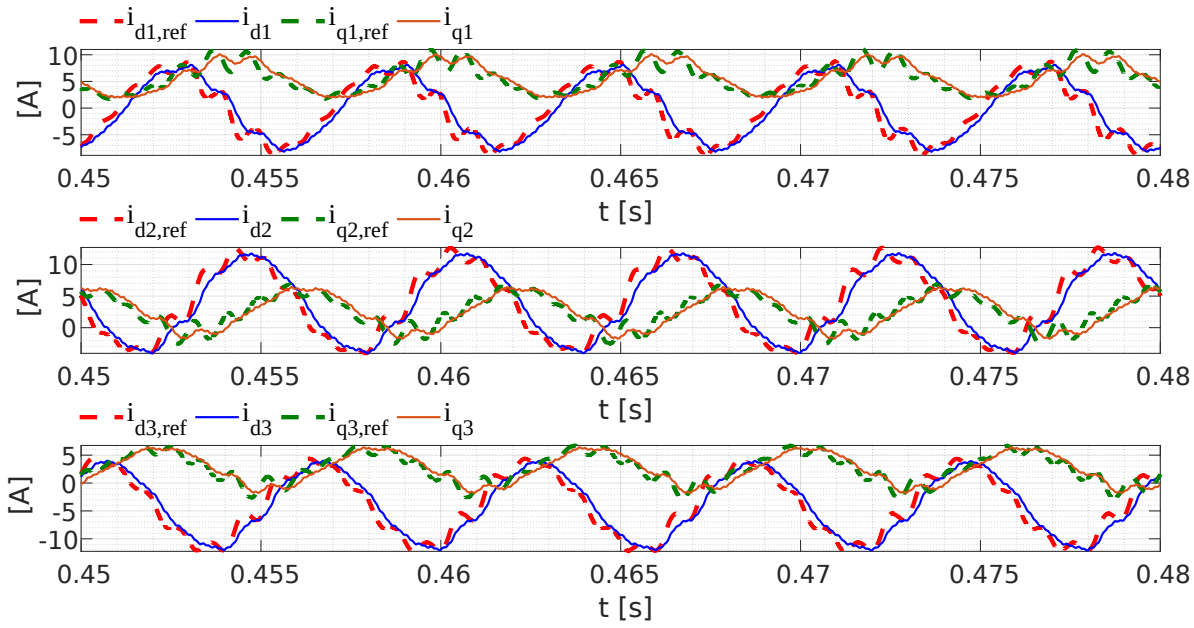

Figure 5.26: $d-q$ currents focus (constant force control)

Displacement at the bearing locations

Figure 5.27 shows the displacement of the shaft at the bearing locations and the rotational speed of the shaft.

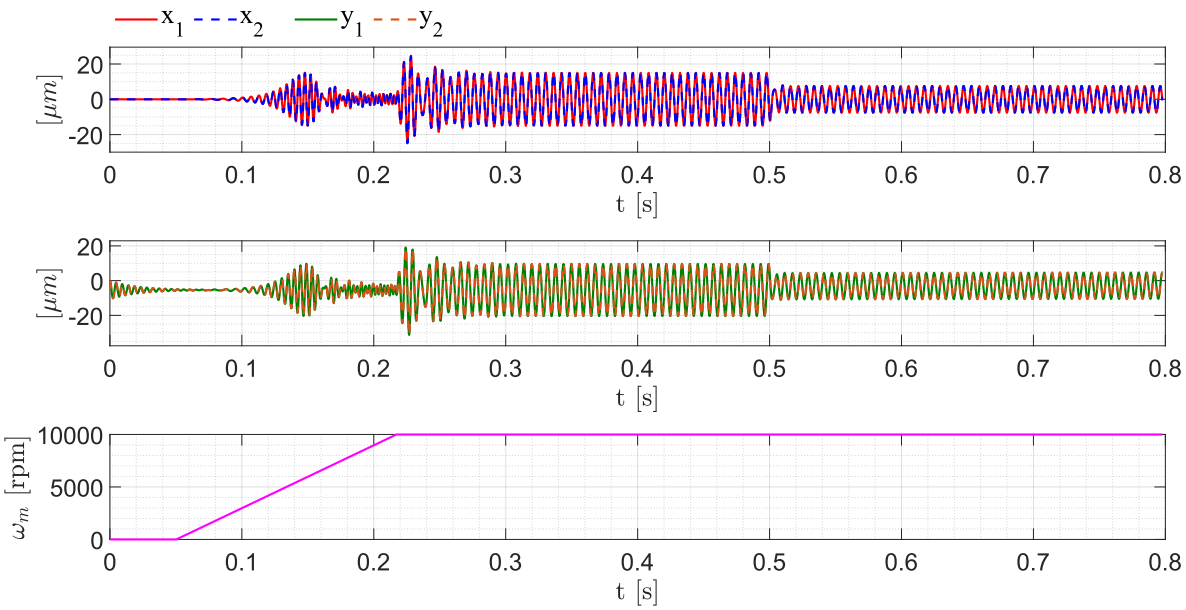

Figure 5.27: Shaft Displacement at the bearing locations

As it is possible to see, after the position control activation the vibration of the shaft at the bearing locations is reduced. Additionally, the mode shape remains cylindrical after the force control activation since the displacements at bearings locations have the same phases.

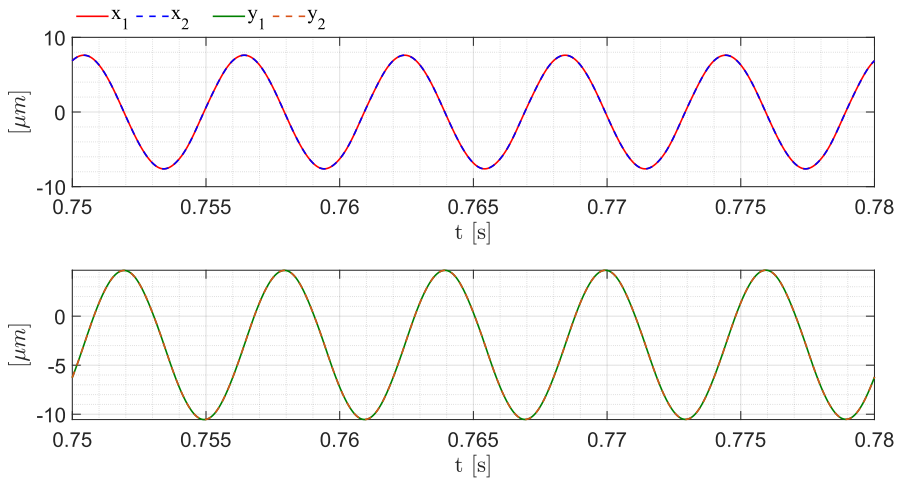

Figure 5.28: Shaft Displacement at the bearings locations after the force control(focus)

Additionally, from figure 5.28, the mode shape remains cylindrical after the force control activation since the displacements at bearings locations have the same angle.

5.5 Vibration Control at different speeds

In this section, the peak-to-peak vibration amplitude at both bearing locations is analyzed with and without force control. At first, the system is simulated without the motor force control. Subsequently, the force control is activated. The parameters used to carry out these simulations are reported in the tab. 5.1, as the two bearings are considered with equal stiffness $k_1 = k_2 = 10$ MN/m and damping $c_1 = c_2 =$ 500Nm/s.
Since the two bearings are equal, the peak-to-peak amplitude of the shaft displacements at the respective bearing locations is the same along x and y for both bearings ($\Delta x_1 = \Delta x_2 = \Delta x$ and $\Delta y_1 = \Delta y_2 = \Delta y$) and it is shown for different rotational speeds in Fig. 5.29.

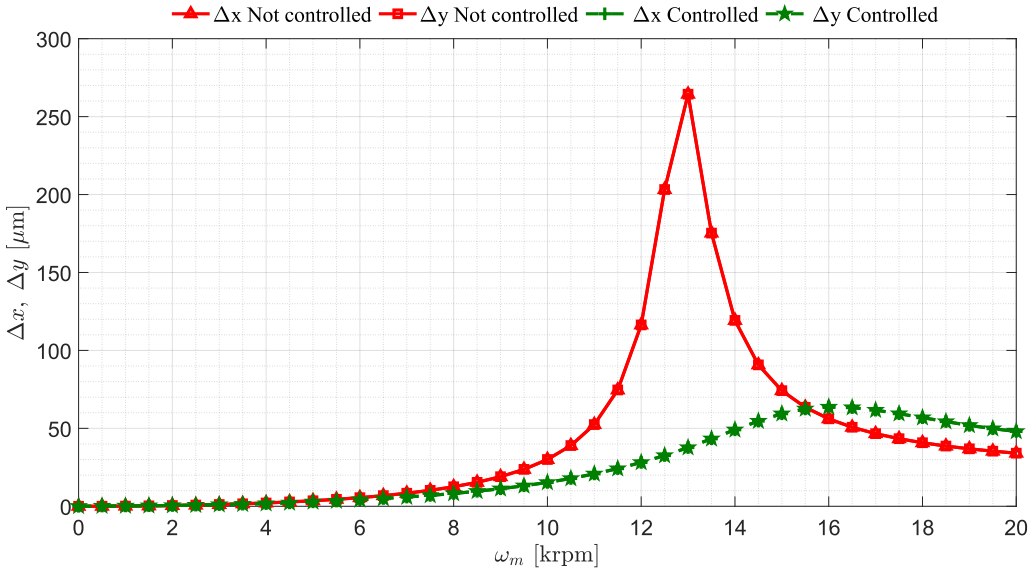

Figure 5.29: Peak-to-Peak vibrations amplitude at different rotational speeds at bearings locations

From the rotor free response analysis carried out in chapter 3.5, a natural frequency of around 215 Hz and a critical speed at roughly 13000 rpm are expected. This is confirmed in fig. 5.29.

5.5.1 Vibration Suppression at Critical Speed (Equal Bearings)

Fig. 5.30 shows the x and y displacement at bearing locations before and after the force control applied by the machine at 0.5 s.

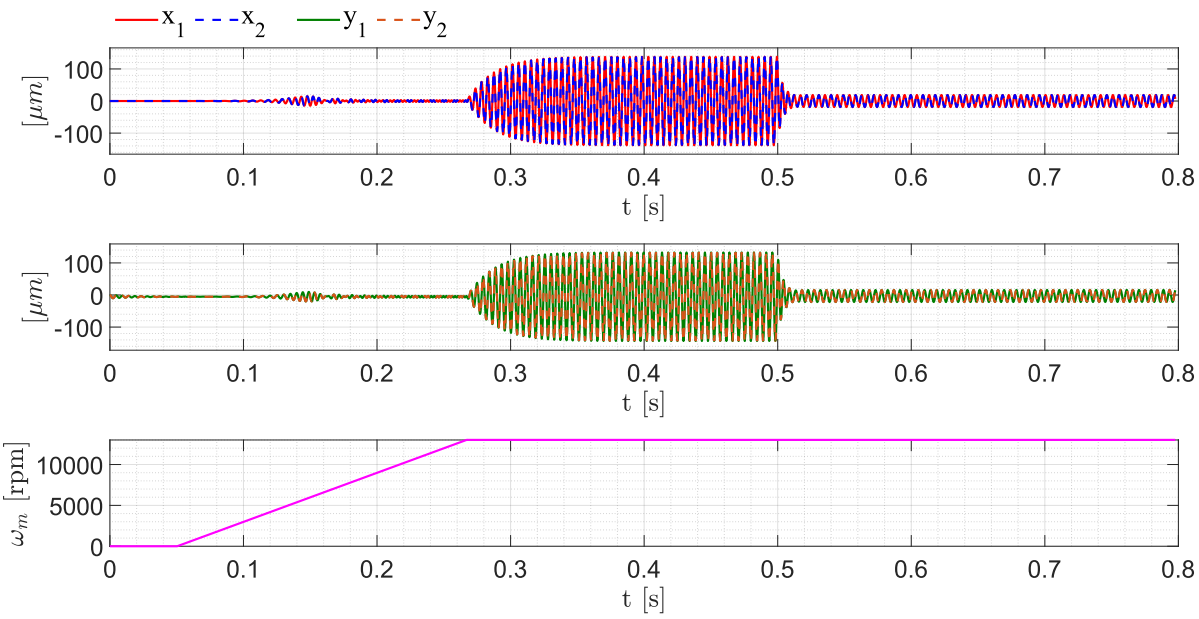

Figure 5.30: Shaft displacements at bearings locations at the critical speed.

The force control is significantly effective in reducing the vibration at the critical speed.

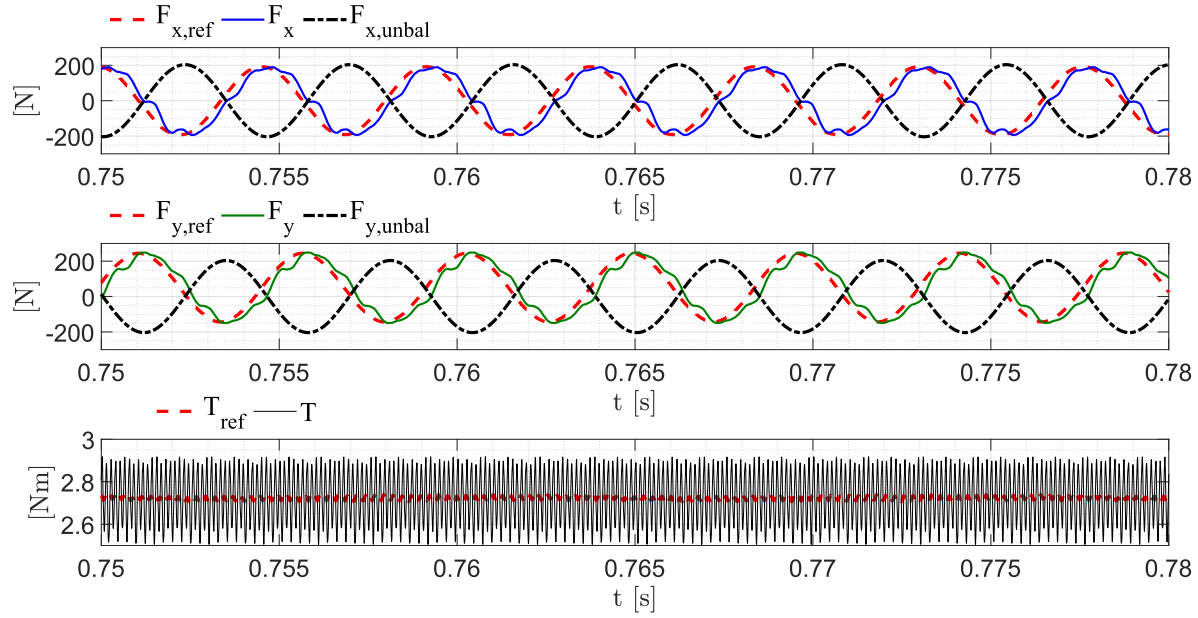

Figure 5.31: Wrench results at the critical speed.

From figure 5.31, it is possible to see how the force applied by the machine compensates effectively for the out-of-balance force of the rotor.

In figure 5.32 and 5.33 the $d-q$ and the phase currents during the vibration control are shown.

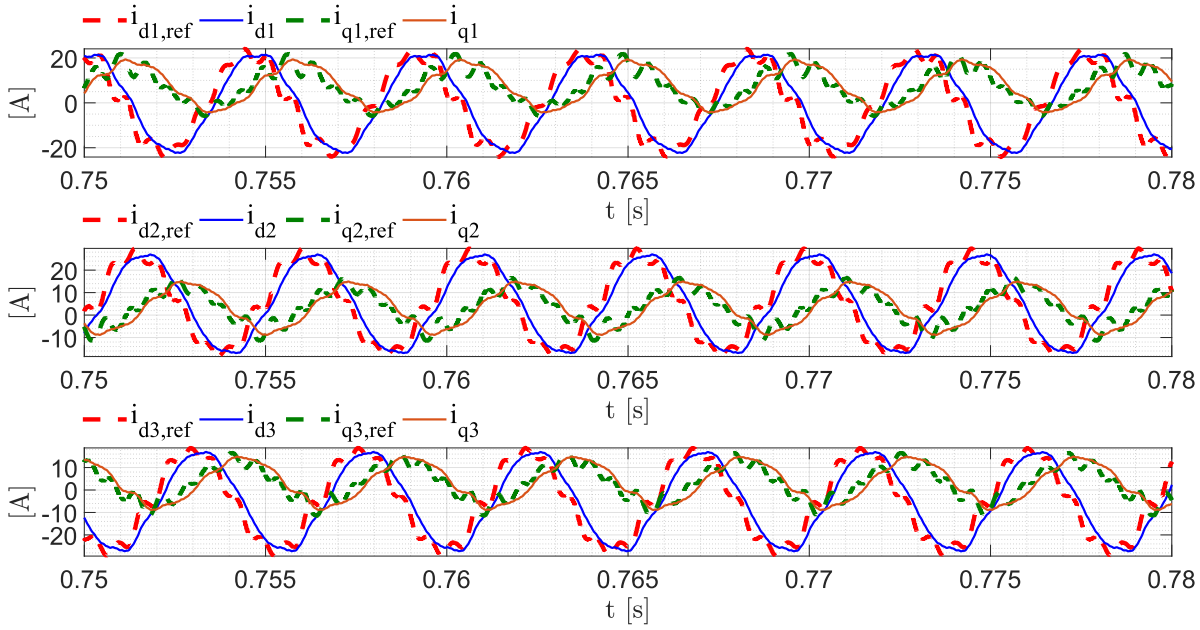

Figure 5.32: $d-q$ currents during the Vibration Control

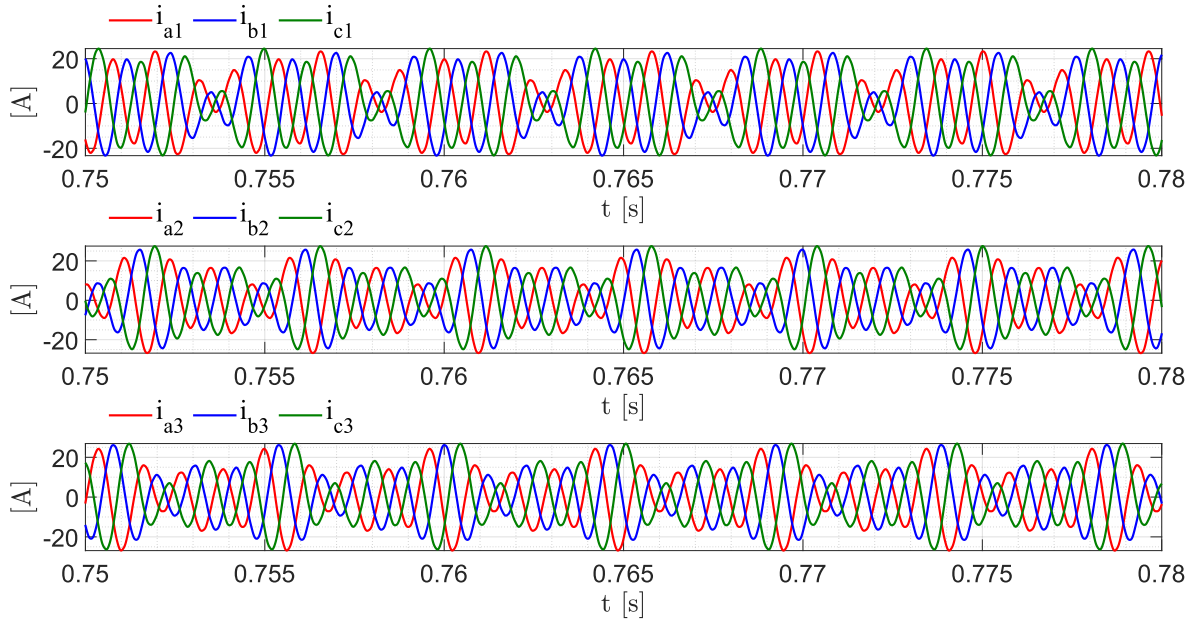

Figure 5.33: Phase Currents during the Vibration Control

5.5.2 Vibration Suppression at High Speed (Equal Bearings)

A speed reference of 18000 rpm has been set and the simulation results are presented in this section.

Fig. 5.34 shows the x and y displacement at bearing locations before and after the force control applied by the machine at 0.5 s.

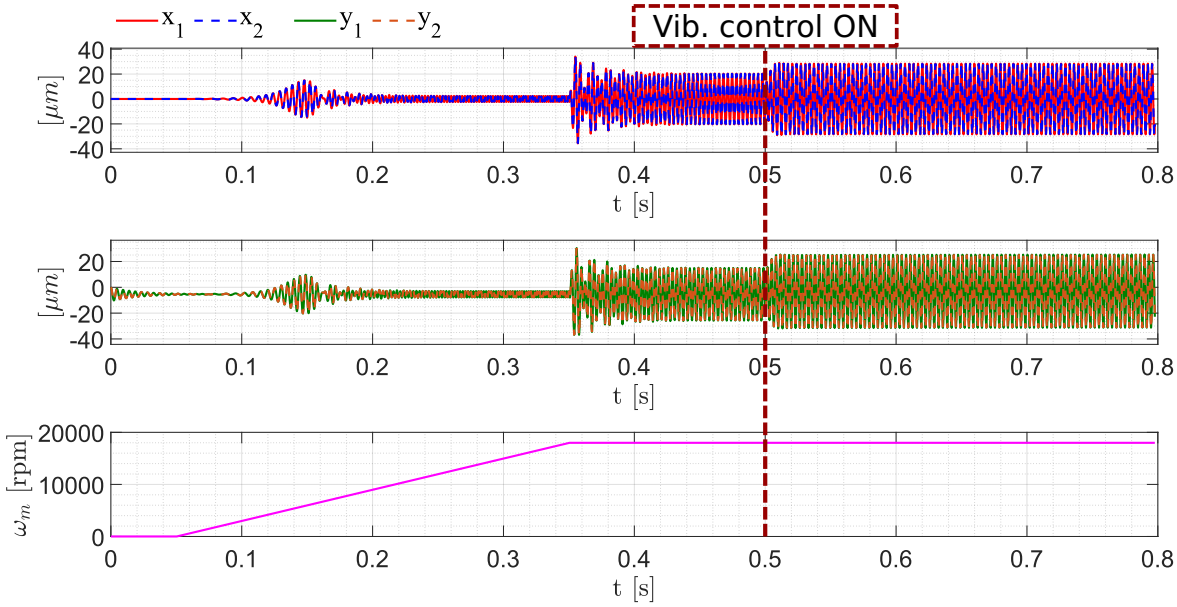

Figure 5.34: Shaft displacements at bearings locations at high speed (18000 rpm).

The force control is not effective in reducing the vibration at the high speed. The vibration amplitude results larger after the vibration control activation than before.

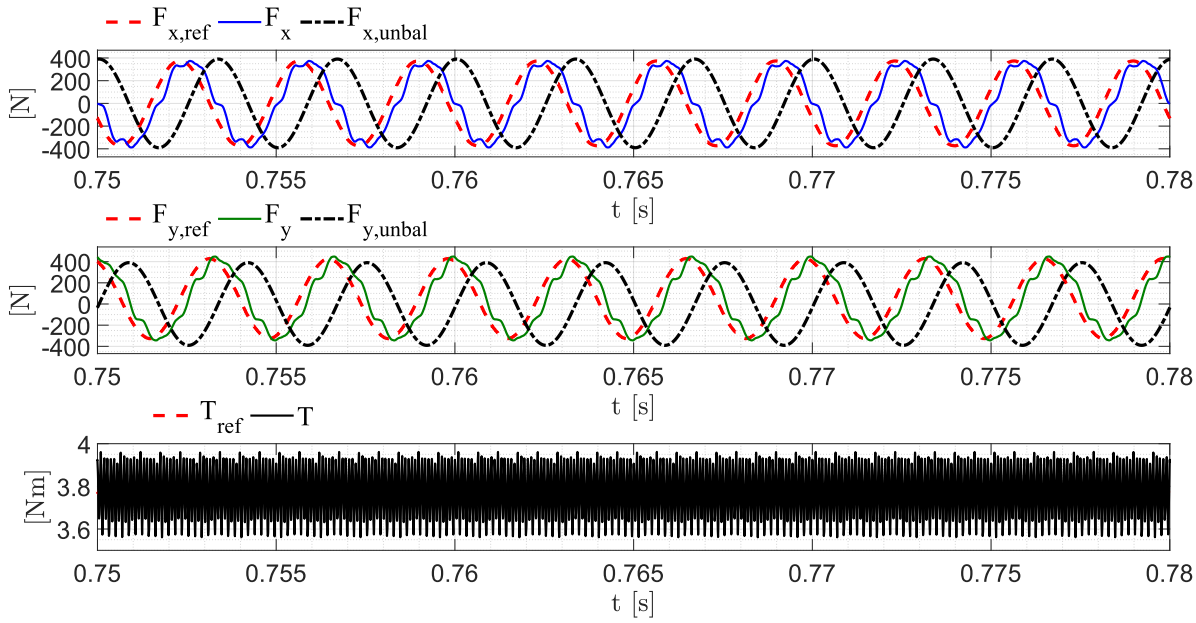

Figure 5.35: Wrench focus at high speed (18000 rpm).

From figure 5.35, it is possible to see how the force applied by the machine doesn't

compensate for the out-of-balance force of the rotor. The force applied by the machine is no anymore opposite to the out-of-balance force and it adds partially up to the unbalanced force making the vibration larger.

In figure 5.36 and 5.37 the $d-q$ and the phase currents during the vibration control are shown.

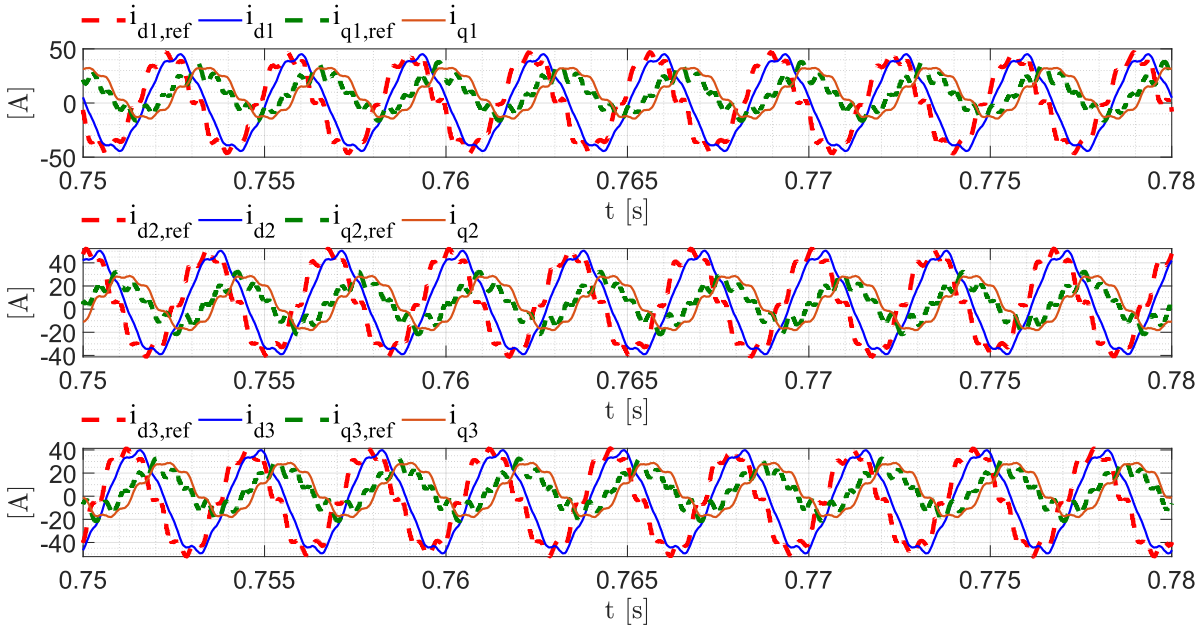

Figure 5.36: $d-q$ currents during the Vibration Control at high speed (18000 rpm).

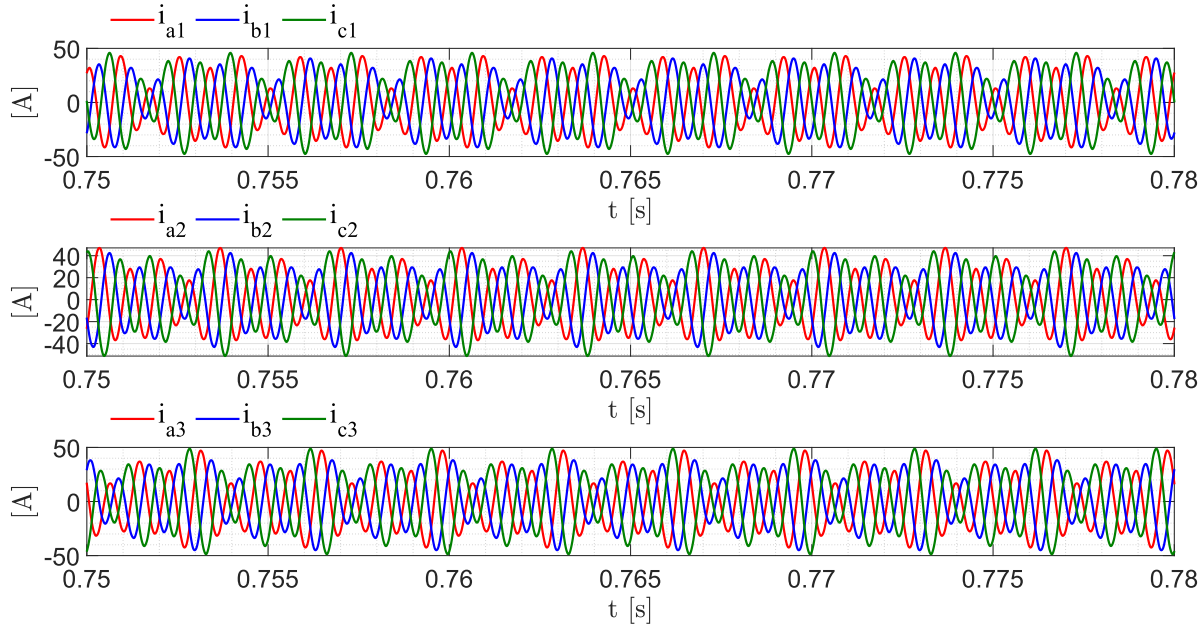

Figure 5.37: Phase Currents during the Vibration Control at high speed (18000 rpm).

Chapter 6

Experimental Results

In this chapter, the experimental setup and the test rig available in the PEMC (Power Electronic, Machine and Control) group laboratory at the University of Nottingham (Nottingham, UK) are introduced. Furthermore, the Back-emf tests carried out during this activity and their results are described.

6.1 Experimental Set-up

To test the radial force control a test rig is designed that can create comparable loading to the operational conditions of the aircraft, as shown in fig. 6.1 and 6.2.

6.1.1 Test Rig

The machine is driven by an asynchronous motor with a maximum speed of 20,000 rpm. The torque transferred over the total drive train is measured by a torque transducer. Two load units (two pneumatic cylinders capable of applying a radial force to the shaft) are considered on both ends of the machine's shaft, which can emulate different loading conditions including gyroscopic moments interference forces seen during real operation. A mechanism is considered between the load units and generator housing to move the load units circumferentially and apply force to the generator shaft from different angular positions with respect to the rotation axis. Using the measured radial shaft displacement, the bearing loads can be determined indirectly based on load-displacement ratios [48]. By decoupling the machine from the motor, the generator can be used in the motor state and the radial force control can be tested in a further application.

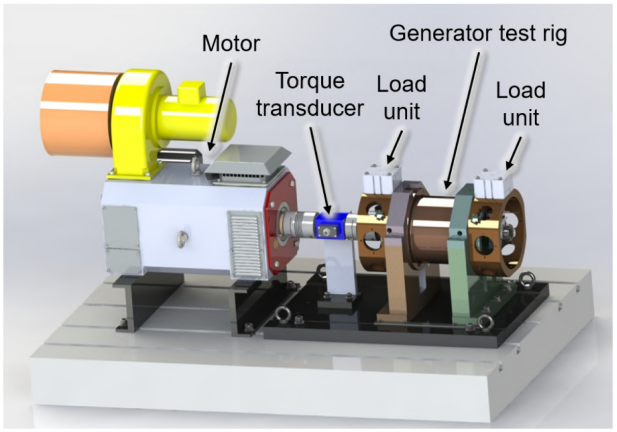

Figure 6.1: Test Rig CAD draw [33].

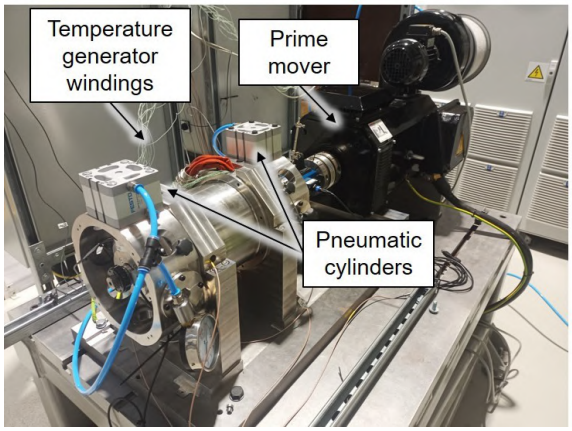

Figure 6.2: Test Rig photo.

6.1.2 Electric parts and sensors

The electric generator part is shown in a cross-section view with the integrated sensors in fig. 6.3. The machine is designed in a fixed-floating arrangement, with a cylindrical roller bearing (CRB) of the type N1008 with clearance on the driven side (input) and a spindle bearing package (SBP) of the type 7008 with a light preload class (65 N each bearing) on the non-driven side (output). The radial shaft displacement, which is the input value for the radial force control is measured close to the two bearing positions using three non-contact eddy current sensors arranged at 120° to each other on both sides. The interference forces of the load units $F_{RLU,i/o}$ are compensated by an electromagnetic force F_{RFC} from the generator to reduce loads of the cylindrical roller bearing F_{CRB} and the spindle bearing package F_{SBP}.

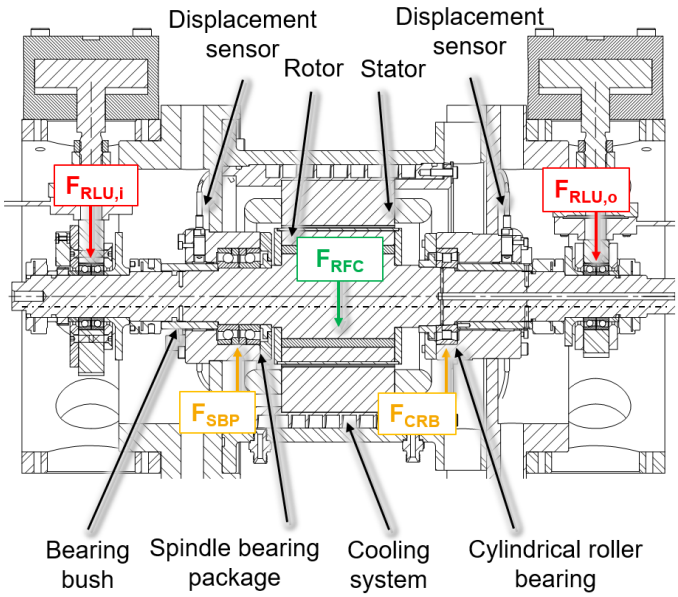

Figure 6.3: Machine section and force details [33].

It is important to consider that, this is the current bearing configuration of the

machine, however, to validate the model the two inner ball bearings will be removed, and the mechanical model of the machine is the one described in chapter 5, with bearing 1 and 2 are the equal bearings located under the load units.

6.1.3 Control and Measurement System

The radial force control is validated using acceleration, temperature, rotational speed, and torque signals. The sensor system to measure the operational behavior of the bearing is part of the bearing monitoring system. Figure 6.4 shows the output side of the generator test rig with a load unit and some of the sensors.

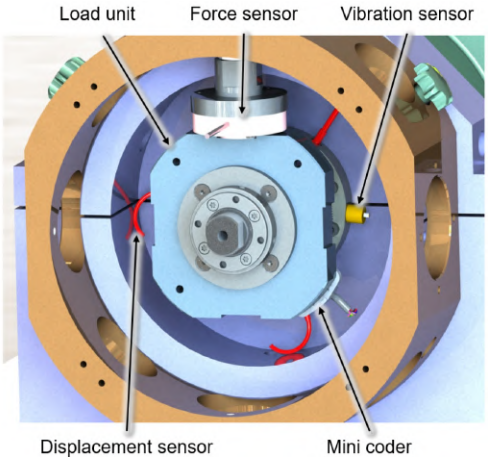

Figure 6.4: Load unit with sensors detail [33].

Two piezoelectric vibration sensors mounted on both sides of the bearing bushes provide information about the dynamic behavior of the test rig and the lubrication condition in the bearing by high-frequency measurements of the acceleration level of up to 51.2 kHz. The electromagnetic encoder measures the speed and angular position of the generator shaft and is the control input for the RFC (radial force control) application. The force sensors measure the actual force applied by the load units and also provide feedback on pneumatic cylinders' force control. Furthermore, the bearing temperatures are measured with resistance thermometers to determine the steady-state conditions. The cage speed of the generator bearing is monitored by infrared sensors to validate the slip and skidding behavior of the cylindrical roller bearing in critical operational conditions. The measured torque on the drive train can also be a suitably measured variable for evaluating radial force control.

The measurement data acquisition is performed by using a National Instrument Labview^{TM} software specifically developed for this application.

The sensors interface cabinet is shown in figure 6.5:

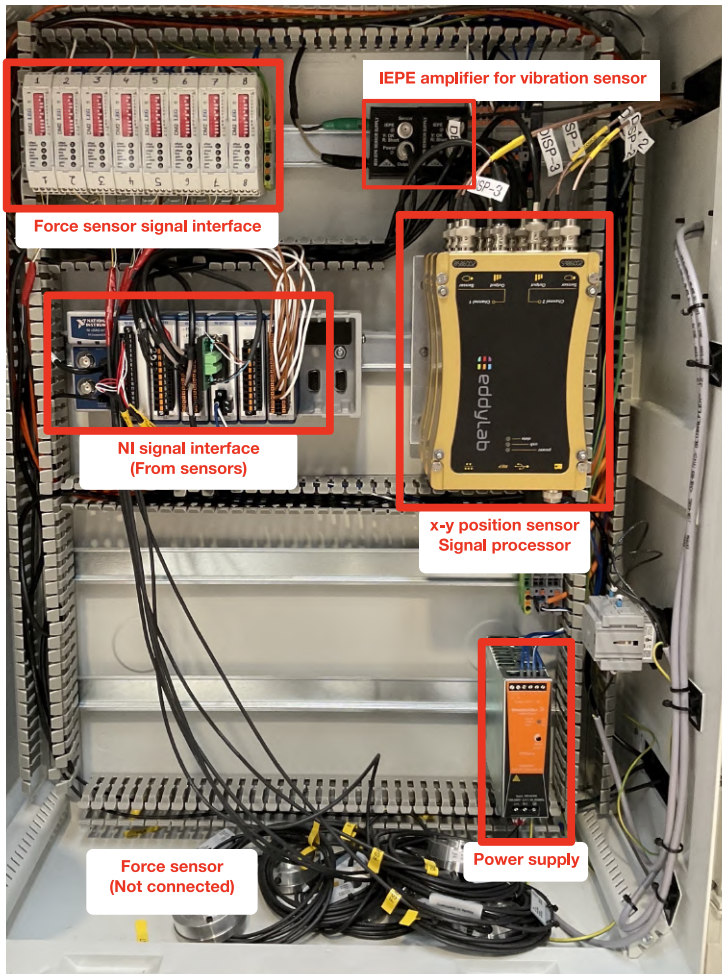

Figure 6.5: Sensors Interface Cabinet.

The sensor interfaces are mounted in a cabinet located close to the machine winding terminal box that allows the connection with the three three-phase inverters, as shown in fig. 6.6.

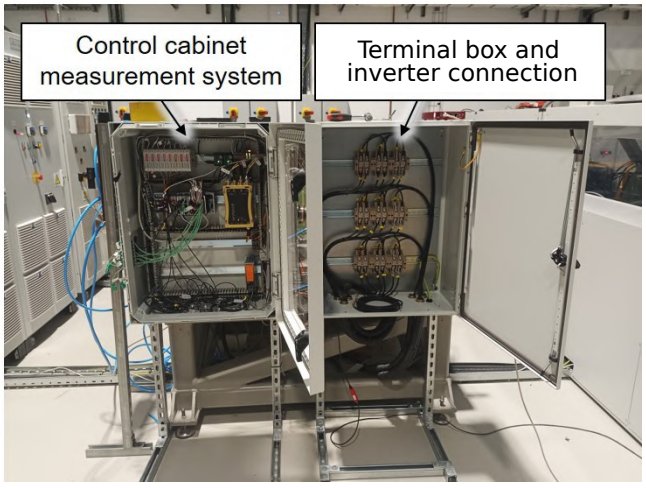

Figure 6.6: Sensors Interface Cabinet.

6.1.4 Converters Setup

The experimental setup with the three three-phase converters and the oscilloscopes that acquire the voltage at the terminals of the converters are depicted in 6.7.

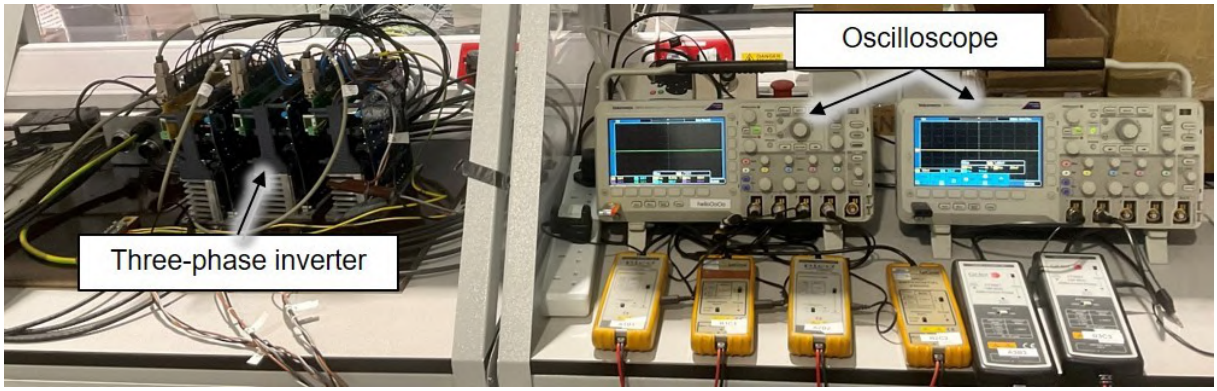

Figure 6.7: Inverters and Oscilloscopes.

It is important to underline that this converter setup is a temporary solution taken from a smaller rig since the three three-phase converters designed for this rig are not available yet. The converters are controlled by an interface developed internally within the PEMC group based on an FPGA architecture. The main converter parameters are in the tab. 6.1.

CONVERTER PARAMETERS		
Max Current	20	A
DC max voltage	200	V
Switching frequency	10	kHz

Table 6.1: Main three-phase converter parameters.

6.2 Experimental Tests

All the rig and sensor functionality has been tested (pneumatic load application, converters, and their sensors functionality). Finally, the back-emf test has been performed.

6.2.1 Back-emfs Test

The back EMF test (back ElectroMotive Force) is a test to characterize the induced electromotive forces induced in the stator winding of an electrical machine. The prime mover runs the machine while the stator windings are opened and the electromotive forces induced in the stator windings by the rotor magnets are measured. The main purpose of this test is to check if the machine is symmetrical (no relevant eccentricity on the rotor)

and if the windings are manufactured with the same number of turns. This test allows also to validate the finite element model used to perform the simulation results. Furthermore, with the back-emf test, it is possible to evaluate the harmonic content of the rotor magnets and it is possible to verify if the harmonics are those expected by the machine design.

Back-emf test results

The back-EMF validation is performed by comparing the FEA and experimental results in open-circuit conditions. The latter has been obtained by driving the machine at various rotational speeds (within the machine operative range) by means of an external load and measuring the voltage between consecutive phases with an oscilloscope. The following figures present the experimental line-to-line back-EMF waveforms of the three motor sectors at different rotational speeds (500 rpm, 1000 rpm, 3000 rpm, 4000 rpm, 5000 rpm). For brevity's sake, only the waveforms at 5000 rpm are shown in fig. 6.8, but the same analysis is performed for each speed tested:

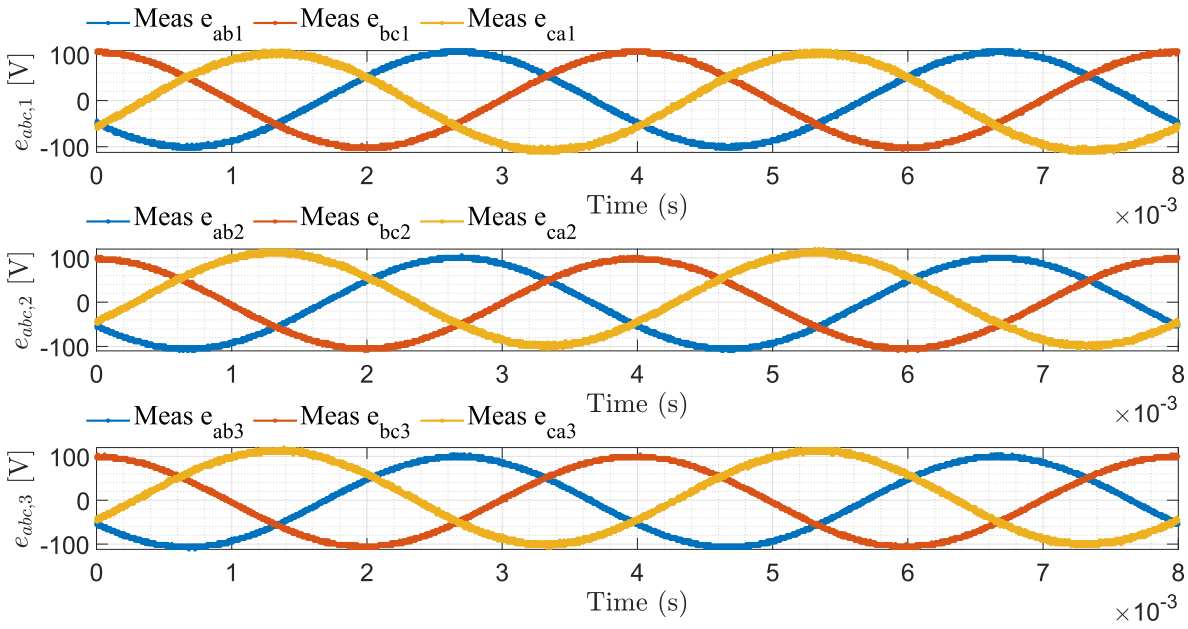

Figure 6.8: Line-to-Line experimental Back-emf waveform at 5000 rpm.

It can be noticed that the same phases in different sectors present identical back-EMF waveforms since they are located in an equivalent electrical position. For each sector, the FFT (Fast Fourier Transform) is performed and the experimental Back-EMF, FEA back-EMF, and rebuilt from FFT waveforms are compared in 6.9.

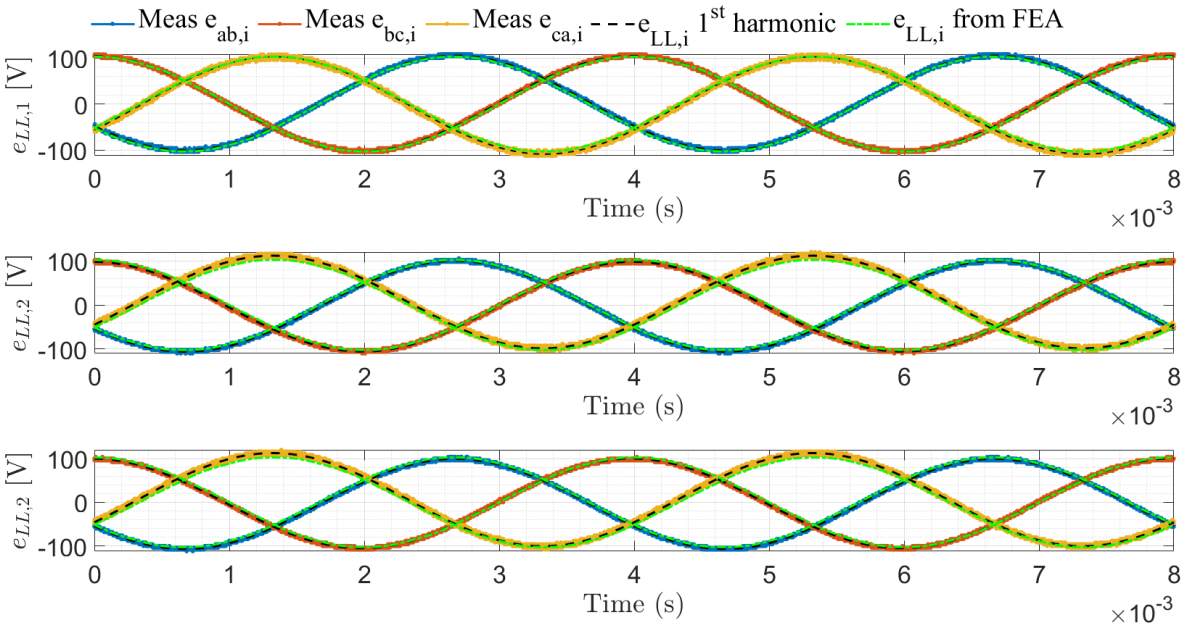

Figure 6.9: Line-to-Line Experimental and FEA Back-emf waveform comparison at 5000 rpm.

The FEA results in a good prediction if compared with respect to the experimental values.

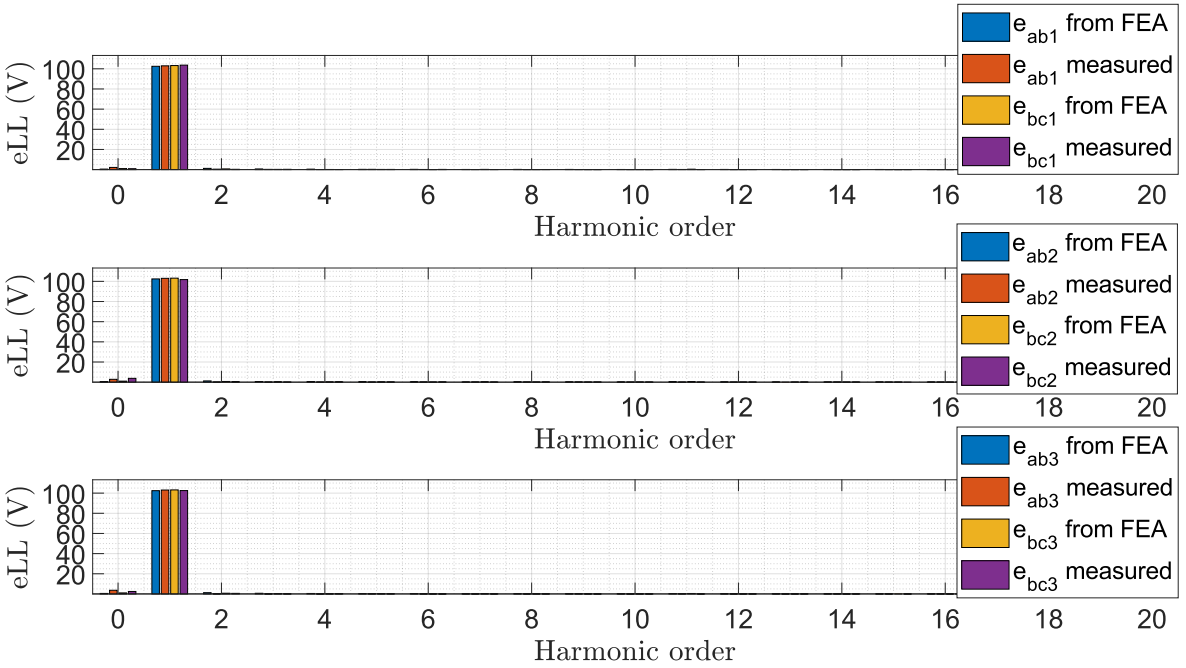

Figure 6.10: Line-to-Line back-emf waveform spectrum at 5000 rpm.

In Figure 6.11 the spectrum is shown in p.u. considering the FEA 1st harmonic as the base:

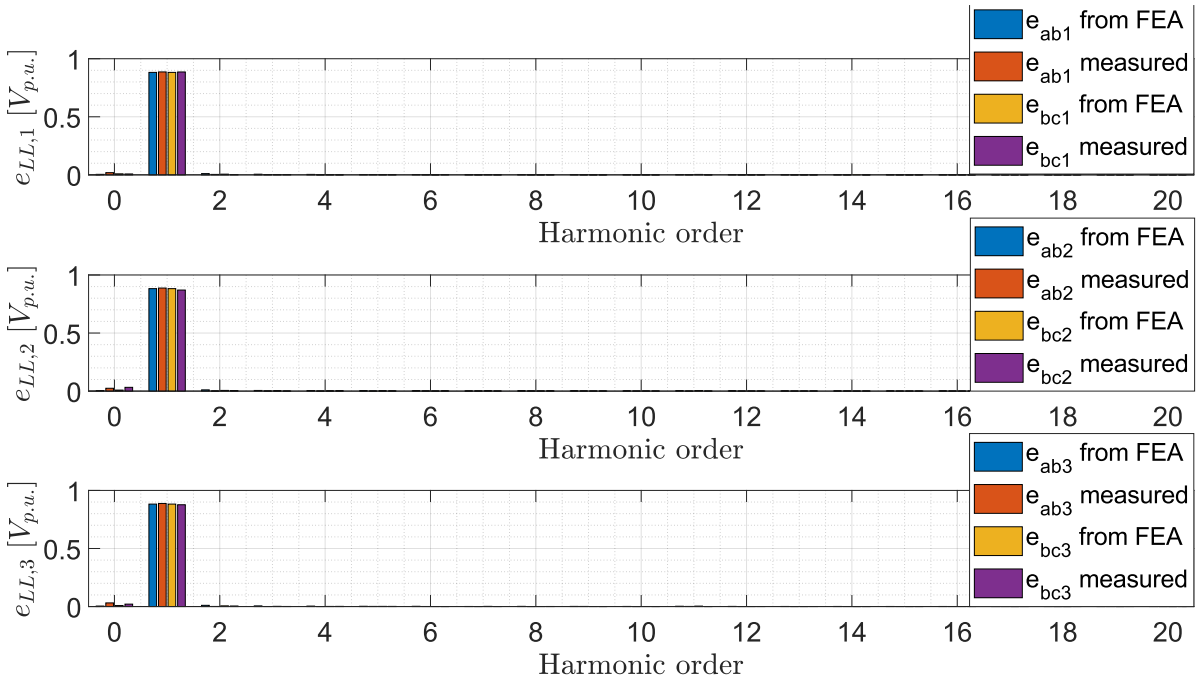

Figure 6.11: Line-to-Line Back-emf Waveform Spectrum in p.u. at 5000 rpm.

The same FFT spectra are shown in the logarithmic scale in fig. 6.11 and fig. 6.13.

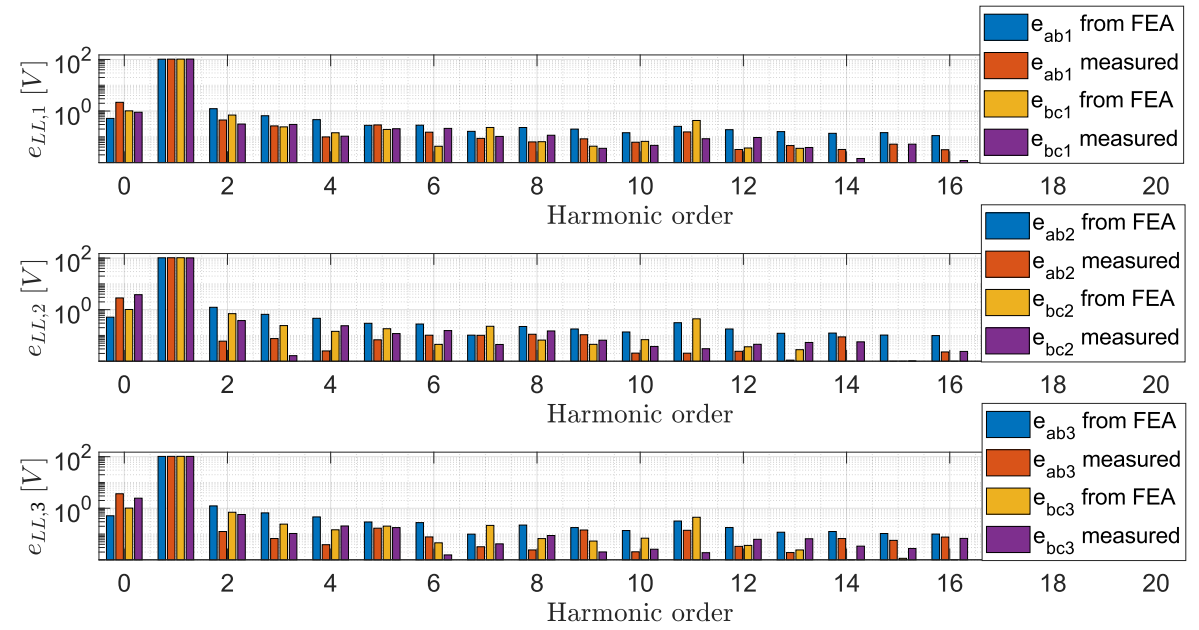

Figure 6.12: Line-to-Line Back-emf Waveform Spectrum at 5000 rpm (log scale).

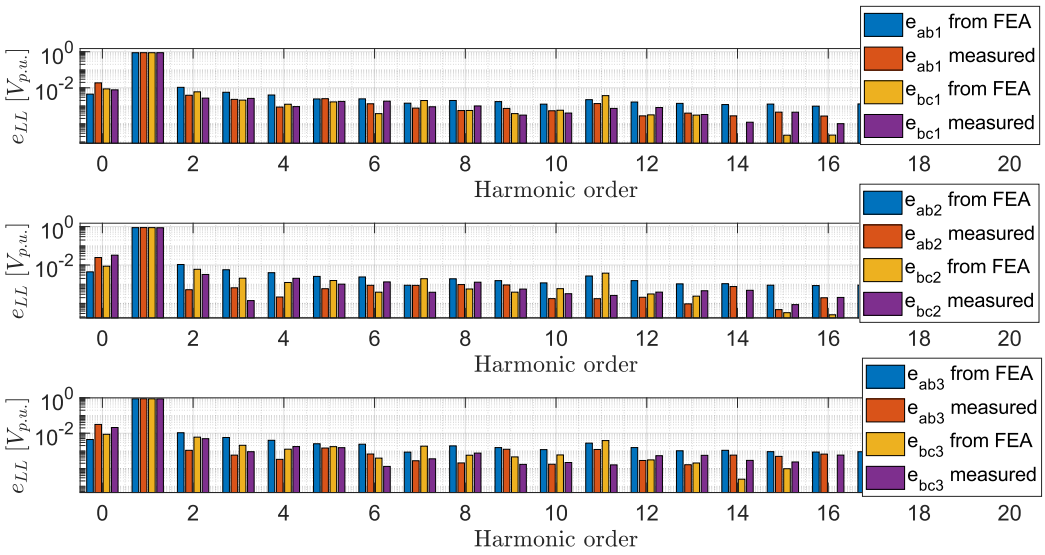

Figure 6.13: Line-to-Line Back-emf Waveform Spectrum in p.u. at 5000 rpm (log scale).

The harmonic components of the back-EMF waveform, higher than the 1st order, are negligible. This is due to the Halbach array magnets configuration that produces a very sinusoidal and distortion-free waveform of the magnetic field at the airgap.

In Figure 6.14 the peak value of the line-to-line back-emf from the experimental results and from the FEA at different speeds are compared:

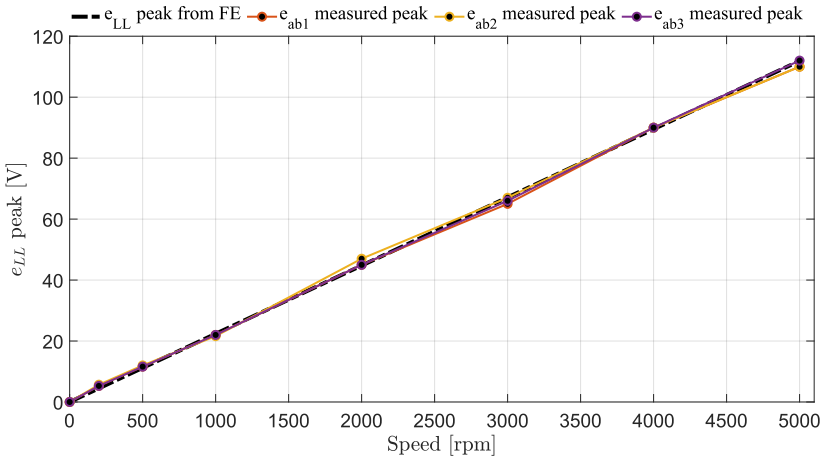

Figure 6.14: Comparison between the experimental, FE, and analytical back-EMF trends against the rotation speed. The back-EMF between phases a and b of each motor sector has been included in the graph.

6.2.2 Back-EMF test results and conclusion

The back-EMF test has shown that the machine is manufactured with symmetrical windings and the rotor does not present significant eccentricity. The measured waveforms match the simulated ones. The harmonic content of the back-EMF shows that the Halbach array layout of the magnets produces a very sinusoidal and distortion-free waveform of the back-emf according to the design criteria.

Chapter 7

Conclusions and Future Developments

Especially for aerospace applications, stresses on electric machine bearings are an important aspect to consider in reliability assessment. Typical sources of stress on bearings are due to the rotor mass unbalance and the gyroscopic couples acting on the machine rotor during flight maneuvers such as takeoff and landing. This work proposes a multi-physical analysis of the dynamic behavior of a multi-sector permanent magnet synchronous motor controlled to simultaneously produce torque, for the speed control, and radial forces, aiming to reduce the rotor vibrations and consequently the stress on the bearings.
After a literature review on the state of the art of radial force control carried out in Chapter 1, the electromagnetic model of the machine has been developed in Chapter 2 and it has been validated with some basic experimental tests reported in Chapter 6. The rotodynamic model of the rotor constraint by two bearings under force control performed by the multiphase machine is presented in Chapter 3. Chapter 4 focuses on the control architecture and strategy for vibration suppression at bearing locations. The control is based on the position feedback and is performed by using two PID controllers (one for the x displacement and one for the y displacement control). In Chapter 5, the simulation results show that it is possible to reduce the vibration amplitude at the bearing locations thanks to the force control based on the position feedback. In particular, considering the rotor cylindrical and conical mode shapes from the rotodynamic analysis, it has been shown that in the case of cylindrical mode shape the force control is capable to reduce the vibration at the bearings locations better than in the case of conical mode shape. Figure 5.29 shows that the vibration suppression is effective at low-medium speed (up to 15000 rpm), allowing the machine operation even at critical speeds. In fact, at the critical speed of 13000 rpm, the vibration reduction is significant and from more than 250 μm peak-to-peak, it reaches less than 40 μm peak-to-peak amplitude. However, the control does not perform so well at high speeds where the position control makes the vibration larger than without the control.

7.1 Future developments

Future developments of this research activity can be focused on the implementation of different control algorithms and on the analysis of more motor operating scenarios. In fact, the PID controllers are not the optimal solution for following non-constant references as the one calculated from the position feedback. For this reason, in literature, other control strategies for vibration suppression based on Notch Filters have been proposed [23]. Other experimental tests can be carried out on the available test rig to validate the model and the control developed in this thesis. Additionally, no current amplitude limits are set and no priority to the force control over the torque has been considered in this work. For this reason, future studies can focus on the current limitation strategies.
Lastly, the analysis of more motor operating scenarios can be investigated trying to discover additional limits and features of the control.

Bibliography

[1] C. Lin, S. Wang, M. Moallem, B. Fahimi, and C. Tschida, "Analysis of vibration in permanent magnet synchronous machines due to variable speed drives," *IEEE Transactions on Energy Conversion*, vol. 32, no. 2, pp. 582–590, 2017.

[2] J. Le Besnerais, "Vibroacoustic analysis of radial and tangential air-gap magnetic forces in permanent magnet synchronous machines," *IEEE Transactions on Magnetics*, vol. 51, no. 6, pp. 1–9, 2015.

[3] J. Leffler and P. Trnka, "Failures of electrical machines - review," in *2022 8th International Youth Conference on Energy (IYCE)*, 2022, pp. 1–4.

[4] S. K. Sahoo, P. Rodriguez, and M. Sulowicz, "Comparative investigation of fault indicators for synchronous machine failures," in *2014 International Conference on Electrical Machines (ICEM)*, 2014, pp. 1503–1509.

[5] C. Ma, Q. Liu, D. Wang, Q. Li, and L. Wang, "A novel black and white box method for diagnosis and reduction of abnormal noise of hub permanent-magnet synchronous motors for electric vehicles," *IEEE Transactions on Industrial Electronics*, vol. 63, no. 2, pp. 1153–1167, 2016.

[6] X. Chen, J. Wang, and V. I. Patel, "A generic approach to reduction of magnetomotive force harmonics in permanent-magnet machines with concentrated multiple three-phase windings," *IEEE Transactions on Magnetics*, vol. 50, no. 11, pp. 1–4, 2014.

[7] G. Serra, "Lecture slides: Metodologie di Progettazione delle Macchine Elettriche M, 2021-2022."

[8] M. Valavi, A. Nysveen, R. Nilssen, R. D. Lorenz, and T. Rølvåg, "Influence of pole and slot combinations on magnetic forces and vibration in low-speed pm wind generators," *IEEE Transactions on Magnetics*, vol. 50, no. 5, pp. 1–11, 2014.

[9] Z. Q. Zhu, M. L. Mohd Jamil, and L. J. Wu, "Influence of slot and pole number combinations on unbalanced magnetic force in pm machines with diametrically asymmetric windings," *IEEE Transactions on Industry Applications*, vol. 49, no. 1, pp. 19–30, 2013.

[10] J. S. Shiyu Zhou, "Active balancing and vibration control of rotating machinery: A survey," vol. 33, no. 5, p. 361–371, 2001.

[11] G. Valente, L. Papini, A. Formentini, C. Gerada, and P. Zanchetta, "Radial force control of multisector permanent-magnet machines for vibration suppression," *IEEE Transactions on Industrial Electronics*, vol. 65, no. 7, pp. 5395–5405, 2018.

[12] J. Asama, D. Kanehara, T. Oiwa, and A. Chiba, "Development of a compact centrifugal pump with a two-axis actively positioned consequent-pole bearingless motor," *IEEE Transactions on Industry Applications*, vol. 50, no. 1, pp. 288–295, 2014.

[13] M. Ooshima and C. Takeuchi, "Magnetic suspension performance of a bearingless brushless dc motor for small liquid pumps," in *2009 International Conference on Electrical Machines and Systems*, 2009, pp. 1–4.

[14] N. B. M. Neff and R. Schob, "Bearingless centrifugal pump for highly pure chemicals," in *Proc. 8th ISMB*, 2002, p. 283–287.

[15] K. Raggl, B. Warberger, T. Nussbaumer, S. Burger, and J. W. Kolar, "Robust angle-sensorless control of a pmsm bearingless pump," *IEEE Transactions on Industrial Electronics*, vol. 56, no. 6, pp. 2076–2085, 2009.

[16] Y. Okada, N. Yamashiro, K. Ohmori, T. Masuzawa, T. Yamane, Y. Konishi, and S. Ueno, "Mixed flow artificial heart pump with axial self-bearing motor," *IEEE/ASME Transactions on Mechatronics*, vol. 10, no. 6, pp. 658–665, 2005.

[17] J. Asama, T. Fukao, A. Chiba, A. Rahman, and T. Oiwa, "A design consideration of a novel bearingless disk motor for artificial hearts," in *2009 IEEE Energy Conversion Congress and Exposition*, 2009, pp. 1693–1699.

[18] T. Reichert, T. Nussbaumer, and J. W. Kolar, "Bearingless 300-w pmsm for bioreactor mixing," *IEEE Transactions on Industrial Electronics*, vol. 59, no. 3, pp. 1376–1388, 2012.

[19] ——, "Investigation of exterior rotor bearingless motor topologies for high-quality mixing applications," *IEEE Transactions on Industry Applications*, vol. 48, no. 6, pp. 2206–2216, 2012.

[20] W. Bauer and W. Amrhein, "Electrical design considerations for a bearingless axial-force/torque motor," *IEEE Transactions on Industry Applications*, vol. 50, no. 4, pp. 2512–2522, 2014.

[21] J. Asama, D. Watanabe, T. Oiwa, and A. Chiba, "Development of a one-axis actively regulated bearingless motor with a repulsive type passive magnetic bearing," in *2014*

International Power Electronics Conference (IPEC-Hiroshima 2014 - ECCE ASIA), 2014, pp. 988–993.

[22] G. Munteanu, A. Binder, T. Schneider, and B. Funieru, "No-load tests of a 40 kw high-speed bearingless permanent magnet synchronous motor," in *SPEEDAM 2010*, 2010, pp. 1460–1465.

[23] H. Mitterhofer, W. Gruber, and W. Amrhein, "On the high speed capacity of bearingless drives," *IEEE Transactions on Industrial Electronics*, vol. 61, no. 6, pp. 3119–3126, 2014.

[24] R. P. Jastrzebski, P. Jaatinen, O. Pyrhönen, and A. Chiba, "Design of 6-slot inset pm bearingless motor for high-speed and higher than 100kw applications," in *2017 IEEE International Electric Machines and Drives Conference (IEMDC)*, 2017, pp. 1–6.

[25] M. Ooshima, S. Kobayashi, and H. Tanaka, "Magnetic suspension performance of a bearingless motor/generator for flywheel energy storage systems," in *IEEE PES General Meeting*, 2010, pp. 1–4.

[26] B. Liu, "Survey of bearingless motor technologies and applications," in *2015 IEEE International Conference on Mechatronics and Automation (ICMA)*, 2015, pp. 1983–1988.

[27] A. Babin, R. Polyakov, L. Savin, and V. Tyurin, "Statistical analysis of turbo generator sets failure causes," *Vibroengineering Procedia*, vol. 31, pp. 129–133, 2020.

[28] P. F. Albrecht, J. C. Appiarius, R. M. McCoy, E. L. Owen, and D. K. Sharma, "Assessment of the reliability of motors in utility applications - updated," *IEEE Transactions on Energy Conversion*, vol. EC-1, pp. 39–46, 1986.

[29] E. Ward, "Preliminary investigation of an invertor-fed 5-phase induction motor," *Proceedings of the Institution of Electrical Engineers*, vol. 116, pp. 980–984(4), June 1969. [Online]. Available: https://digital-library.theiet.org/content/journals/10.1049/piee.1969.0182

[30] M. Qiao, C. Jiang, Y. Zhu, and G. Li, "Research on design method and electromagnetic vibration of six-phase fractional-slot concentrated-winding pm motor suitable for ship propulsion," *IEEE Access*, vol. 4, pp. 8535–8543, 2016.

[31] M. Villani, M. Tursini, G. Fabri, and L. Castellini, "High reliability permanent magnet brushless motor drive for aircraft application," *IEEE Transactions on Industrial Electronics*, vol. 59, no. 5, pp. 2073–2081, 2012.

[32] A. V. Brazhnikov, N. N. Dovzhenko, A. N. Minkin, O. V. Pomolotova, A. I. Litvinenko, and V. A. Shilova, "Multiphase hybrid traction drives for electrical vehicles," in *2014 International Symposium on Power Electronics, Electrical Drives, Automation and Motion*, 2014, pp. 583–588.

[33] C. Brecher, S. Neus, M. Gärtner, H. Eckel, M. Hoppert, B. James, C. Gerada, M. Degano, M. Ilkhani, and M. Di Nardo, "Design of an aircraft generator with radial force control [version 2; peer review: 1 approved]," *Open Research Europe*, vol. 2, no. 73, 2022.

[34] D. Torregrossa, D. Paire, F. Peyraut, B. Fahimi, and A. Miraoui, "Active mitigation of electromagnetic vibration radiated by pmsm in fractional-horsepower drives by optimal choice of the carrier frequency," *IEEE Transactions on Industrial Electronics*, vol. 59, no. 3, pp. 1346–1354, 2012.

[35] G. Valente, L. Papini, A. Formentini, C. Gerada, and P. Zanchetta, "Radial force control of multi-sector permanent magnet machines considering radial rotor displacement," pp. 140–145, 2017.

[36] S. Kobayashi, M. Ooshima, and M. N. Uddin, "A radial position control method of bearingless motor based on d - q -axis current control," *IEEE Transactions on Industry Applications*, vol. 49, no. 4, pp. 1827–1835, 2013.

[37] A. Laiho, A. Sinervo, J. Orivuori, K. Tammi, A. Arkkio, and K. Zenger, "Attenuation of harmonic rotor vibration in a cage rotor induction machine by a self-bearing force actuator," *IEEE Transactions on Magnetics*, vol. 45, no. 12, pp. 5388–5398, 2009.

[38] K. Halbach, "Design of permanent multipole magnets with oriented rare earth cobalt material," *Nuclear Instruments and Methods*, vol. 169, no. 1, pp. 1–10, 1980. [Online]. Available: https://www.sciencedirect.com/science/article/pii/0029554X80900944

[39] R. P. Praveen, M. H. Ravichandran, V. T. Sadasivan Achari, V. P. Jagathy Raj, G. Madhu, and G. R. Bindu, "A novel slotless halbach-array permanent-magnet brushless dc motor for spacecraft applications," *IEEE Transactions on Industrial Electronics*, vol. 59, no. 9, pp. 3553–3560, 2012.

[40] Z. Q. Zhu, "Recent development of halbach permanent magnet machines and applications," in *2007 Power Conversion Conference - Nagoya*, 2007, pp. K–9–K–16.

[41] I. Martinez-Ocaña, N. J. Baker, B. C. Mecrow, C. Gan, S. Brockway, and C. Hilton, "Manufacture and testing of an in-wheel halbach array motor for automotive traction," in *The 10th International Conference on Power Electronics, Machines and Drives (PEMD 2020)*, vol. 2020, 2020, pp. 56–61.

[42] Y. Yali, W. Yuanxi, and S. Feng, "Design of permanent magnet motor/generator using halbach magnetized structure for the flywheel energy storage system," in *Proceedings of 2011 6th International Forum on Strategic Technology*, vol. 1, 2011, pp. 593–597.

[43] K. Atallah and D. Howe, "The application of halbach cylinders to brushless ac servo motors," *IEEE Transactions on Magnetics*, vol. 34, no. 4, pp. 2060–2062, 1998.

[44] Z. Zhu, Z. Xia, K. Atallah, G. Jewell, and D. Howe, "Powder alignment system for anisotropic bonded ndfeb halbach cylinders," *IEEE Transactions on Magnetics*, vol. 36, no. 5, pp. 3349–3352, 2000.

[45] M. I. Friswell, J. E. T. Penny, S. D. Garvey, and A. W. Lees, *Dynamics of Rotating Machines*, ser. Cambridge Aerospace Series. Cambridge University Press, 2010.

[46] G. Sala, G. Valente, A. Formentini, L. Papini, D. Gerada, P. Zanchetta, A. Tani, and C. Gerada, "Space vectors and pseudoinverse matrix methods for the radial force control in bearingless multisector permanent magnet machines," *IEEE Transactions on Industrial Electronics*, vol. 65, no. 9, pp. 6912–6922, 2018.

[47] A. Tani, "Lecture slides: Modellistica dei Sistemi Elettromeccanici M, 2021-2022," 2022.

[48] C. Brecher, H.-M. Eckel, M. Fey, and F. Butz, "Prozesskraftmessung mit spindelintegrierter sensorik," *Zeitschrift für wirtschaftlichen Fabrikbetrieb*, vol. 113, no. 10, pp. 660–663, 2018. [Online]. Available: https://doi.org/10.3139/104.111982

[49] C. Brecher, S. Neus, M. Gärtner, H. Eckel, M. Hoppert, B. James, C. Gerada, M. Degano, M. Ilkhani, and M. Di Nardo, "Design of an aircraft generator with radial force control [version 2; peer review: 1 approved]," *Open Research Europe*, vol. 2, no. 73, 2022.

[50] F. P. H. T. S. W. E. Levi, R. Bojoi, "Multiphase induction motor drives – a technology status review," *IET Electric Power Applications*, vol. 1, pp. 489–516(27), July 2007. [Online]. Available: https://digital-library.theiet.org/content/journals/10.1049/iet-epa_20060342

[51] E. Levi, M. Jones, S. Vukosavic, and H. Toliyat, "A novel concept of a multiphase, multimotor vector controlled drive system supplied from a single voltage source inverter," *IEEE Transactions on Power Electronics*, vol. 19, no. 2, pp. 320–335, 2004.

Acknowledgements

I would like to thank the Electric Machines and Drives Research Group of the University of Bologna, especially my thesis supervisor Prof. Giacomo Sala. Thanks also to my co-supervisor Dr. Mauro Di Nardo and Dr. Meiqi Wang, who gave me the opportunity to do my thesis work at the University of Nottingham and helped me during all phases of the activity.
I also thank Prof. Michele Degano, who welcomed me to the Power Electronics, Machines and Control (PEMC) Research Group, Nottingham, and gave me the tools and help I needed to carry out my thesis project.
Last but not least, I would like to thank Asia who was always there for me throughout my entire path, and my family who gave me the opportunity and support to reach this important milestone.

Ringraziamenti

Ringrazio il gruppo di ricerca di Macchine Elettriche ed Azionamenti dell'Università di Bologna, in particolare il mio relatore prof. Giacomo Sala. Ringrazio i miei correlatori Ing. Mauro Di Nardo e Dr. Meiqi Wang che mi hanno dato l'occasione di svolgere la mia attività di tesi presso l'università di Nottingham e mi hanno supportato durante tutte le fasi dell'attività.
Ringrazio inoltre il Prof. Michele Degano, che mi ha accolto al PEMC (Power Electronics, Machines and Control (PEMC) Research Group, Nottingham), mi ha dato gli strumenti e l'aiuto necessario per realizzare il mio progetto di tesi.
Infine, ringrazio Asia che mi è sempre stata vicino durante tutto il mio percorso e la mia famiglia che mi ha dato l'opportunità e il supporto per raggiugere questo importante traguardo.